

THE UPPER CRUSTAL P-WAVE VELOCITY STRUCTURE OF NEWBERRY
VOLCANO, CENTRAL OREGON

by

MATTHEW WILLIAM BEACHLY

A THESIS

Presented to the Department of Geological Sciences
and the Graduate School of the University of Oregon
in partial fulfillment of the requirements
for the degree of
Master of Science

June 2011

THESIS APPROVAL PAGE

Student: Matthew William Beachly

Title: The Upper Crustal P-wave Velocity Structure of Newberry Volcano, Central Oregon

This thesis has been accepted and approved in partial fulfillment of the requirements for the Master of Science degree in the Department of Geological Sciences by:

Emilie E.E. Hooft Chairperson

Douglas R. Toomey Member

Katharine V. Cashman Member

and

Richard Linton Vice President for Research and Graduate Studies/Dean of
the Graduate School

Original approval signatures are on file with the University of Oregon Graduate School.

Degree awarded June 2011

© 2011 Matthew William Beachly

THESIS ABSTRACT

Matthew William Beachly

Master of Science

Department of Geological Sciences

June 2011

Title: The Upper Crustal P-wave Velocity Structure of Newberry Volcano, Central Oregon

Approved: _____
Prof. Emilie Hooft

The upper-crustal seismic-velocity structure of Newberry volcano, central Oregon, is imaged using P-wave travel time tomography. The inversion combines a densely-spaced seismic line collected in 2008 with two USGS seismic experiments from the 1980s. A high-velocity ring (7 km EW by 5 km NS) beneath the inner caldera faults suggests an intrusive ring complex 200 to 500 m thick. Within this ring shallow low velocities (<2 km depth) are interpreted as caldera fill and a subsided block. High velocities below 2 km depth could be intrusive complexes. There appears to be a low-velocity body at 3-6 km depth beneath the center of the volcano. This region is poorly resolved in the inversion because the ray paths bend around the low-velocity body. The 2008 data also recorded a secondary arrival that may be a delayed P-wave interacting with the low-velocity body.

CURRICULUM VITAE

NAME OF AUTHOR: Matthew William Beachly

GRADUATE AND UNDERGRADUATE SCHOOLS ATTENDED:

University of Oregon, Eugene, OR
Hastings College, Hastings, NE

DEGREES AWARDED:

Master of Science, Geology, 2011, University of Oregon
Bachelor of Arts, Physics, 2008, Hastings College

AREA OF SPECIAL INTEREST:

Seismology

PROFESSIONAL EXPERIENCE:

Teaching Assistant, Department of Physics, University of Oregon, 2011

Technical Assistant, Department of Geology, University of Oregon, 2010

Research Assistant, Department of Geology, University of Oregon, 2009-2010

Teaching Assistant, Department of Geology, University of Oregon, 2008-2009

Field Assistant, Summer of Applied Geophysical Experience (SAGE), Los
Alamos National Laboratory, 2008

Intern, Incorporated Research Institutions for Seismology (IRIS) Summer
Internship, University of Nevada, Las Vegas, 2007

Math Tutor, Educational Service Unit 9-CCC, 2007

Physics Tutor, Physics Department, Hastings College, 2005-2007

GRANTS, AWARDS AND HONORS:

\$1000, ExxonMobil SAGE Scholar, 2010

\$500, Geometrics SAGEEP Student Travel Scholarship, 2009

\$10,000 per year, Trustee Scholarship to Hastings College, 2004-2008

\$1000, Madgett Physics Scholarship, 2006, 2007

\$800, Dr. Harry R. James Physics Award, 2004, 2005

ACKNOWLEDGMENTS

I am most grateful for my advisor Emilie Hooft, who provided this Master's project, guided me through it and developed my scientific skills along the way. Sincere thanks to Douglas Toomey for providing tomography code and critical feedback in the writing of my thesis. I thank Troy Durant for his finite-difference modeling work. Thanks to Katharine Cashman for serving on my committee and also for developing my writing skills in her Geocommunication class. I appreciate Julie Donnelly-Nolan for sharing her expertise on Newberry Volcano. Thanks to Greg Waite who helped propose the 2008 Newberry Seismic Experiment. Many thanks to the volunteers who provided field labor during the 2008 Newberry Seismic Experiment. IRIS Pascal provided instruments and data collection, and Steve Azevedo and Eliana Dotson were very helpful for software support. Funding for the 2008 Newberry Seismic Experiment was provided by a USGS Venture Capital grant and NSF grants EAR-207670 and EAR-207671.

TABLE OF CONTENTS

Chapter	Page
I. INTRODUCTION.....	1
1.1. Magmatic Plumbing Systems	1
1.2. Detecting Magma Bodies.....	2
1.3. The Tomography Problem	2
1.4. Secondary Arrivals.....	3
1.5. Detecting Secondary Arrivals.....	6
1.6. 2008 Experiment Objective	6
II. NEWBERRY VOLCANO.....	7
2.1. Geologic Setting.....	7
2.2. Geologic Evidence for a Crustal Magma Chamber	8
2.3. Geophysical Evidence for a Crustal Magma Chamber.....	9
2.4. Upper Crustal Structure	11
III. SEISMIC DATA.....	13
3.1. 2008 Seismic Profile.....	13
3.2. 1983 USGS Refraction Line	17
3.3. 1984 USGS Tomography Array	19
3.4. Obtaining First Arrivals	20
IV. TOMOGRAPHIC METHODS.....	22
V. TOMOGRAPHY RESULTS	26
5.1. Inversion Settings.....	26
5.2. Low Velocity Anomalies	29
5.3. High Velocity Anomalies	31
VI. DISCUSSION.....	33
6.1. Shallow Volcanic Structure	33
6.1.a. Inner-Caldera Low-Velocity Zone.....	33
6.1.b. High-Velocity Ring.....	34

Chapter	Page
6.1.c Synthetic Ring Test.....	35
6.1.d. Caldera Collapse History.....	38
6.1.e. Local Stress Field.....	39
6.2 High-Velocity Region Below 2 km Depth.....	39
6.3 Low-Velocity Body Below 3 km Depth.....	42
6.3.a. Ray Path Deflection.....	43
6.3.b. Low-Velocity Body Test.....	45
6.3.c. High-Velocity Body Test.....	48
6.3.d. Structural Tests.....	50
6.3.e. Magma Chamber vs. Fractured Pluton.....	53
6.4. Secondary Arrival Analysis.....	54
6.4.a. Observation of a P-wave Secondary Arrival.....	54
6.4.b. Finite-Difference Model.....	55
6.4.c. Finite-Difference Results.....	56
6.4.d. Synthetic Seismics.....	57
6.4.e. Future Modeling.....	58
VII. CONCLUSIONS.....	61
APPENDICES.....	64
A. P-WAVE TRAVEL-TIME DATA.....	64
B. P-WAVE TRAVEL-TIME RESIDUALS.....	85
REFERENCES CITED.....	94

LIST OF FIGURES

Figure	Page
1. Wave-front isochrons display the position of a seismic wavefront at 0.2 second intervals through a synthetic velocity model with a magma chamber	3
2. Reflected and transmitted phases at a melt-solid interface	4
3. Finite-difference waveforms in a velocity model with 2 by 2 km ² low-velocity body	5
4. Map of Oregon locating Newberry Volcano	8
5. Interpreted structural features overlain on the perturbational P-wave velocity model from Achauer et al., 1988	10
6. Residual gravity anomaly map adapted from Gettings and Griscom (1988) compared to a P-wave velocity model from 1.26 to 2.95 km depth adapted from Zucca and Evans (1992).....	12
7. Map of the 2008 seismic experiment	14
8. Vertical-component record section from the 2008 profile.....	15
9. Radial-component record section from the 2008 profile	16
10. L-22D seismometer being oriented and buried.....	17
11. Map of all active-source seismic experiments at Newberry	18
12. Example seismic record section for shot 7 on the 1983 seismic line.....	19
13. Example record section for shot 13, 1984 USGS array.....	20
14. Map-view plot of residuals for event 13, 1984 USGS array, and histogram of residuals.	21

Figure	Page
15. Velocity layer model from Catchings and Mooney (1988) and 1D initial velocity model profiles used in the inversion	23
16. Ray paths through the initial 1D velocity model	24
17. The final velocity model shown in depth sections.....	31
18. 3D representation of velocity anomalies.....	32
19. Synthetic model with a 500 m thick, 10% high-velocity ring	37
20. Depth section at 2.5 km through the final velocity model compared to an inversion with the 2008 seismic data removed.....	41
21. Residual gravity anomaly map adapted from Gettings and Griscom (1988) compared to the P-wave velocity anomaly model	42
22. Ray bending around a low-velocity body at 3-6 km depth beneath the caldera	44
23. Synthetic test model with a negative 40% low-velocity body at 3 to 6 km depth.....	47
24. Synthetic test model with a 10% high-velocity body	49
25. Synthetic test model with a continuous -10% low-velocity column extending to 6 km depth.....	51
26. Synthetic test model with a separated -10% low-velocity column to 2.5 km depth and a -40% low velocity body from 3 to 6 km depth.....	52
27. The central section of the 2008 vertical-component record section compared to the central section of the synthetic seismic record section with matching P-wave secondary arrivals	58

LIST OF TABLES

Table	Page
1. Description of the source events	28

CHAPTER I

INTRODUCTION

1.1. Magmatic Plumbing Systems

The concept of a magma plumbing system has evolved over the past six decades from a simple chamber of melt to more geometrically complex systems sometimes involving multilevel networks of magma reservoirs. The concept of magma storage beneath volcanoes arises from the geochemical observation that magma evolves from mafic to silicic composition and that eruptions may involve large volumes of magma. In order for mafic melt rising from a mantle source to erupt as silicic lava from a volcano, it must reside in the crust long enough to crystallize and separate its mafic components or assimilate silicic components from the crust. This necessitates the idea of a magma reservoir in the crust between a volcano and the mantle source. Many solidified magma bodies are now exposed as plutons, exhibiting geometries ranging from thin dikes to massive sills hundreds of kilometers wide (see Marsh (1989) for a review). Geophysical interpretations of magma bodies vary on a similar scale. Geophysical studies find and interpret magma plumbing systems as mush zones with a small percentage of partial melt (e.g. Chu et al., 2010, West et al., 2001), sills of almost pure melt (e.g. Zollo et al., 2008), or segregated magma bodies with a pure melt sill overlying a mush zone (e.g. Dunn et al., 2000). Magma bodies are found within the crust at a variety of depths, and it is unresolved whether the depth is determined by the level of neutral buoyancy (Ryan, 1988), by lithological barriers (Hooft and Detrick, 1993) or by the freezing horizon

(Phipps Morgan and Chen, 1993). The concept of a volcanic magma plumbing system is highly variable and expected to differ between volcanic locations. Volcanic plumbing system models range from a single stratified chamber, to multilevel sills and conduits (e.g. Bons et al., 2001), to geophysically undetectable systems of small, dispersed dikes and sills (e.g. Stauber et al., 1988). Continued research is needed to better image volcanic plumbing systems, and this is necessary to understand the geochemical evolution of magmas, eruption mechanisms, caldera formation, and volcanic hazards.

1.2. Detecting Magma Bodies

Detecting crustal magma bodies poses geophysical challenges. These include constraining the depth, shape, and melt content of the magmatic system. In studying magma bodies, the most popular and successful geophysical technique is seismic tomography (see Lees (2007) for a review). Seismic tomography observes magma bodies as regions of low velocity and high attenuation. Unfortunately, low-velocity zones are poorly resolved by seismic tomography when their width is less than the dominant wavelength, about 1 km resolution for explosive sources. It is not surprising that many seismic tomography studies have been inconclusive in detecting crustal magma bodies.

1.3. The Tomography Problem

Seismic tomography detects velocity anomalies by analyzing travel times. A travel time is the difference between the time of a seismic event and the time when a seismometer records the first impulse of energy from the seismic event (arrival time). The first-arriving energy travels along the fastest path, as stated by Fermat's Principle. The fastest path tends to "circumvent" (Steck et al., 1998) low-velocity zones instead of traveling through them (Figure 1). This ray-bending effect can be explained by Huygens'

principle. A wavefront encountering a low-velocity zone becomes delayed in that region. The corners of the undisrupted wavefront then disperse energy into the delayed region, causing the wavefront to heal. The healed region of the wave is slightly delayed and decayed in amplitude as a result of energy deflection around the low-velocity zone.

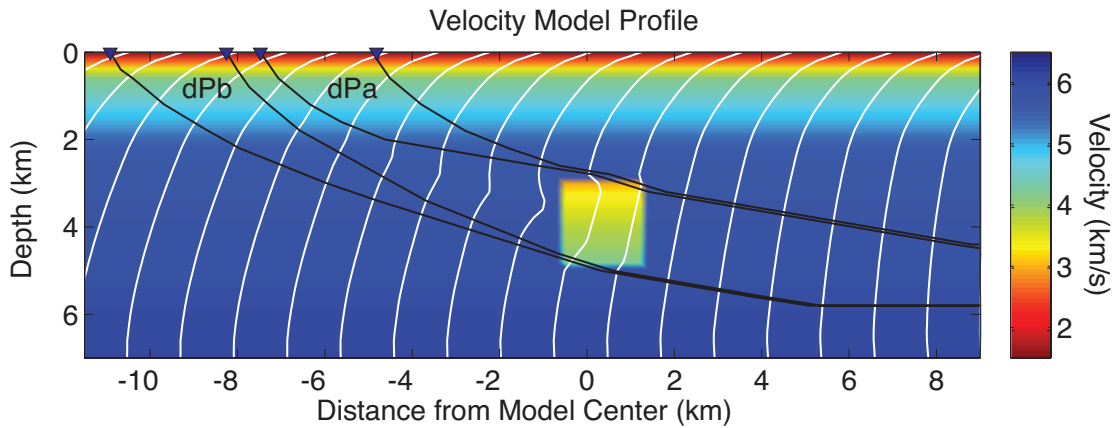


Figure 1. Wave-front isochrons (white lines) display the position of a seismic wavefront at 0.2 second intervals through a synthetic velocity model. A 2 by 2 km², 30% low-velocity body is located at 3 to 5 km depth. The isochrons acquire a 0.1 second delay in the low-velocity body but the wavefront recovers just 5 km beyond the low-velocity body. First-arrival ray paths (black lines) show that the fastest paths deflect from above (dPa) and below (dPb) the low-velocity body as described by Wilcock et al. (1993).

1.4. Secondary Arrivals

While tomography detects a delay or amplitude reduction indirectly due to deflection around a low-velocity zone, additional information can be obtained from energy that directly encountered the low velocity zone. This energy appears later than the first arrival and is referred to as a secondary arrival. Several types of secondary arrivals from magma bodies have been observed (Figure 2) such as PreflP reflections (e.g. Brown et al., 1980), SreflS reflections (Sanford et al., 1973), converted PtransS transmissions (Sheetz and Schlue, 1992) converted PreflS reflections (e.g. Durant and Toomey, 2009), and even StransP transmissions (Sanford et al., 1973). The amplitude of the resulting secondary arrivals depends on the angle of incidence and the velocity contrast

encountered by the direct wave, as described by the Zoeppritz Equations (e.g. Shuey 1985). While converted and reflected S-wave phases can result from any seismic interface, they are especially strong from magma bodies because liquid melt does not transmit S-waves. Also, a P-wave transmitted through a magma body, or any low velocity zone, can become focused by refraction to produce a high-amplitude PtransP secondary arrival (West et al., 2001). The high amplitude of PtransP is apparent in Figure 3, which shows the full seismic wave field propagating through the velocity model shown in Figure 1. Figure 3 also shows the emergence of converted P to S-waves at the interface of the magma chamber such as a PreflS wave at the top of the magma body (Figure 3a), and a PtransS wave exiting the magma body following PtransP (Figure 3b). These secondary arrivals result from direct interaction with a low-velocity body while a first arrival might avoid a low velocity body.

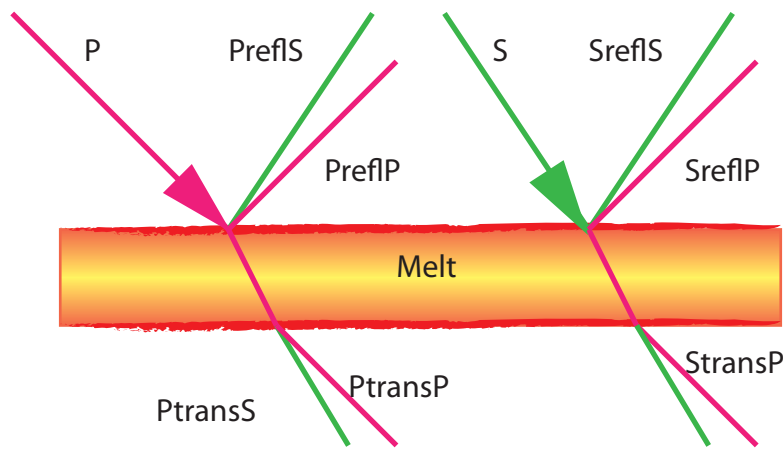


Figure 2. Reflected and transmitted phases at a melt-solid interface. Because shear-wave energy does not transmit through liquid, melt produces characteristically strong P to S-wave conversions such as PreflS and PtransS. Reflections PreflP and SreflS are also strong.



Figure 3a. Finite-difference waveforms in a velocity model with 2 by 2 km² low-velocity body similar to Figure 1. The P-wave in pink has been delayed and focused within the low-velocity body as a high-amplitude PtransP. A converted PreflS phase in green emerges from the top of the low-velocity body.

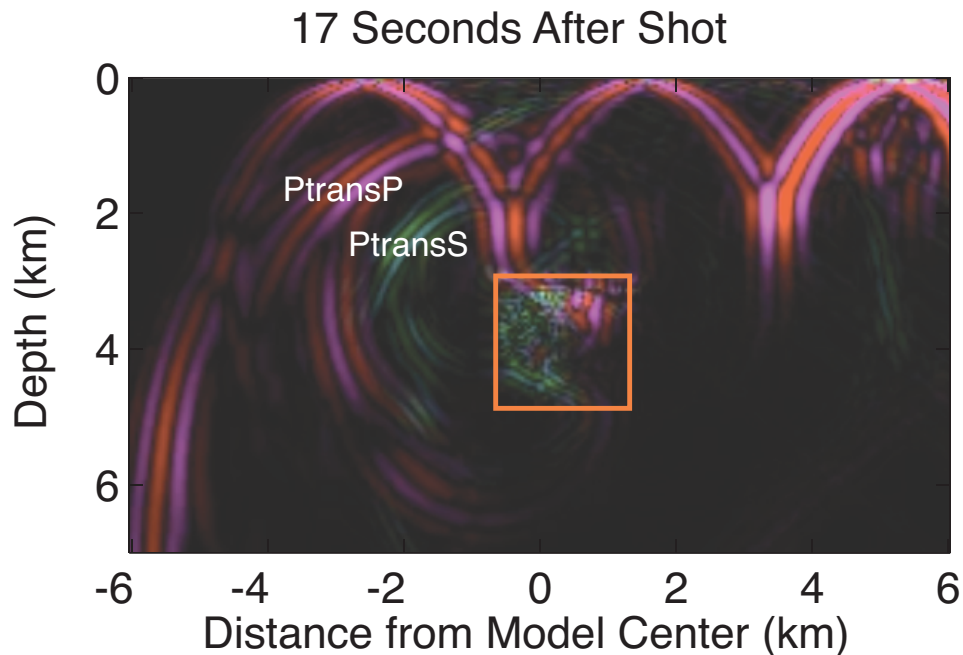


Figure 3b. Finite-difference waveforms 2 seconds after Figure 3a. A strong PtransP phase and a weaker PtransS phase travel toward the surface. Wavefronts split above and below the magma chamber have rejoined, healing the first-arrival wavefront. The healed region has lower amplitude and is slightly delayed.

1.5. Detecting Secondary Arrivals

Identifying a secondary arrival from a small magma body requires a high-quality seismic dataset. The seismic wavefield must be densely sampled to observe secondary arrivals and distinguish them from other information in the wave coda. Secondary arrivals are successfully observed in marine experiments due the general high quality of marine seismic data. Marine, active-source experiments produce dense, evenly spaced record sections by navigating an airgun source in a straight line and shooting at short intervals. This is not the case in land experiments where accessibility limits the locations of seismometers, chemical explosions, and routes suitable for vibroseis trucks. Land experiments on volcanoes have not been as successful at detecting secondary arrivals from magma bodies as marine experiments on ocean ridges (e.g. Durant and Toomey, 2009). In fact, the most successful studies that detected secondary arrivals in volcanoes employed airgun sources in a nearby body of water (Ben-Zvi et al., 2009, Auger et al., 2001) or above a subaqueous volcano (West et al., 2001).

1.6. 2008 Experiment Objective

The primary objective of the 2008 Newberry seismic profile was to detect secondary arrivals from a magma chamber with a land-based experiment. The experiment was designed to simulate the geometry of a marine experiment on land to obtain a dense, three-component seismic record section. Secondary arrivals were expected from an already proposed (Achauer et al., 1988; McLeod and Sherrod 1988), yet debated (Zucca and Evans, 1992), magma chamber at 3-5 km depth. The secondary objective of this experiment was to obtain additional P-wave travel-time data for use in a tomographic inversion to image Newberry's shallow volcanic structure.

CHAPTER II

NEWBERRY VOLCANO

2.1. Geologic Setting

Newberry volcano provided an ideal setting for the 2008 seismic experiment. Newberry is a shield volcano 60 km east of the Cascade axis in Central Oregon (Figure 4). Though low in profile, Newberry is the largest volcano in the Cascades; its lavas cover an area of $\sim 3000 \text{ km}^2$ with an estimated volume of 500 km^3 (Jensen et al., 2009). The center of Newberry Volcano holds a caldera with a relatively recent collapse event at 75 ka (Julie Donnelly-Nolan, personal communication, 2010). The caldera extends 8 km east-west by 6.5 km north-south, and lies within a national monument with accessible roads and developed camping. The accessibility of Newberry Volcano facilitated deployment of a straight, evenly spaced, seismic experiment. Newberry was chosen for this study because a shot was planned 30 km northeast of the caldera as part of an NSF-funded High Lava Plains experiment and because of the possibility of a crustal magma body beneath Newberry's caldera.

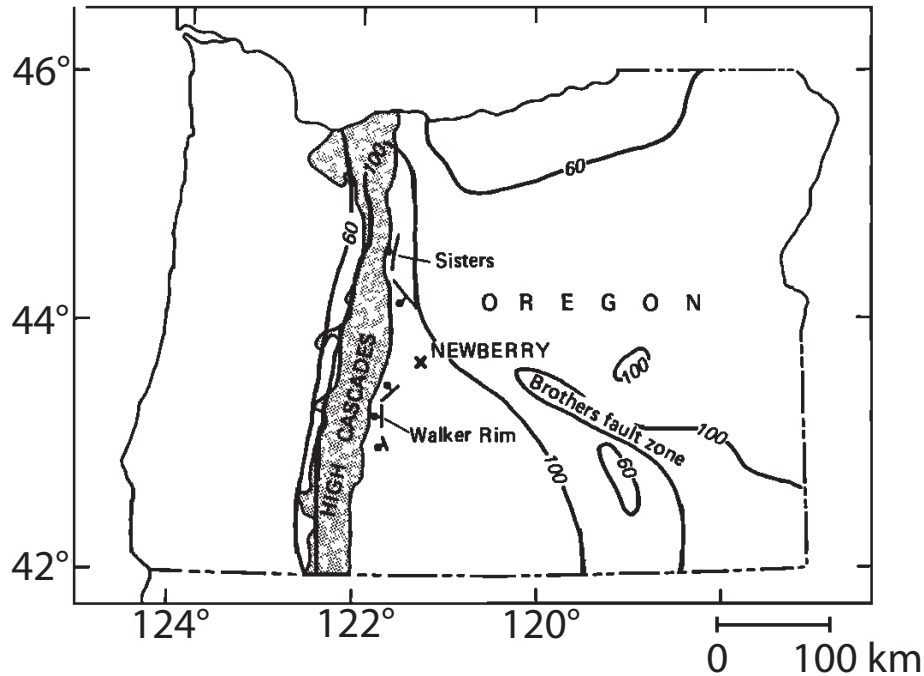


Figure 4. Map of Oregon adapted from Sammel et al., (1988). Newberry Volcano is located in Central Oregon, 60 km east of the High Cascades and at meeting point of the Sisters and Walker Rim Fault Zones.

2.2. Geologic Evidence for a Crustal Magma Chamber

Geologic evidence at Newberry volcano suggests the presence of a shallow crustal magma body. Recent activity includes the Northwest Rift Zone eruptions, which occurred 7000 years ago (McKay et al., 2009), and the Big Obsidian flow, only 1300 years ago. Newberry is characterized by having a bimodal compositional distribution with mafic eruptions outside the caldera and silicic eruptions within (MacLeod and Sherrod, 1988). For example, the Northwest Rift Zone eruptions opened vents both north and south of Newberry Crater, which produced basalt and andesite flows, while the Big Obsidian Flow within Newberry Caldera is a rhyolite obsidian flow. MacLeod and Sherrod (1988) attribute this bimodal distribution to a magma chamber “shadow effect.” Rising mafic magma that encounters an evolved magma storage system underplates the

less-dense silicic magma and forces silicic magma to erupt. Elsewhere the unobstructed mafic magma erupts at the surface, such as during the Northwest Rift Zone eruptions. It is possible that a central magma body may have frozen since the last eruption 1300 years ago, although the Newberry 2 drill hole, located at the center of the caldera, indicates elevated crustal temperatures. A drill-core temperature of 265°C at 932 m depth suggests by extrapolation that melt could reside only 2 km below the surface (Keith and Bargar, 1988).

2.3. Geophysical Evidence for a Crustal Magma Chamber

Previous geophysical studies at Newberry Volcano do not concur regarding the presence of a shallow magma chamber. Teleseismic tomography (Stauber et al., 1988) did not detect a low-velocity anomaly expected from a magma chamber, and concluded that there was no magma chamber greater in width than the horizontal-resolution limit of 5 km. While electromagnetic studies, summarized by Fitterman et al. (1988), did not observe an expected conductive anomaly coincident with the proposed magma chamber they concluded that the presence of a shallower conductive layer may have obscured the magma chamber. Both articles suggested that low quantities of melt could reside in dispersed pockets and remain undetectable. On the other hand, an active-source tomography experiment (Achauer et al., 1988) detected evidence for a magma chamber as an 8% low-velocity body at 3-5 km depth beneath the caldera and estimated the magma chamber to be several tens-of-km³ in volume (Figure 5). However, a later P-wave attenuation study of the same seismic data (Zucca and Evans, 1992) interpreted the same low-velocity body as a pluton, because they found only average attenuation instead of high attenuation coincident with the low-velocity body. Zucca and Evans (1992)

suggested that a hot pluton with dry, gas-filled cracks could have moderate attenuation and low velocity. Both interpretations assumed that the reconstructed velocity and attenuation anomalies are reliable. However, the imaged structures may be inaccurate if the deflection effects described in Section 1.2 are not considered. In this thesis, I address the resolution of these data and combine them with new data in a new P-wave tomography study.

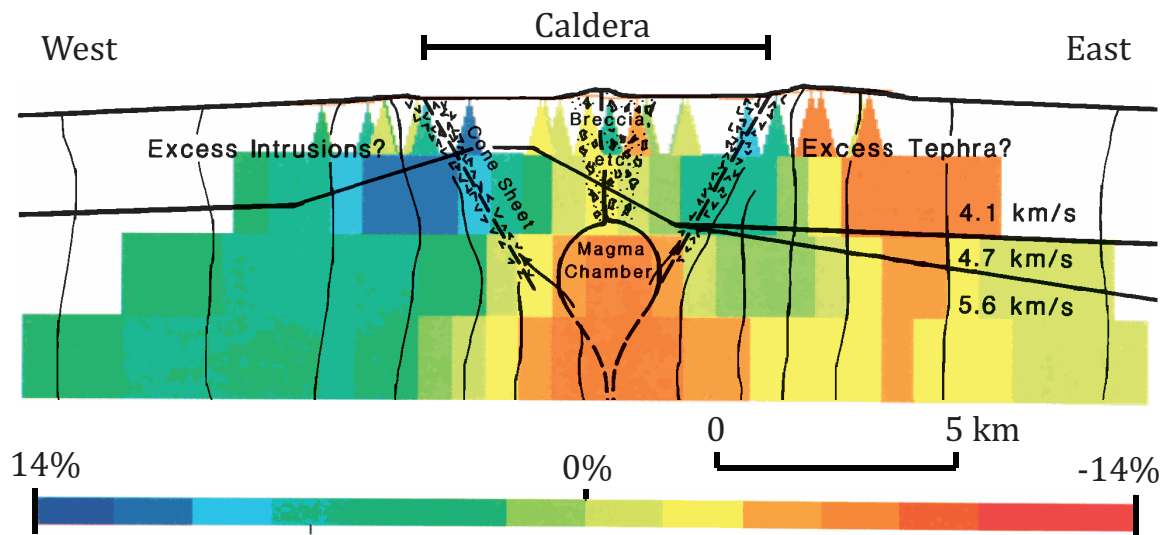


Figure 5. Interpreted structural features overlain on the perturbational P-wave velocity model from Achauer et al., 1988. The cross section strikes east-west through the center of Newberry caldera. Velocities are colored by percent perturbation from the layer's average. Achauer et al. (1988) proposed a small magma chamber at 3-5 km depth in the low velocity region. High velocity intrusions, here interpreted as cone sheets, may dip inward from the caldera rim down to a central magma chamber. Dark lines from left to right outline the original velocity layers from the Catchings and Mooney (1988) seismic refraction profile and show the western intrusive zone as an uplifted high velocity layer (blue).

2.4. Upper Crustal Structure

The earlier geophysical studies detected various volcanic structural features beneath Newberry volcano. The possible magma chamber below 3 km depth is overlain by a zone of low velocities within the caldera (Figure 6, right panel, feature D) interpreted as caldera fill and a breccia pipe (Achauer et al., 1988). Borehole data (Keith and Bargar, 1988) confirm clastic deposits in the upper 900 m of caldera fill, comprised of mainly tuffs in the upper 500 m and lava flows beneath. Just west of the caldera fill zone and below 2 km depth lies an inferred intrusive complex characterized by high-velocities (Catchings and Mooney, 1988), high-gravity (Gettings and Griscom, 1988), and high-resistivity (Fitterman, 1988, Figures 5 and 6). Finally, a high-velocity, high-gravity ring underlies the caldera and surrounds the low-velocity, caldera fill zone (Figure 6, B). Achauer et al. (1988) interpret this ring feature as silicic cone-sheets dipping at 60° inward toward the proposed central magma chamber (Figure 5). Gettings and Griscom (1988) detected a corresponding high-density ring beneath the caldera but prefer a vertical, mafic ring-dike interpretation instead. These two interpretations differ significantly. Ring-dikes are most often silicic to intermediate composition and form during caldera collapse, whereas cone-sheets are usually mafic and form during uplift (Saunders, 2004).

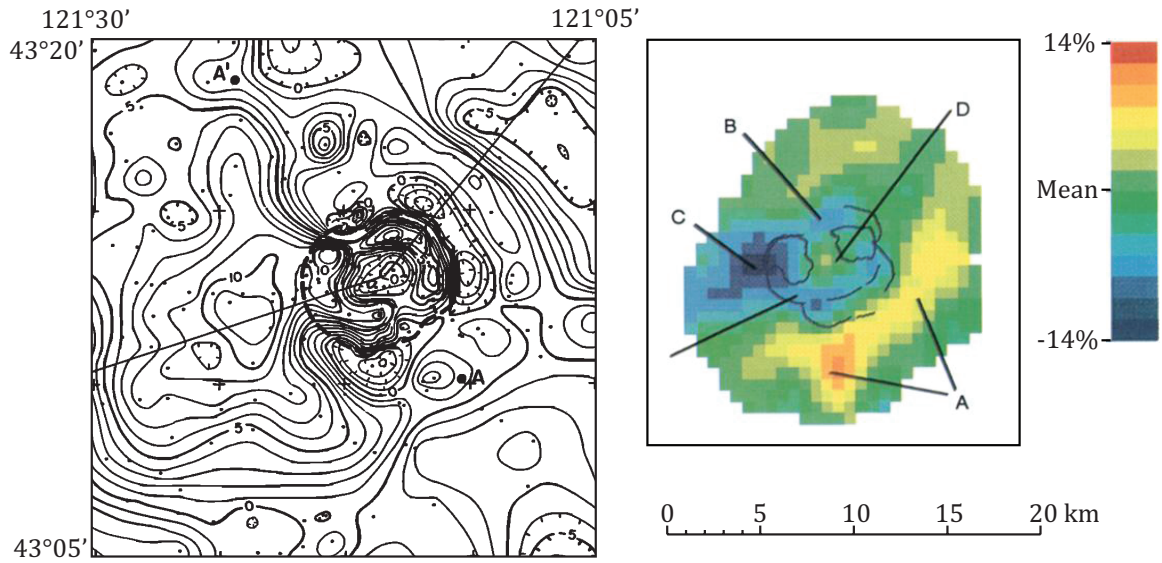


Figure 6. (Left) Residual gravity anomaly map adapted from Gettings and Griscom (1988). Gravity anomaly is contoured every 1 mGal. Stations (dots) are corrected for topography. A dashed line represents the caldera rim. (Right) P-wave velocity model section from 1.26 to 2.95 km depth adapted from Zucca and Evans (1992). The velocity model is from Achauer et al. (1988). High-velocity features B and C correspond to high gravity anomalies.

CHAPTER III.

SEISMIC DATA

This study reexamines the velocity structure of Newberry volcano using seismic tomography in addition to detecting secondary arrivals. The following sections first present the 2008 seismic experiment and its results, including an observed secondary arrival, then introduce two previous seismic experiments conducted by the USGS: a refraction line from 1983 (Cotton and Catchings, 1989) and a tomography array from 1984 (Dawson and Stauber, 1986). All three seismic studies contribute P-wave travel time data to the new P-wave tomography study.

3.1. 2008 Seismic Profile

The objective of the 2008 seismic experiment was to record a secondary arrival from a crustal magma body with a dense, high-quality seismic experiment in a terrestrial setting at Newberry Volcano. Fieldworkers from the University of Oregon, Michigan Tech, and PASSCAL with funding from the NSF and USGS deployed 75 seismometers in a line centered on Newberry caldera spanning 40 km from southwest to northeast (Figure 7). PASSCAL provided Mark Products L-22D short-period, three-component seismometers. The seismometers were buried in a half meter of volcanic ash, oriented by compass, and calibrated for amplitude using a PASSCAL CalBox and BirdDog II. The seismometer spacing was 300 m in the caldera and on the upper flanks and 800 m on the outer flanks. A parallel line of six seismometers was located between the two lakes

within the caldera, just north of the main line. The even spacing of seismometers and near straight-line deployment ensured that the 2008 experiment had enough trace-to-trace coherence in a record section to identify secondary arrivals.

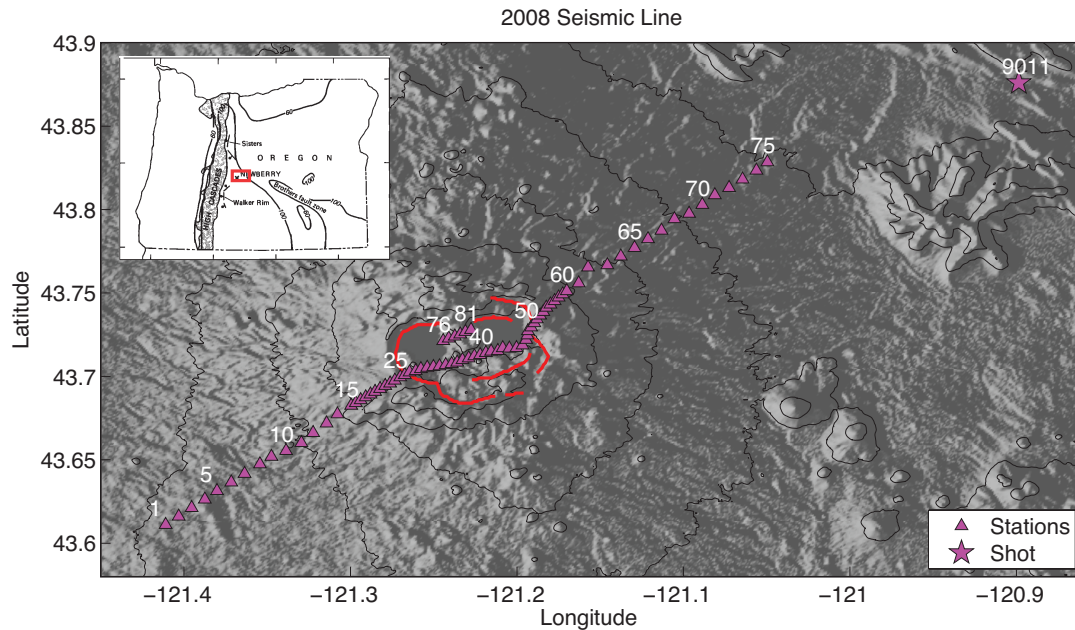


Figure 7. Map of the 2008 seismic experiment on shaded topography with a 200 m contour interval. The seismic line is 40 km long and centered on Newberry caldera. Stations (triangles) are spaced every 300 m near the volcano's center, and 800 m on its flanks. Stations are labeled from 1 to 75 along the main line, and 76 to 81 along the inter-lake line. Shot 9011 (star) of the High Lava Plains Experiment was 30 km northeast of the caldera. The shot occurred ~5 km south of the planned location. Exposed caldera ring fractures are marked in red (from MacLeod et al., 1995).

The 2008 seismic profile recorded a borehole explosion (907 kg TNT equivalent at 20 m depth) 30 km northeast of Newberry from the High Lava Plains experiment (Figure 7). Taking advantage of this previously planned shot provided a cost effective opportunity to test whether secondary arrivals could be observed from an explosive source. In addition, the array recorded teleseismic events for two weeks. There were no explosions on the southeast end of the line, unlike a standard refraction experiment, because the objective was to test a method using a shot of opportunity.

The 2008 seismic data contain an interesting secondary arrival in the vertical-component record section (Figure 8). The record section clearly records the first arrival wavefront from the eastern end of the line to the caldera. At the caldera rim, the first arrival wavefront advances by 0.5 seconds and undergoes an amplitude decrease just within the caldera. Noise amplitude increases on the central region of the line where elevation is high and is probably caused by wind on exposed topography because there is less noise just within the caldera. On the western caldera rim, the first arrival is not picked for 3 km (ranges 37 to 40 km) because it cannot be distinguished from noise. In the range where the first arrival is not observed, a secondary arrival is observed. The secondary arrival is visible ~ 0.7 seconds after the expected first-arrival at 36 km range, and then merges with the first arrival at 39 km range.

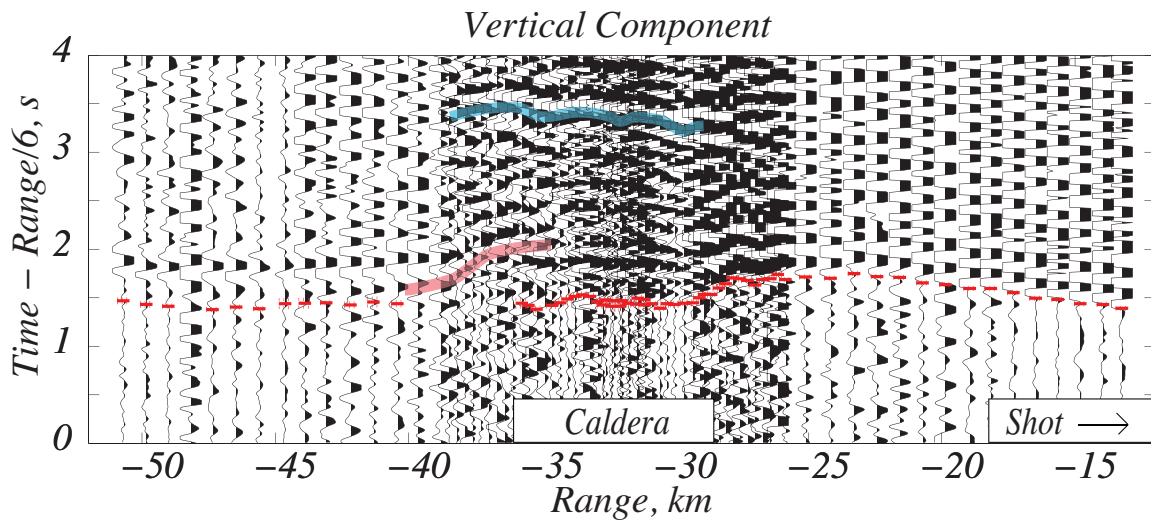


Figure 8. Vertical-component record section from the 2008 profile. First arrival picks are in red. Traces are range reduced at 6 km/s. A 1 to 5 Hz Butterworth filter reduces noise. Amplitude scaling is fixed and trace amplitudes are clipped for display purposes. Traces are spaced 800 m along the east and west sections of the line, with 300 m spacing near the center of the caldera. A secondary arrival is highlighted in pink along a prominent phase. An unidentified secondary arrival arrives later and is highlighted in blue.

The 2008 seismic profile recorded three-component seismic data with channels oriented vertical, north-south, and east-west. The east-west and north-south channels were rotated to obtain radial component data, aligned towards and away from the shot, northeast to southwest (Figure 9). Radial component data were expected to be most useful in identifying S-wave secondary arrivals characteristic of magma bodies, however, none were observed. It is possible that S-wave secondary arrivals are obscured by a poor signal-to-noise ratio in the radial component data. The pumice and ash at Newberry may have provided a poor medium for recording S-waves due to attenuation and poor coupling with buried seismometers (Figure 10). Also, the ray-geometry from the source at 30 km distance may have resulted in a large incidence angle beneath a shallow magma chamber and thus be poorly suited for P to S-wave transmissions or reflections.

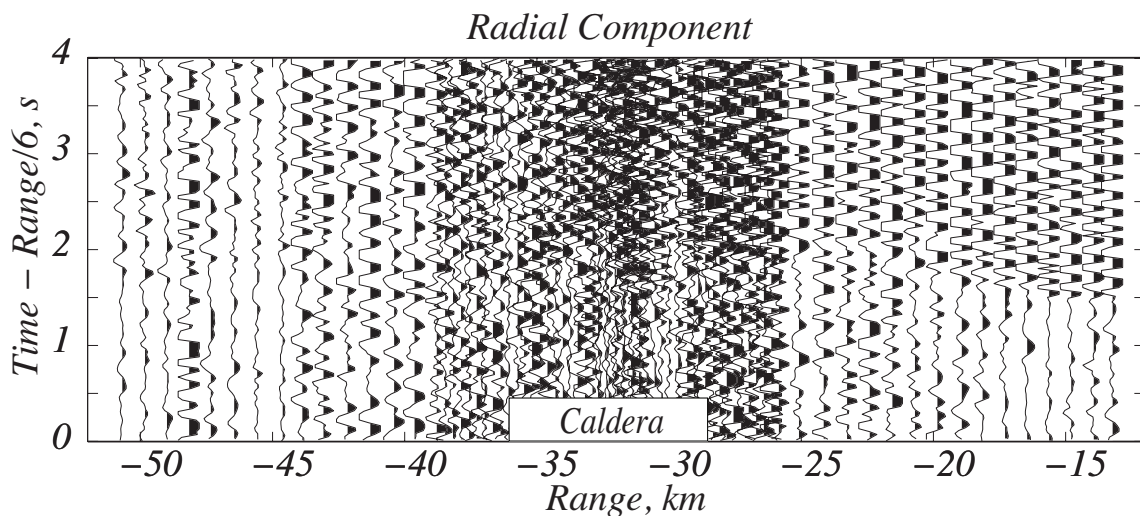


Figure 9. Radial-component record section from the 2008 profile. Settings are the same as the vertical-component record section in Figure 10. The signal-to-noise ratio is very poor and no clear secondary arrivals are observed.



Figure 10. L-22D seismometer being oriented and buried in 18 inches of volcanic ash at station 33. The three channels were oriented vertically, north-south, and east-west.

3.2. 1983 USGS Refraction Line

The 1983 seismic refraction line (Figure 11, blue) provided abundant east-west data coverage for the inversion. The USGS deployed 120 vertical-component seismometers in a 60 km east-west profile across Newberry volcano. The inversion includes data from five shots along this profile, one of which recorded a secondary arrival (Figure 12) that is possibly related to the secondary arrival observed in the 2008 record section. The shots were 900 and 1800 kg equivalent of TNT in 40 and 60 m boreholes. These shots were spaced every 15 km along the line while the seismometers were spaced 500 m apart.

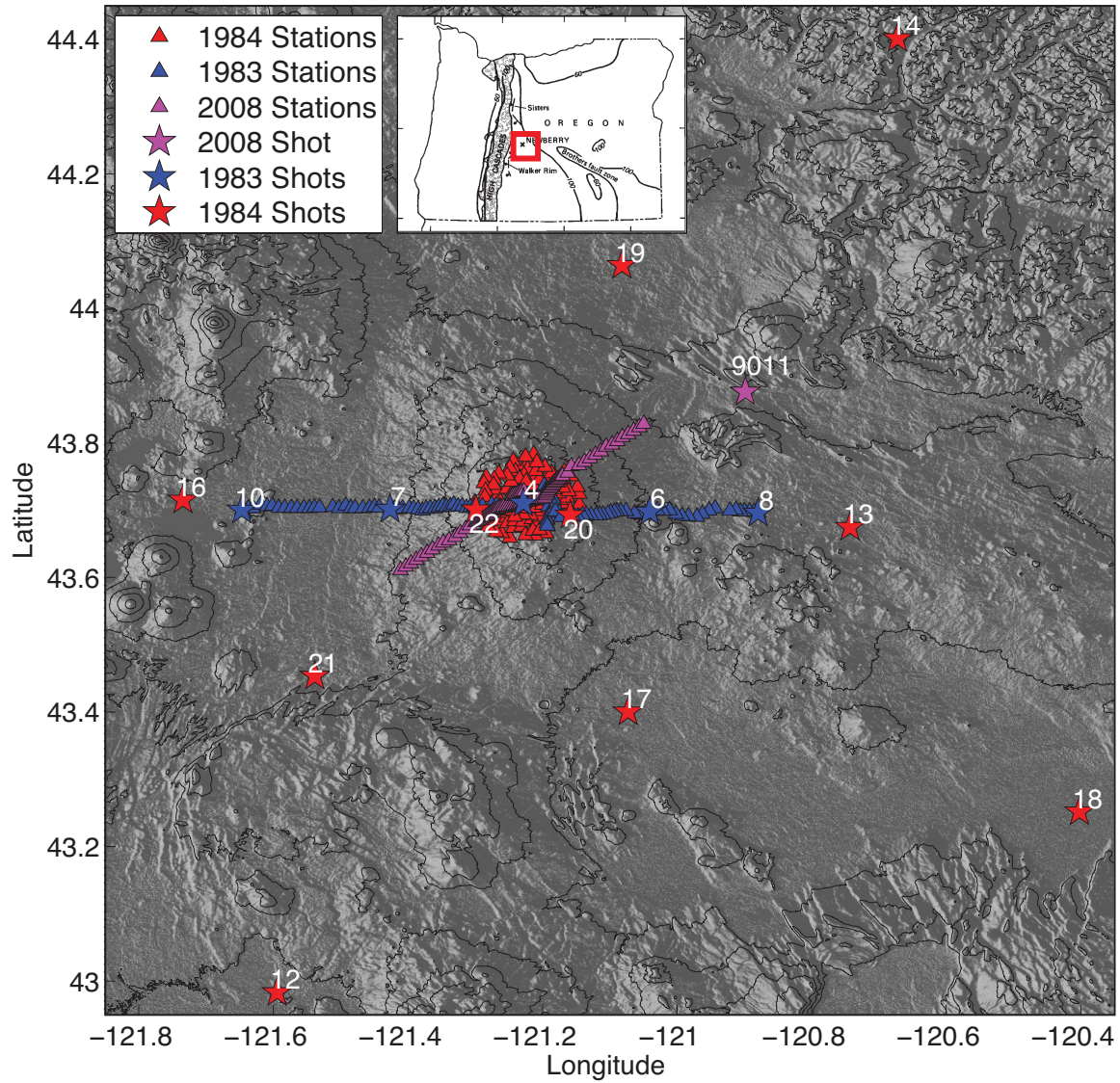


Figure 11. Map of all active-source seismic experiments at Newberry on shaded topography with a 200 m contour interval. Pink - 2008 seismic profile: 81 stations (triangles), one shot (star). Red - 1984 3D array: 122 stations, 10 shots. Blue – 1983 refraction line: 120 stations, 5 shots.

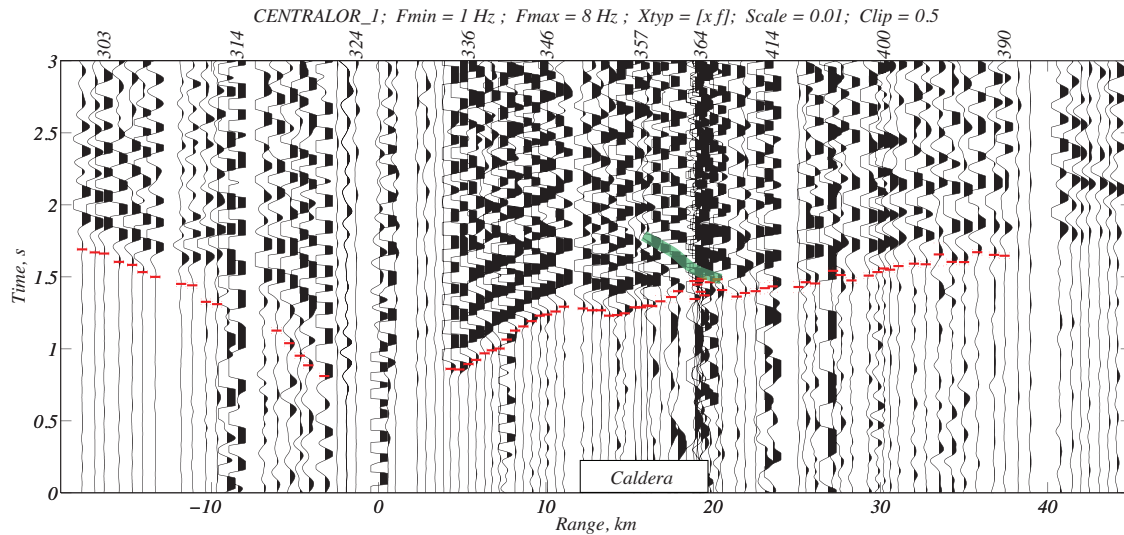


Figure 12. Example seismic record section for shot 7 (at Range = 0 km) on the 1983 seismic line. Traces are range reduced at 6 km/s. A Butterworth filter from 1 to 8 Hz reduces noise. Amplitude scaling is fixed and clipped at 0.5 km. First arrival breaks are picked as red bars. A secondary arrival is highlighted in green along a prominent phase and may be related to the secondary arrival observed in the 2008 data (Figure 8).

3.3. 1984 USGS Tomography Array

The 1984 USGS seismic array (Figure 11, red) provided the most data for the tomography study. The USGS deployed 122 vertical-component seismometers on the caldera and upper flanks in a circular grid 13 km in diameter (Achauer et al., 1988). The mean seismometer spacing was 1.6 km. Of 12 original shots, 10 were picked for this inversion. These include three large shots (2720 kg) in a triangle ~85 km from the center of the array, five large shots in a circle 39 km from the center of the array and 2 small shots (227 kg) on southeast and southwest edges of the array. Shots 11 and 15 were not picked due to data corruption and noise, respectively. Shots 20 and 22 were not used in previous tomography studies (Achauer et al., 1988; and Zucca and Evans, 1988) because they were too close to the 1984 seismic array for the ray-tracing methods used (Achauer et al., 1988). Data from shot 13 is shown for example in Figure 14.

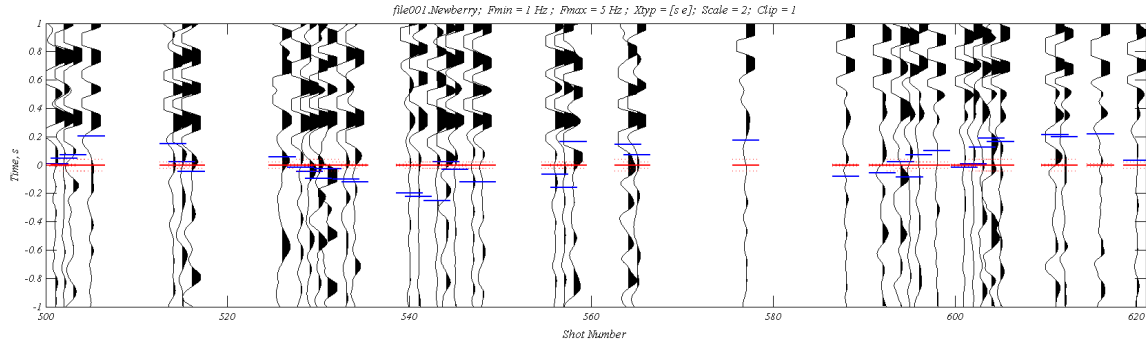


Figure 13. Example record section plotted by station number for shot 13, 1984 USGS array. Seismic traces are aligned by travel time (red bars). Noisy, unpicked traces are removed because they can't be aligned. A Butterworth filter of 1-5 Hz reduces noise. Travel time picks are red while initial predictions for a 1D velocity model are blue. Where the first break is obscure, the pick is estimated at a consistent distance ahead of an identified later phase and assigned a greater error interval (dashed red bars).

3.4. Obtaining First Arrivals

In total, 1007 P-wave first-arrival travel times were consistently identified from the three different data sets. First arrival picks (Appendix A) were made in Upicker, a MATLAB seismic analysis code developed by William Wilcock at the University of Washington. The seismic data were filtered with a zero-phase, Butterworth, band-pass filter windowed on the signal's dominant frequency. Generally, a 1 to 8 Hz window isolated a 5 Hz signal from most noise. Where noise still obscured the onset of the first arrival the arrival time was estimated by picking a consistent later phase and applying a correction. Cross-correlation further aligned picks on data with a clear enough signal (Figure 13). All picks were visually assigned a 68% confidence interval. (The correct time was 68% likely to be within the error bars, or 95% likely to be within an interval twice the error bars.) 543 picks had an error (confidence interval) of 10 ms, 292 picks had an error of 20 ms, and 171 picks had a greater error. For the 1984 array, the first arrivals

were especially difficult to follow in range or azimuth sections. These picks were iteratively compared to model predictions on station-sorted record sections (Figure 13) and residual surface plots (Figure 14) to ensure that they followed a consistent phase.

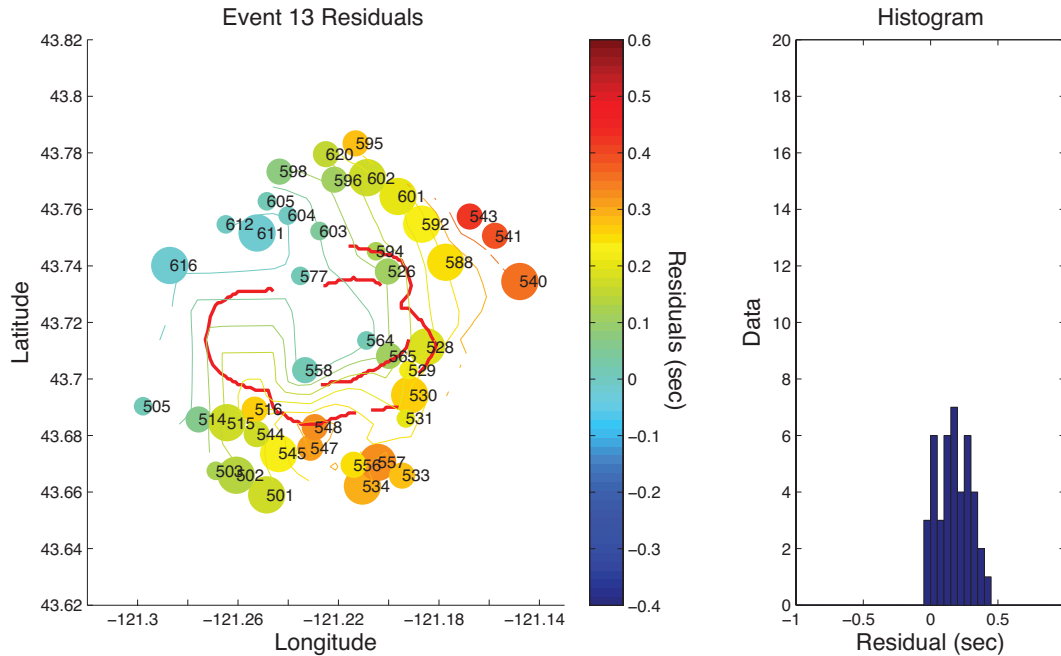


Figure 14. (Left) Map-view plot of residuals by station location for event 13, 1984 USGS array. Residuals (circles) are plotted by station location. The residuals are calculated by subtracting initial model predictions (blue picks, Figure 13) from observations (red picks, Figure 13). Hot colors are delayed while cool colors are early with respect to initial model predictions. Smaller circles show higher pick uncertainty while larger circles show lower pick uncertainty. Event 13 was 20 km east (Figure 11) of the caldera. Caldera ring faults are marked in red (Macleod et al., 1995). (Right) Histogram of residuals.

CHAPTER IV

TOMOGRAPHIC METHODS

The tomographic method obtains an improved velocity model through iterations of two steps: the forward problem and the inverse problem. The forward problem calculates travel-time predictions and ray paths using Stingray, a MATLAB accessed Fortran code developed by Doug Toomey at the University of Oregon. Stingray calculates and stores travel times and ray paths throughout the velocity model (converted to a slowness model) using graph theory, efficiently calculating travel times to all stations at once for a single event. The predicted travel times are subtracted from the observed travel times to obtain residuals, which are inverted to solve for slowness perturbations (slowness is the inverse of velocity) to the initial model, resulting in an improved velocity model.

The tomographic inversion first requires an initial velocity model that is close to the actual structure. The initial velocity model is a one dimensional (1D, velocity varied with depth) model based on the seismic refraction work of Catchings and Mooney (1988), as shown in Figure 15. The layered model is modified to obtain smooth gradients that spread rays evenly by depth (Figure 16). To obtain an initial model that represents average velocities at each depth, preliminary inversions are run with the travel-time data and then averaged to a 1D velocity model (Figure 15). This method is more successful than a 1D tomographic inversion because the velocity model can be subjectively

smoothed to remove local minimums and maximums in the velocity/depth curve that could trap or split rays, respectively. The averaged, 1D velocity model is assigned to a dense, 3D model grid with nodes spaced 200 m in the x and y directions and 100 m in the z direction. The dense grid spacing allows more precise ray paths to be connected between grid nodes. Also, the grid is hung on an elevation surface so that the forward problem produces travel times that account for topography. The predicted travel times from the initial model are then subtracted from observed travel times to obtain the travel-time residuals used in the inverse problem.

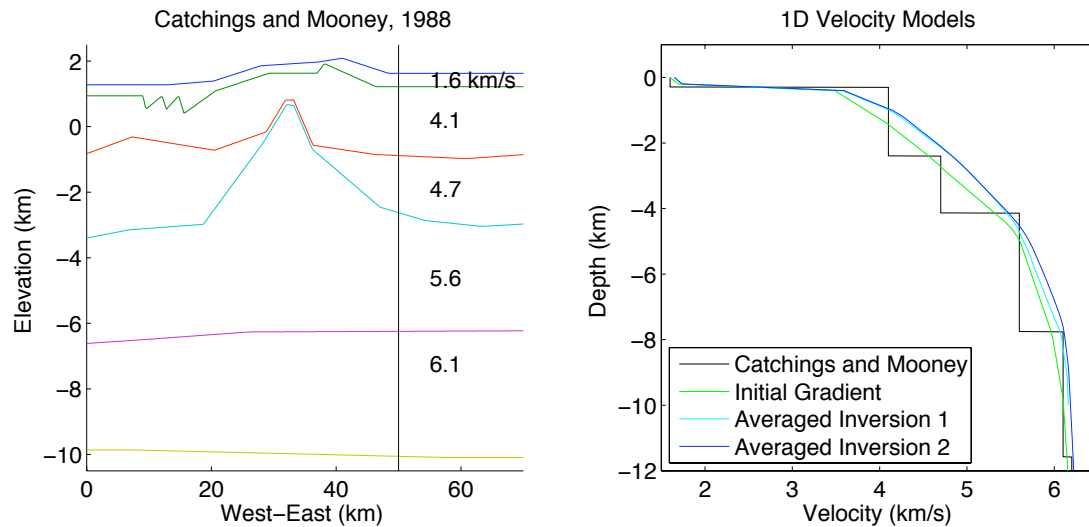


Figure 15. (left) Velocity layer model from Catchings and Mooney (1988). Newberry Caldera lies between 30 and 38 km. The vertical black line at $x = 50$ indicates the location of the 1D velocity profile shown in the diagram to the right. (right) 1D initial velocity model profiles used in the inversion. The initial gradient model (green) was estimated from the Catchings and Mooney velocity model. Successive 3D inversions were averaged to obtain better 1D initial models (cyan and blue).

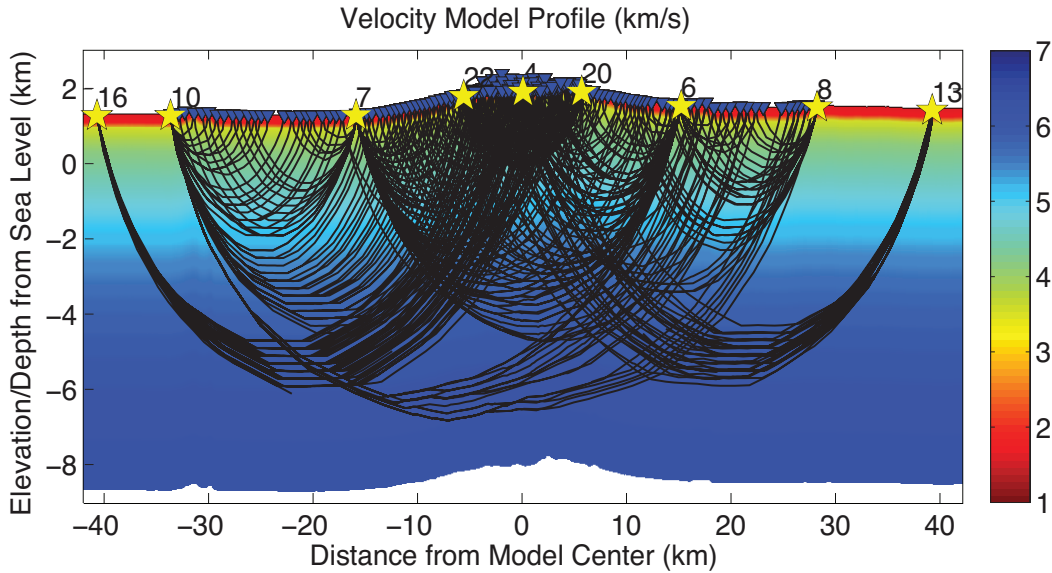


Figure 16. Ray paths through the initial 1D velocity model along a west-to-east profile 2 km south of the caldera center. Only ray paths, stations (triangles), and shots (stars) within 3.5 km of the profile are shown.

The tomographic inverse problem solves for slowness perturbations (slowness is the inverse of velocity) to the initial model using the travel-time residuals and ray paths calculated by the forward problem. The inverse problem is solved with Tomolab, a MATLAB tomography program written by Doug Toomey. Tomolab estimates slowness perturbations on a perturbational model that may be sparser than the ray-tracing model. The perturbational model nodes were spaced 400 m in the x and y directions and 200 m in the z direction. Although the perturbational model was sparser than the ray tracing model, it was still under-constrained by the data and parameterized finer than the expected resolution of ~ 1 km, estimated by dividing seismic velocity, ~ 5 km/s, by frequency, ~ 5 Hz. A more detailed model could be obtained in this situation while avoiding instabilities and unrealistic slowness perturbations by applying constraints to the inverse problem. Traditionally, the inverse problem finds a least squares solution that minimizes the travel-time residuals. A weighted least squares solution minimized the

travel-time residuals divided by the square of their pick errors, giving more weight to residuals associated with smaller pick errors.

To avoid obtaining a solution with unrealistically large slowness perturbations, a damping constraint penalized perturbations relative to the slowness model of the previous iteration (the creeping technique). In addition, unrealistically large slowness gradients were penalized by horizontal and vertical smoothing constraints. A smaller vertical smoothing constraint allowed greater slowness variations in the vertical direction than in horizontal directions. The values of these constraints were varied and tested through more than 20 inversions. The best constraint values neither over-penalized desired structure nor allowed unrealistic slowness anomalies or large gradients to emerge. Finally, the resulting slowness model is converted back to a velocity model. For a detailed discussion on solving the non-linear, ill-conditioned tomography problem see Toomey et al. (1994).

In addition to solving for slowness perturbations, the inversion solved static corrections for distant events. Static corrections are time constants that correct for the effects of structure outside the region of the velocity model where ray paths cross. A static correction was assigned to each of eight events located far from the constrained region. Event statics were not applied to all events in order to retain absolute velocity information along some ray paths, and still recover absolute velocity structure in the constrained area.

CHAPTER V

TOMOGRAPHY RESULTS

The tomographic analysis recovered heterogeneous velocity structure beneath Newberry Volcano. The inversion settings include the number of iterations, the values of the damping and smoothing constraints, and the sources for which time statics are included in the inversion. The velocity structure obtained in the tomography model includes a shallow low-velocity zone beneath the caldera, a shallow high-velocity ring surrounding this low-velocity zone, a broader high-velocity zone beneath the high velocity ring, and finally a poorly-recovered low-velocity anomaly below 3 km depth beneath the caldera. The origin of these velocity anomalies is discussed in Chapter 6.

5.1. Inversion Settings

The velocity model was improved by iterating tomographic inversions until a stable velocity model was reached. On the eighth and final iteration the weighted RMS residual misfit was reduced from an initial misfit of 207.2 ms to a final misfit of 20.5 ms. This represents a variance reduction of 99%. The misfit reduction between iteration seven (weighted RMS misfit 21.4 ms) and iteration eight was only 4%. Further iterations would reduce the misfit by negligible amounts.

Smoothing and damping constraints for the inversion were tested and adjusted to obtain a velocity model that best fit the observed travel times while restricting unrealistic velocity perturbations (instabilities) in poorly constrained regions. The damping constraint was held constant at 1 while the smoothing constraints were adjusted. In the

final inversions presented here the horizontal and vertical smoothing constraints were 200 and 100, respectively. Less vertical smoothing was imposed because velocity is expected to change more rapidly with depth than in the horizontal direction.

Additional settings optimized the inversion. The nodes of the perturbational model were assigned a uniform uncertainty of 0.1, which penalized perturbations greater than 10%. The iterations were allowed to creep, that is, the velocity model was damped relative to the velocity model of the previous iteration and not relative to the initial model. This allows more localized velocity perturbations to emerge over successive iterations. Finally, the inversion included source static terms for nine of the sixteen events as shown in Table 1.

Table 1. Description of the source events. Ranges are given in distance to the center of the caldera. Shot sizes are given in kg TNT equivalence. Events at closer range and with larger source size had more picked travel times due to higher signal-to-noise. Event 11 was not picked due to data corruption and Event 15 had an insufficient signal-to-noise ratio. Static timing corrections were calculated in the tomographic inversion for events lacking nearby stations.

Event	Year	Range (km)	Size (kg)	# of Picks	Static time (s)
4	1983	1.0523	900-1800?	61	no
6	1983	15.46	900-1800?	63	no
7	1983	15.972	900-1800?	78	no
8	1983	28.379	900-1800?	21	no
10	1983	33.67	900-1800?	68	no
11	1984	38.721	2720	N/A	N/A
12	1984	87.064	2720	38	0.20
13	1984	39.593	2720	42	0.23
14	1984	87.896	2720	69	-0.40
15	1984	7.1248	227	N/A	N/A
16	1984	40.645	2720	79	0.34
17	1984	37.74	2720	99	0.38
18	1984	84.825	2720	58	0.23
19	1984	40.033	2720	26	0.20
20	1984	6.4904	227	54	no
21	1984	38.702	2720	101	-0.04
22	1984	5.9423	227	83	no
9011	2008	31.808	907	67	0.12

5.2. Low Velocity Anomalies

The final P-wave tomography model reveals two central low-velocity anomalies at separate depths as well as a broad low-velocity region south and east of the caldera. At 0 to 2 km depth, a central low-velocity zone resides within a high velocity ring and beneath the caldera (Figure 17). This inner-caldera low-velocity zone is 0.5 km/s slower than the average velocities at 1 km depth, and 1 km/s slower than the surrounding high-velocity ring. For consistency, I report the largest magnitude of velocity anomaly observed in a feature since the damped inversion tends to underestimate velocity structure. Above 1 km depth, the low-velocity zone appears concentrated into an east-west pair of low-velocity anomalies, which merge into a central anomaly below 1 km depth. At 1 km depth the low-velocity zone is roughly 4 km wide EW and 2 km NS, surrounded by the high-velocity ring. This low-velocity zone ends near 3 km depth.

Low-velocities reappear beneath the caldera below 4 km depth, but this second low-velocity anomaly is poorly recovered. A third, much broader low-velocity region extends south and east of the caldera rim in the upper 4 km (Figure 17). At 1 km depth this southern low-velocity zone is 0.6 km/s slower than the average velocity. The full extent of this low-velocity region is unclear and could extend beyond the edge of the resolved region.

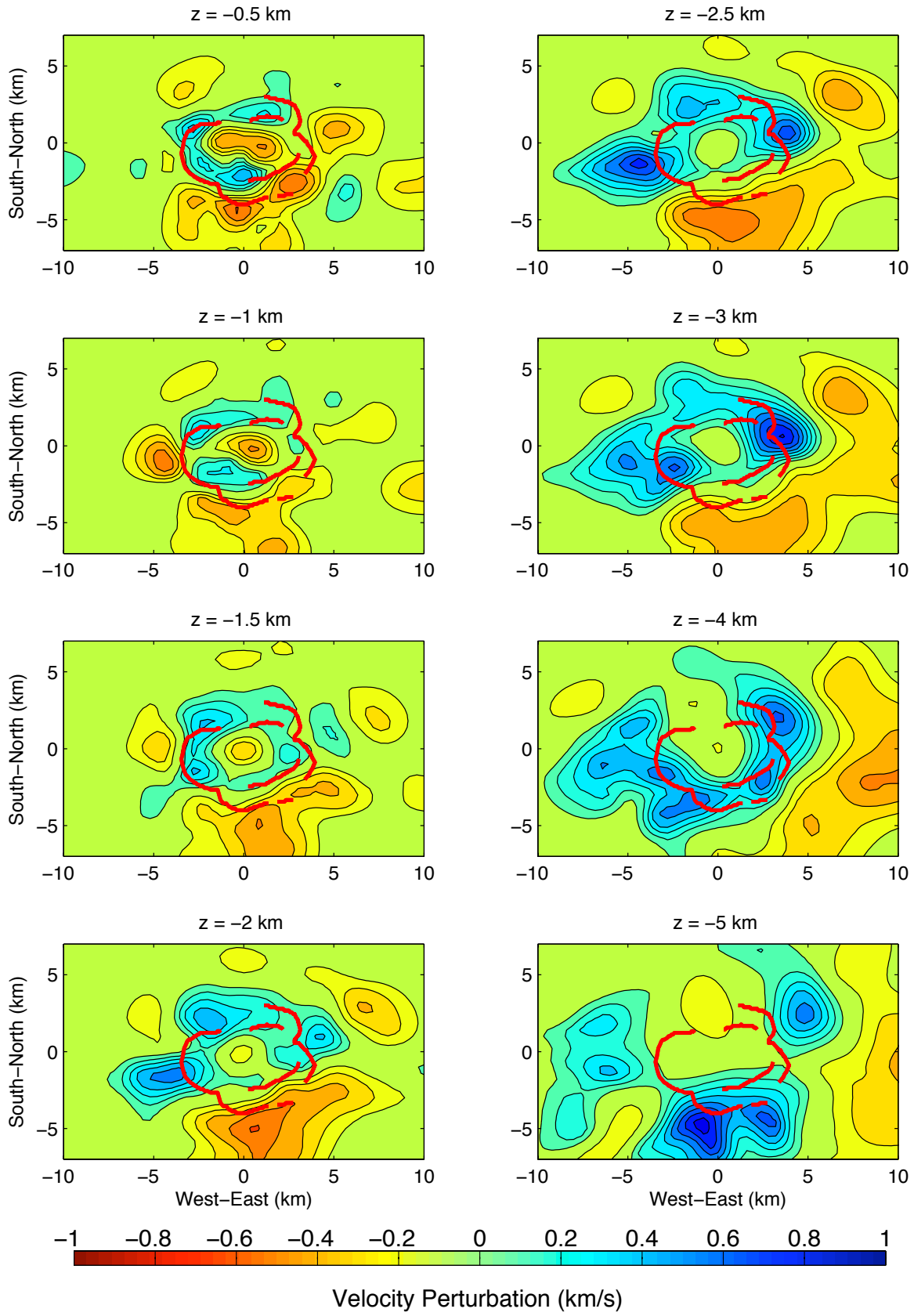


Figure 17. The final velocity model shown in depth sections at various depths from the surface. Velocities are colored as perturbation from the initial 1D velocity model with 0.1 km/s contours. Caldera ring faults are marked in red (Macleod et al., 1995).

5.3. High Velocity Anomalies

The tomography model recovers high-velocity anomalies at different depths. In the uppermost crust, a high-velocity ring-like anomaly follows the inner caldera ring faults (Figure 18). This high-velocity ring is 7 km east-west by 5 km north-south and extends to 1.5 km depth. At 1 km depth the ring is at most 0.5 km/s faster than the average velocity. At 2 km depth the ring merges with a broad high-velocity region. The broad high-velocity region has its highest velocities concentrated east and west of the caldera. The eastern high-velocity anomaly is 4 km wide east-west at 3 km depth and 1 km/s faster than the average velocity. The western high-velocity anomaly is 8 km wide at 3 km depth and 0.6 km/s faster than the average velocity. Below 3 km depth the high-velocity zone spreads out and may be influenced by the ray geometry.

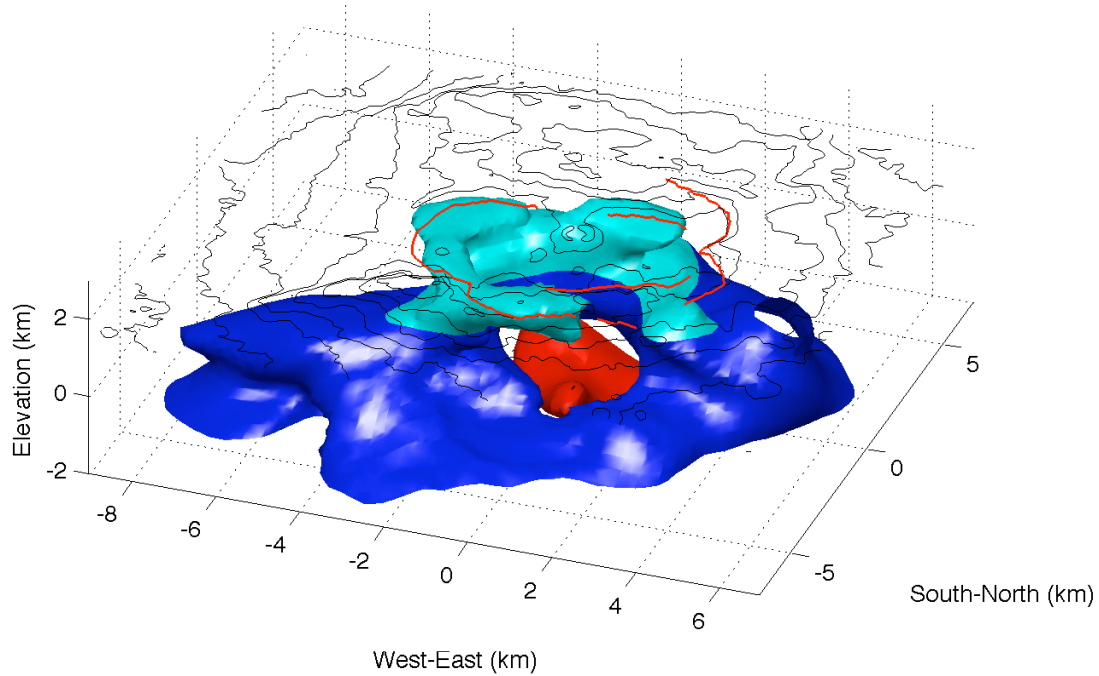


Figure 18. 3D representation of velocity anomalies illuminated from the southeast. High-velocity structure is colored in light blue above 1.5 km depth and in dark blue below 1.5 km depth, contoured at +0.2 km/s velocity perturbation. The color difference distinguishes a possible structural difference between the shallow high-velocity ring and broader, deeper high-velocity region. The central, low-velocity body is colored red from 3 to 5 km depth contoured at -0.1 km/s velocity perturbation. The shallow low-velocity region within the caldera is not shown. The view is from 20° east of south and 30° above horizontal. At the surface, red lines show inferred ring fractures and black lines are 100 m topography contours.

CHAPTER VI

DISCUSSION

The tomography results reveal a heterogeneous velocity structure beneath Newberry volcano, which I attribute to structural features emplaced during Newberry's history. The anomalous features include 1) a high-velocity, ring-like anomaly within the caldera, interpreted as either intruded ring-dikes or possibly cone-sheets; 2) a shallow, low-velocity zone within this ring and beneath the caldera, interpreted as tephra deposits and a collapsed region composed of lava flows; 3) a broad high-velocity region below 2 km depth, interpreted as an intrusive complex; and finally 4) a central, low-velocity zone below 3 km depth that is inferred to be a magma chamber or a fractured pluton. The velocity variation of these features may result from differences in porosity, lithology, temperature and/or partial melt. The interpretation of these features reflects the integrated history of Newberry Volcano involving at least one caldera collapse along the inner ring faults, east-west extension, north-south trending rift zones facilitating eruptions, and a central magma chamber between 3 and 6 km depth. The following sections discuss each observed velocity feature and its structural interpretation.

6.1. Shallow Volcanic Structure

6.1.a. Inner-Caldera Low-Velocity Zone

A low-velocity zone centered beneath the caldera is interpreted as caldera fill deposits overlying a collapsed region composed of lava flows. Low velocities are interpreted as porous caldera fill deposits in the upper 500 m, where drill core data report

layers of tuff (Keith and Bargar, 1988). Below 500 m lava flows dominate, either post-caldera flows or the top of the collapsed region. This lithological boundary is not visible in the tomography image. The velocity of the lava flows must be similar to the tuffs, with their low-velocity also attributed to porosity. Keith and Bargar (1988) report vesicles and fractures in various lava-flows below 500 m depth. It is notable that Keith and Bargar (1988) do not indicate consistent fracturing across layers, which could be expected from a traumatic collapse event. Either the collapsed region/caldera fill boundary lies below the 932 m extent of the Newberry 2 drill hole and is seismically undetectable, or the lava-flows beneath 500 m depth subsided as a coherent block during “piston collapse.” The collapsed region probably extends to 3-4 km depth terminating at the top of an expected magma chamber or pluton.

6.1.b. High-Velocity Ring

A high-velocity ring surrounding the inner-caldera low velocity zone is interpreted as an intrusive ring complex. This could be either ring-dikes or cone-sheets encircling a caldera or crustal magma chamber (Anderson, 1937). Because the high-velocity ring circles the caldera along a ring of caldera collapse faults (figures 17 and 18), it is probably caused by ring-dikes or cone-sheets intruded along these faults. These structures are generated by two different modes of caldera collapse and/or resurgence. In the case of ring dikes, the subsided region may have stayed a relatively intact block during “piston collapse” while magma extruded around the edges of this block, solidifying as vertical to outward dipping ring-dikes (e.g. Cole et al., 2005; Lipman, 1997; Marti et al., 1994). In the case of cone-sheets, the subsided region may have crumbled and collapsed into a narrow magma chamber during “funnel collapse,” with

inward-dipping cone-sheets emplaced around the edge of the subsided zone (Achauer et al., 1988), possibly during a later episode of resurgence.

Both cone-sheets and ring-dikes have been observed in eroded calderas (e.g. Anderson, 1936), but rarely have they been observed in geophysical studies (Bauer et al., 2003, Nercessian et al., 1984, Aster and Meyer, 1989, Gudmundson and Högnadóttir, 2007). Gravity data at Newberry (Gettings and Griscom, 1988) and this P-wave velocity study of Newberry provide conclusive geophysical evidence of an intrusive ring complex. Despite its clarity, it is still difficult to distinguish whether the high-velocity ring corresponds to ring-dikes, as interpreted by Gettings and Griscom (1988), or cone-sheets, as interpreted by Achauer et al., (1988).

6.1.c Synthetic Ring Test

In the tomography model, the high-velocity ring appears 1 km thick at 1 km depth; however, a synthetic test model shows that the actual ring structure may be thinner and faster than that recovered by the inversion due to the effects of smoothing and damping. I designed a synthetic model with a 500 m horizontally thick, positive 10% velocity ring to test the inversion's ability to recover a thin high-velocity ring. These high velocities represent the lower porosity of crystalline intrusive rock relative to its surroundings (lava flows and tephra deposits). The test models the ring to 2.5 km depth, rather than the 1.5 km observed depth of the high-velocity ring, because an actual intrusive ring complex likely extends down to a magma source (expected at ~3-6 km depth) but becomes indistinguishable from the broader high-velocity region below 2 km depth. A negative 10% low-velocity zone within the ring represents caldera fill and a

subsided region. The synthetic test obtains travel times by ray tracing through the model using the source and receiver geometry of the combined seismic experiments. Gaussian random noise is introduced to the synthetic travel times with a standard deviation of 0.02 seconds to simulate human pick error; a value chosen because the mean standard error assigned to picks was 0.017 seconds.

The synthetic travel times were then inverted using the same settings as the actual inversion to investigate how well the artificial structure can be resolved. The 500-m-thick-ring test recovers a smoothed, 1-km-thick ring with a maximum velocity 0.6 km/s faster than average, a recovery greater than the synthetic ring's velocity (Figure 19). Note that the ring has smeared downward and inward but with a lower magnitude velocity anomaly. The recovered velocity anomaly compares well with the observed high-velocity ring so the 500 m synthetic ring may be a good model of the actual structure while the observed high-velocity ring is likely widened by the horizontal smoothing constraint.

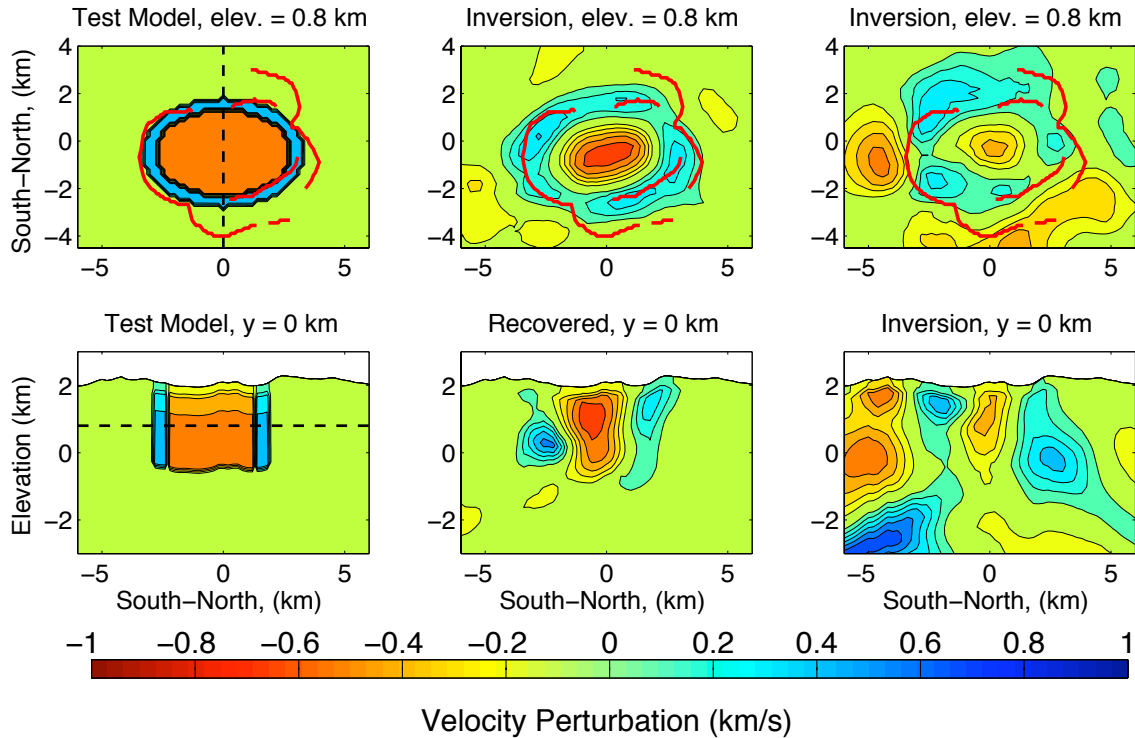


Figure 19. (Left column) Synthetic model with a 500 m thick, 10% high-velocity ring (4.6 km/s at 1 km depth) extending to 2.5 km depth below the surface. A 10% low-velocity zone (3.7 km/s at 1 km depth) lies within the ring. (Middle column) Profiles through the recovered model, the model obtained by tomographic inversion of travel time data calculated for the synthetic model. (Right column) Profiles through the tomography model obtained from the real data. Notice that the vertical ring is recovered with an apparent inward dip that is not present in the starting model. (Upper row) Map view sections at 0.8 km elevation, base of the Newberry volcanic pile. (Lower row) East-west sections at $y = 0$ km.

The tomography results cannot distinguish between ring-dikes or cone-sheets.

While the dip could be used to distinguish between ring-dikes and cone-sheets, the synthetic tests show that the dip of the high-velocity ring is not well resolved. The originally vertical high-velocity rings (90° dip) are recovered with an apparent inward dip of $71 \pm 21^\circ$ in the south and $71 \pm 5^\circ$ in the north (Figure 19). The thickness range is also consistent with either ring-dikes or with cone-sheets concentrated along the ring faults. Ring-dikes range from 50 to 2000 m in thickness (Anderson, 1937). Individual cone-

sheets are only 3 to 15 m thick but congregate in swarm regions up to 5 km thick (e.g. Schirnick et al., 2010; Klausen 2004; Ancochea et al., 2003). The seismic data are not consistent with a broad cone-sheet swarm, but could be consistent with the interpretation by Achauer et al. (1988) of cone-sheets intruded within inward-dipping ring-faults. I interpret the high-velocity ring as an intrusive complex that follows the caldera ring-faults.

6.1.d. Caldera Collapse History

The high-velocity ring at Newberry contributes to our understanding of Newberry's history. An intrusive ring complex follows ring-faults caused by at least one major collapse event in Newberry's history. The collapse subsided an elongated central region roughly 5.5 ± 1.5 km east-west and 4 ± 1 km north-south. It is surprising to find a single intrusive-ring complex at Newberry, which from the surface appears to have had multiple collapses on overlapping sets of ring faults. In fact, ash flow tuff deposits give evidence for at least three different collapse episodes: the tuff of Paulina Creek Falls (~ 0.75 ka), the tuff of Tepee Draw, and the tuff of Brooks Draw (Jensen et al., 2009); the later two tuffs are thought to be ~ 200 ka and 300 ka, respectively (J. Donnelly-Nolan, 2010, personal communication). To reconcile the single intrusive ring-complex observation with multiple ash flow tuffs, multiple collapses may have reused the same ring faults (J. Donnelly-Nolan, 2010, personal communication). Alternatively, it is possible that only one of the collapse episodes had the right conditions to form an intrusive ring complex (Legros et al., 2000).

6.1.e. Local Stress Field

The elongation of Newberry's caldera and the high-velocity ring is consistent with an extensional environment. Both the high-velocity ring and the inner ring faults have an ellipsoidal shape with an east-west major axis. This is consistent with an east-west extensional stress field that is manifested at Newberry by north-south trending fault zones: the Sister's fault zone to the north and the Walker Rim fault zone to the south (Fitterman, 1988). Physical modeling of caldera collapse in extensional settings predicts the formation of ellipsoidal ring-faults with a major axis parallel to regional extension (Acocella et al., 2004). Although Acocella et al. (2004) finds that an elongated caldera could result from a circular magma chamber, Bosworth et al. (2000) suggests that extension would cause an elongated magma chamber. I adopt an east-west elongation to the high-velocity ring and the other velocity features in synthetic tests.

6.2 High-Velocity Region Below 2 km Depth

I interpret the broad high-velocity region beneath 2 km depth as an intrusive complex different from the high-velocity ring above it. Despite its ring-like distribution about the caldera, the deeper high-velocity region clearly differs from the shallow high-velocity ring in thickness and magnitude. At 2.5 km the high-velocity region extends 15 km across east-west and 8 km north-south. The deeper high velocity region also differs in having higher velocities concentrated to the east and west of the caldera. At 2.5 km depth (Figure 17) the magnitude of the eastern high-velocity region is 5.7 km/s and the western high-velocity region 5.6 km/s.

The high-velocity region west of the caldera has been detected previously in the tomography study of Achauer et al., (1988) as well as in the refraction model of Catchings and Mooney (1988) (Figure 5). This feature is also consistent with a high-gravity anomaly in the residual gravity anomaly map of Gettings and Griscomb (1988) (Figure 6). The correlation of high-gravity and high-velocity anomalies is consistent with a concentration of intrusions west of the caldera and Achauer et al. (1988) interpreted this feature as a mafic feeder complex.

Unlike the western high-velocity region, the high-velocity region recovered east of the caldera below 2 km depth was not found in previous seismic or gravity studies at Newberry. This high-velocity anomaly is well-sampled by the 2008 seismic profile. However, it is also sampled by the USGS 1983 and 1984 data sets; a tomographic inversion run without the 2008 travel times still recovers the eastern high-velocity region though with smaller magnitude: 5.5 km/s as opposed to 5.7 km/s at 2.5 km depth (Figure 20). Perhaps the travel time data used in previous inversions (Achauer et al., 1988; Catchings and Mooney 1988) did not reveal this feature until I reevaluated these travel times for the current inversion.

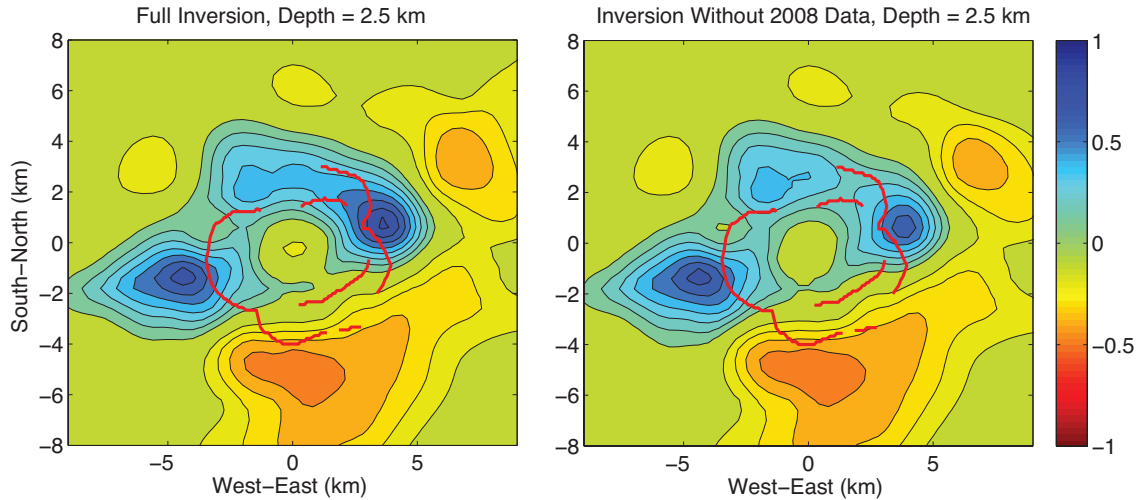


Figure 20. (Left) Depth section at 2.5 km through the final velocity model and (Right) through the velocity model resulting from an inversion with the 2008 seismic data removed. The eastern high-velocity peak is reduced by 0.2 km/s in the latter inversion.

It is perplexing that the newly resolved eastern high-velocity anomaly is not associated with a gravity high, but rather with a low-gravity trough (Gettings and Griscomb, 1988) (Figure 21). However the residual gravity anomaly map integrates deep and shallow structure and can therefore not be directly compared to the velocity depth sections. The expected high-gravity signal of the eastern high-velocity anomaly may be overwritten by shallow, low-density structure.

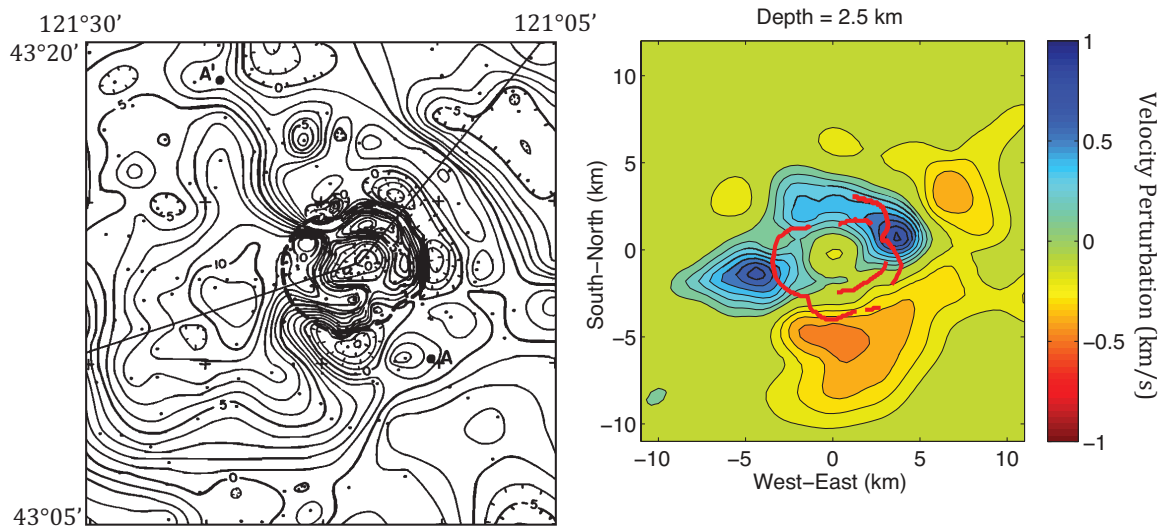


Figure 21. (Left) Residual gravity anomaly map adapted from Gettings and Griscom (1988), same as Figure 6, right panel. (Right) P-wave velocity anomaly model at -0.5 km elevation from sea level (~ 2.5 km depth), same as Figure 17, top right panel. A high-velocity region to the west of the caldera may correspond to a high-gravity anomaly west of the caldera. The high-velocity region to the east does not correlate with gravity.

6.3 Low-Velocity Body Below 3 km Depth

I infer the presence of a low-velocity anomaly between 3-6 km depth that may be caused by a magma chamber or a fractured pluton. The final tomography model recovers a negative 0.1 km/sec velocity anomaly (absolute velocity 5.3 km/s) below the caldera at 4 km depth. The inversion most likely underestimates the full magnitude of the velocity anomaly, as discussed in section 1.3. Although tomography has difficulty recovering small, low-velocity bodies, Flecha et al. (2004) show that an examination of ray-path coverage can detect and locate low-velocity bodies. I find evidence for a low-velocity body beneath 3 km depth at Newberry based on the deflection of ray paths and consistency of tomographic inversion results with synthetic tests. Synthetic tests also

show that the low-velocity body below 3 km depth is distinct from the shallow inner-caldera low-velocity zone and may be much greater in magnitude. The synthetic tests cannot constrain whether a magma chamber or a fractured pluton causes the low-velocity body.

6.3.a. Ray Path Deflection

The tomography study recovers the effects of ray bending around the low-velocity body. Figure 22 shows ray bending in the 2008 data. Ray bending is not evident in the initial velocity model but emerges over several iterations of the tomographic inversion. Starting ray paths through the initial velocity model underestimate travel times where ray bending produces longer ray paths in the actual structure. To account for travel-time differences, the tomographic inversion applies velocity perturbations along the starting ray paths. In subsequent iterations, the ray paths are recalculated and now deflect around the low-velocity anomalies applied along the starting ray paths. Tomography recovers the effects of ray bending by recalculating ray paths over multiple iterations.

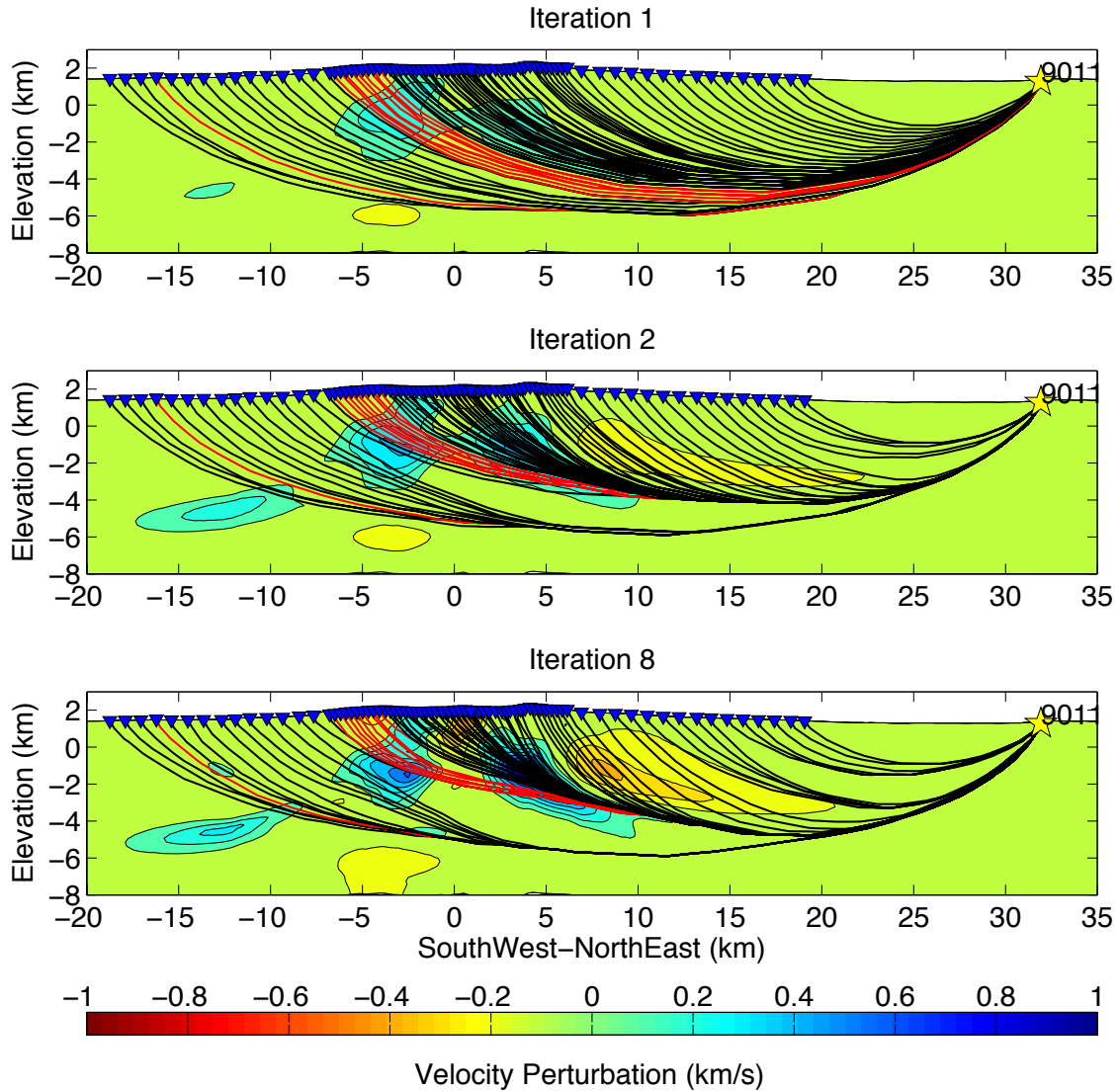


Figure 22. Ray bending around a low-velocity body at 3-6 km depth beneath the caldera. Profiles show velocity perturbation for successive iterations of the tomographic inversion. Ray paths (black and red lines), stations (triangles) and the shot (star) are shown along the profile of the 2008 seismic experiment. (Top) The first iteration inversion shows initial ray paths. (Middle) The second iteration shows ray paths that bend above and below a region of average velocity between -2 and 2 km horizontally and 5-6 km depth (-3 to -4 km elevation). (Bottom) The eighth and final iteration shows ray bending that has fully developed around an average velocity region between -3 to 3 km horizontally and 3-6 km depth (-1 to -4 km elevation) with a weak low-velocity anomaly at 4 km depth. A bundle of red ray paths appears to pass above the low-velocity anomaly but actually diffracts around the near side. Red ray paths did not have travel time picks (Figure 10) due to low signal to noise, probably caused by spreading of energy where rays bend around the low-velocity region.

The 2008 seismic data in Figure 22 are not ideal in that a group of travel times could not be picked due to low signal to noise (Figure 8). The corresponding unpicked ray paths are shown in red in Figure 22. However, the data gap does not invalidate the recovered low-velocity body because low amplitude and low signal-to-noise are consistent with the presence of a low-velocity body. In Figure 22 it is evident that the rays in red spread out from a tight bundle after passing above the low-velocity body (also see Figure 1, dPa). This ray spreading suggests that the wavefront energy also spreads out. The wavefront amplitude becomes weaker in the region of spread rays and picking the travel times in this low-amplitude region becomes more difficult due to a lower signal to noise ratio. I choose to show the unpicked (red) ray paths in Figure 22 because they demonstrate ray bending. In addition, the tomography study has ray paths from other sources sampling this ray-bending region and low-velocity body so these results are not wholly dependent upon the 2008 data.

6.3.b. Low-Velocity Body Test

Synthetic tests also indicate that a low-velocity body causes the deflection of ray paths around a poorly-resolved region. The first synthetic test models a -40% low-velocity body (Figure 23, left column) within the averaged 1D velocity model used for the initial tomography model. The low-velocity body has dimensions 5.6 km east-west, 3.6 km north-south, and 3 km top to bottom. These dimensions are based on the previous high-velocity ring tests and estimate the lateral dimensions of the magma chamber involved in the central caldera collapse. The 3 km vertical extent is a maximum estimate for the vertical extent of a magma chamber based on the region avoided by ray paths (Figure 22).

Despite its large dimensions and magnitude, the low-velocity body is barely recovered in the synthetic inversion (Figure 23, right column). A -0.2 km/s (4%) anomaly is recovered compared to the original -40% anomaly, just 10% recovery of the original low-velocity body. The spatial recovery of the anomaly is also diminished about 4 km east-west, 3.5 km north-south, and 3 km top to bottom. The weak recovery of the low-velocity body is partly caused by a lack of ray-coverage at different angles and mainly caused by ray bending. Figure 23 shows that the model ray paths deflect around the low-velocity body (with several ray paths deflected around the near side) so that no ray paths directly sample the low-velocity body. Therefore the low-velocity body cannot be fully recovered by tomographic inversion.

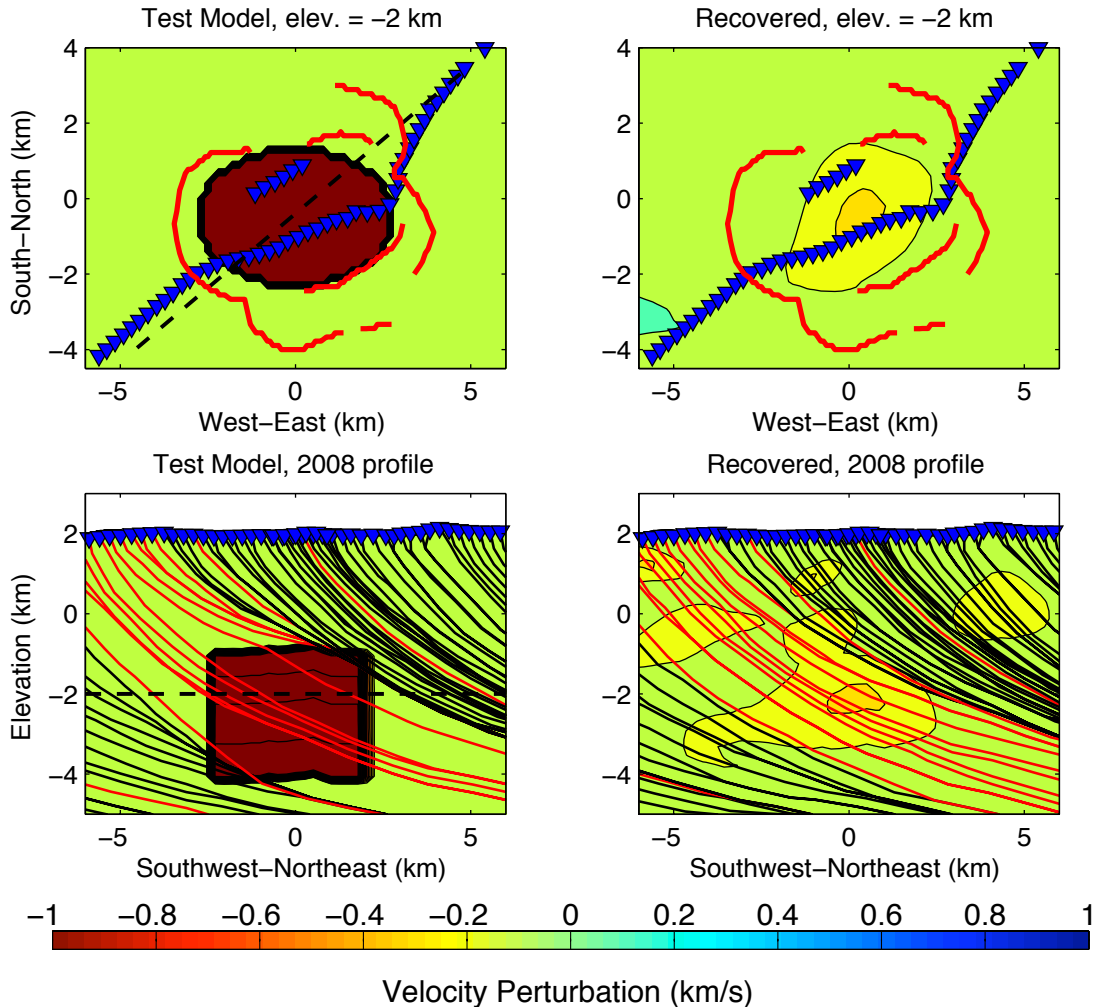


Figure 23. (Left column) Synthetic test model with a negative 40% low-velocity body at 3 to 6 km depth. The low-velocity body extends 5.6 km east-west and 3.6 km north-south. The low-velocity body has a velocity of 3.1 km/s at 3 km depth and 3.5 km/s at 6 km depth, note that this is below the -1 km/s limit of the color scale. (Right column) A 0.2 km/s (4%) low-velocity anomaly is recovered. This is only a 10% recovery of the low-velocity body and provides another example of the difficulty resolving low-velocity bodies using tomography because ray paths deflect around low-velocity bodies. Red lines: caldera ring faults. Dashed line: profile intersection. Blue triangles: stations. Black and red lines: ray paths and unpicked ray paths.

6.3.c. High-Velocity Body Test

To demonstrate that the poorly resolved low-velocity body is not a result of inadequate data coverage, a second synthetic test models a high-velocity body (Figure 24, left column). The high-velocity body has the same location and dimensions as the low-velocity body in the previous test. However, the high-velocity body has only 10% velocity anomaly as opposed to the 40% low-velocity body test. The high-velocity body test recovers a 0.4 km/s (8%) high-velocity anomaly, which is an 80% recovery (Figure 24, right column). This recovery is significantly greater than in the low-velocity test. Also, the spatial extent of the recovered anomaly closely matches of the synthetic high-velocity body. These results demonstrate the resolution inequality between a high-velocity body and low-velocity body at 3-6 km depth and show that ray coverage is not inadequate in this region.

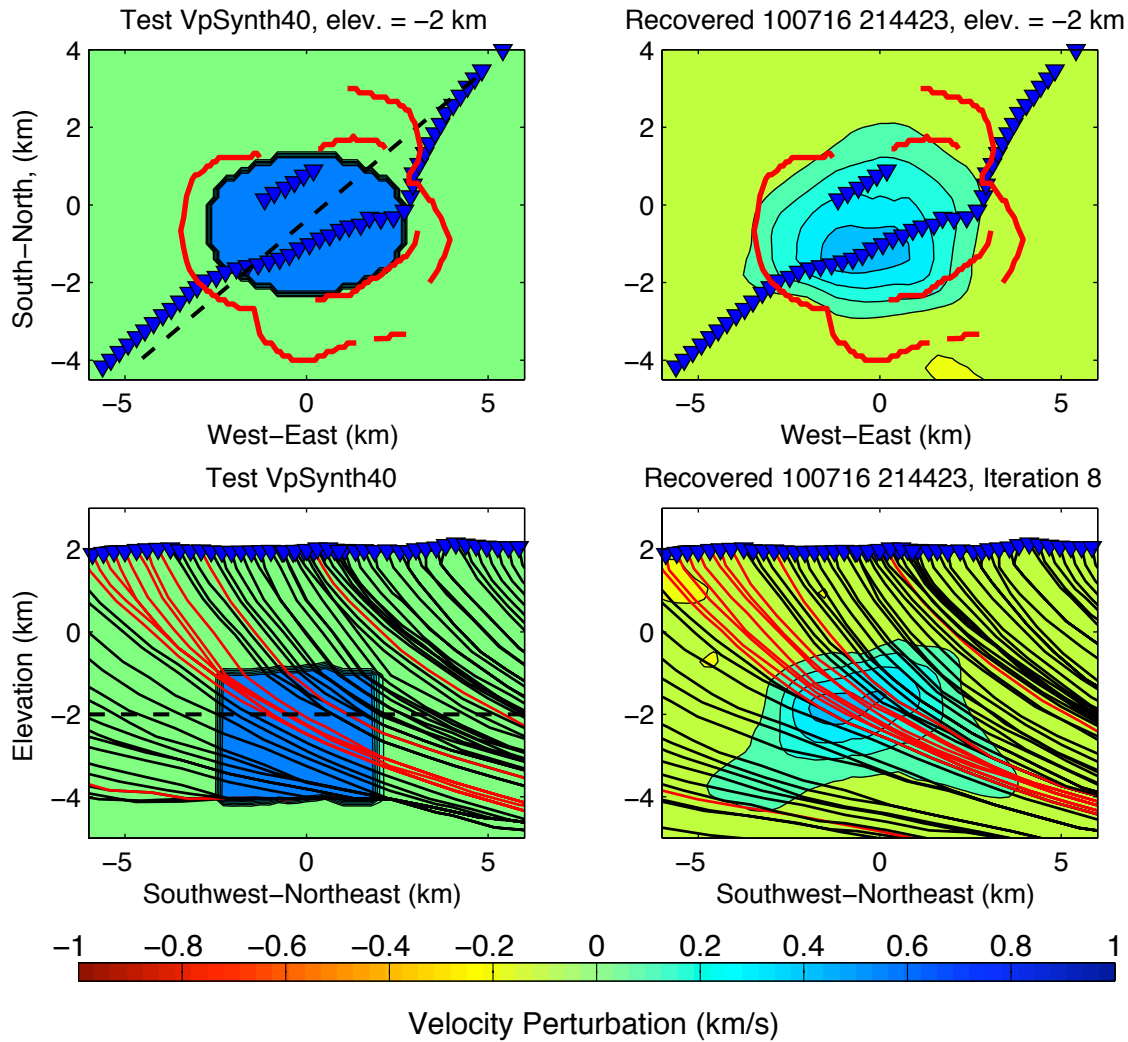


Figure 24. (Left column) Synthetic test model with a 10% high-velocity body of the same dimensions as the low-velocity body described in Figure 23. The high-velocity body has a velocity of 5.6 km/s at 3 km depth and 6.5 km/s at 6 km depth. (Right column) A 0.4 km/s high velocity anomaly was recovered, a 80% recovery. Red lines: caldera ring faults. Dashed line: profile intersection. Blue triangles: stations. Black and red lines: ray paths and unpicked ray paths.

Synthetic tests demonstrate another resolution inequality between a low-velocity body near the surface and one at depth. In Figure 19 the synthetic high-velocity ring tests includes a 10% low-velocity zone from 0 to 2.5 km depth representing caldera fill. The near surface low-velocity anomaly is well recovered because ray paths must travel

through this region to reach the stations at the surface. However, if a low-velocity body is at depth, ray paths may bend around it. To summarize, the resolution of the tomography study is better for high-velocity and shallow features but poorly resolves a low-velocity body deep enough to allow deflection of energy around the anomaly.

6.3.d. Structural Tests

A concern posed by Achauer et al. (1988) is whether the deeper low-velocity body is a distinct feature or a continuation of the collapsed region within the caldera. I address this concern by comparing two new synthetic tests to the tomography image. The tomography image shows the inner-caldera low-velocity zone separated from the poorly-resolved deeper low-velocity body by a thin zone of average velocity around 3 km depth (Figure 25, lower right panel). Both features appear distinct but it is possible that a continuous low-velocity column appears separated by resolution inequalities. Such a feature could be a collapsed region that subsided into a magma chamber deeper than 3 km depth. A synthetic test models the collapsed region as a -10% low-velocity column with lateral dimensions 5.6 km east-west and 3.6 km north-south (Figure 25, left column). The synthetic test includes a simplified volcanic structure with a +10% high velocity ring near the surface and high-velocity shoulder at 2.5 km depth. The test inversion recovers the low-velocity column as a single low-velocity anomaly focused at 2 km depth, rather than two separate low-velocity anomalies. Therefore a continuous low-velocity column is not consistent with the observed travel times.

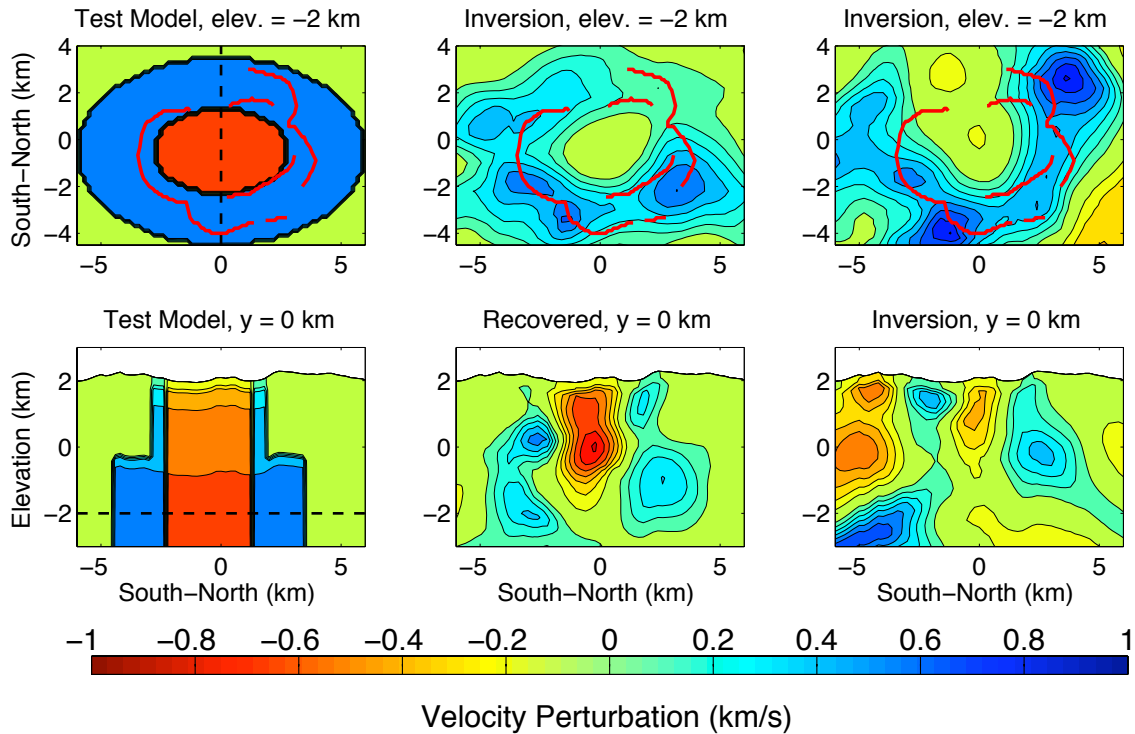


Figure 25. (Left column) Synthetic test model with a continuous -10% low-velocity column extending to 6 km depth. The low-velocity column is surrounded by simplified volcanic structure consisting of a +10% high-velocity ring to 2.5 km depth meeting a +10% high-velocity shoulder representing an intrusive complex. (Middle column) The synthetic inversion recovers a low-velocity column down to 4 km depth. (Right column) The tomographic result shows a break in low velocities at 3 km depth.

A second synthetic test more accurately reproduces the observed travel-times by including two separated low-velocity zones. This synthetic test modeled a -10% low-velocity zone down to 2.5 km depth representing the caldera fill and a collapsed region (Figure 26, right column). Beneath this lies a -40% low-velocity zone representing a magma chamber at 3 to 6 km depth with dimensions 6.6 km east-west, 4.6 km north-south. This is a maximum magma chamber volume scenario (72 km^3) that matches the lateral extent of the high-velocity ring and the caldera ring faults. A +10% high velocity layer separates the low-velocity zones and possibly represents a crystalline roof above the magma chamber. I attribute no significance to this particular structural solution and

emphasize the separated nature of the low-velocity zones. In the synthetic inversion, the separate low-velocity zones blur into an image comparable to the actual inversion. It is worth noting that the -40% low-velocity body is less well recovered (0% recovery) in this synthetic test where it is surrounded by high-velocity structure (Figure 26) than it was alone (Figure 23). This synthetic test implies that a low-velocity magma-chamber with a maximum volume of 72 km^3 could be consistent with the observed travel times, although this volume is probably unrealistic.

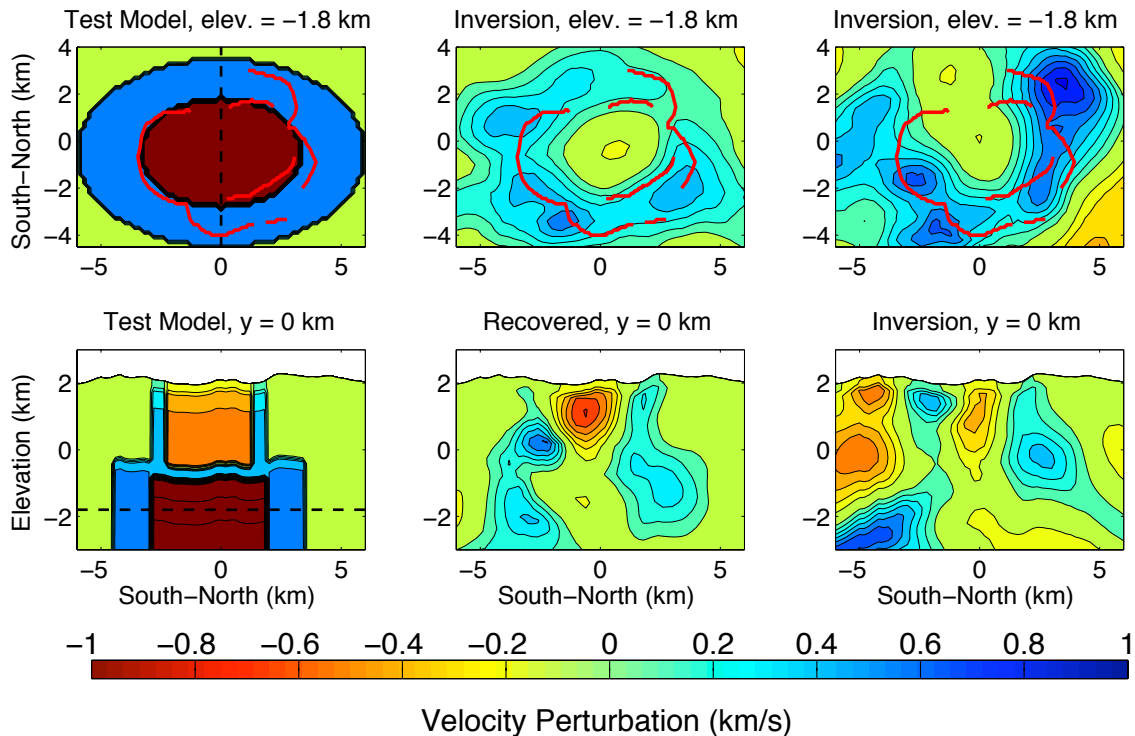


Figure 26. (Left column) Synthetic test model with a separated -10% low-velocity column to 2.5 km depth and a -40% low velocity body from 3 to 6 km depth with dimensions 6.6 km east-west and 4.6 km north-south. Note: the -40% low-velocity body is off the color scale and has velocities described in Figure 25. The low-velocity zones are separated by 0.5 thick +10% high-velocity layer. (Middle column) The synthetic test recovers a separate low-velocity anomaly below 3 km depth with a positive 1 km/s velocity perturbation. (Right column) The tomographic result recovers separate low-velocity anomalies.

6.3.e. Magma Chamber vs. Fractured Pluton

A key concern in detecting the low-velocity body beneath 3 km depth is determining whether a shallow crustal magma chamber exists beneath Newberry or if it has solidified as a pluton. Previous studies debated the low-velocity body as either a magma chamber, based on the observation of low P-wave velocities (Achauer et al., 1988) or as a fractured pluton, based on the observation of only moderate P-wave attenuation (Zucca and Evans, 1988). The low-velocity body recovered in this tomography study may be small enough in magnitude to be consistent with a hot, fractured pluton. The low-velocity body is only 0.1 km/s slower than average velocity at 4 km depth and ranges in absolute velocity from 5 km/s at 3 km depth to 5.8 km/s at 6 km depth. To have a velocity of 5.6 km/s at 5 km depth in granite would require a temperature of 1500°C, according to the linear dV/dT coefficient -3.9×10^{-4} km/s°C (Christensen and Mooney, 1995). This is not appropriate considering that the solidus of granite at 100 MPa (~5 km depth) is 700-900°C, depending on H₂O content (Holtz et al., 2001). To achieve such low velocities a granitic pluton would have to be fractured, as suggested by Evans and Zucca (1988). Modeling predicts fracture formation in a pluton as it cools, although fractures may be concentrated in the edges of a pluton (Koenders and Petford, 2003). It is possible that a hot fractured pluton causes the low-velocity body below 3 km depth if the true magnitude of the low-velocity body is no greater than the recovered anomaly.

The actual magnitude of the low-velocity body may be much greater than the recovered anomaly if ray bending obscures the true velocity structure. A magma chamber is therefore very possible despite the recovered low-velocity body and moderate

attenuation region reported by Zucca and Evans (1992). The synthetic tests show that a 40% low-velocity body up to 72 km^3 in volume could be obscured in the seismic data used in this and in previous tomography studies (Figure 26). The 40% low-velocity anomaly ranges in velocity from 3 km/s at 3 km depth to 3.5 km/s at 6 km depth. A velocity of 3.0 km/s is consistent with 28 to $\sim 37\%$ silicic partial melt, and a velocity of 3.5 km/s is consistent with 23 to 32% melt depending on H_2O and CO_2 saturation. A higher H_2O and CO_2 saturation requires less melt (Chu et al., 2010, Figure 3). A mush region comprised of $30 \pm 7\%$ partial melt with a volume 72 km^3 would contain $22 \pm 5 \text{ km}^3$ of melt. While this maximum estimate may be unrealistic, much smaller volumes of melt could still produce an eruption like the recent Big Obsidian Flow, which erupted only 0.2 km^3 of rhyolitic magma (Linneman and Meyers, 1990). It is difficult to conclude that a volume of melt poses a threat, however, because melt dispersed in a crystal mush cannot erupt unless it exceeds the rheological lock up point, $\sim 50\%$ melt, 50% crystals (Vigneresse et al., 1996, Petford, 2003). Determining the concentration of melt is beyond the power of tomographic methods, due the inability to resolve low-velocity bodies. Further analysis with waveform modeling may be able to characterize and distinguish magma chamber from a pluton by modeling the timing and amplitude of the secondary arrivals.

6.4. Secondary Arrival Analysis

6.4.a. Observation of a P-wave Secondary Arrival

A secondary arrival detected by the 2008 seismic experiment provides further evidence for a low-velocity body below 3 km depth. The secondary arrival appears on the far side of the caldera, 0.5-0.7 seconds behind the first arrival at 36 km range, and becomes parallel to first arrival at 39 km range (Figure 8). The secondary arrival is

observed on the vertical component record section, but not on the radial component record section (Figure 9), indicating that it is a P-wave arrival and not an S-wave arrival. Unfortunately, no S-wave secondary arrivals were observed in the radial-component record section due to a poor signal-to-noise ratio probably caused by poor horizontal coupling of the seismometers buried in pumice and ash. The following sections focus on interpreting the P-wave secondary arrival observed in the vertical-component record section.

6.4.b. Finite-Difference Model

The observed P-wave secondary arrival may be a reflection or transmission from a variety of possible features. I test whether a small, low-velocity magma chamber beneath the caldera could cause a secondary arrival consistent with the observations. To do this I examine synthetic waveforms calculated for a test velocity model, and compare a synthetic seismic record section to the observed 2008 seismic record section. Troy Durant calculated these synthetic waveforms for the 2008 experiment geometry using E3D, an elastic finite-difference wave propagation code (see Durant and Toomey, 2009, for methods and Levander, 1988, for theory). The test model is a 1D velocity profile with an embedded low-velocity body that is similar to the synthetic inversion model in Figure 14, but with a smaller low-velocity body at 3-5 km depth (Figure 1). The low-velocity body is modeled as a 48% to 28% velocity reduction gradient, from top to bottom, simulating a stratified mush region with a pure melt sill at top and a decrease in partial melt with depth. Melt is represented by greatly decreased S-wave velocities: a 100% S-wave velocity reduction at the top (the melt sill) with a reduction gradient decreasing to

35% at the bottom (mush). The model densities are calculated from P-wave velocities by the relation $0.165 \cdot V_p + 1.852$ (Vera et al., 1990) and the model does not include attenuation structure.

6.4.c. Finite-Difference Results

The finite-difference model generates secondary arrivals from the modeled magma chamber including a delayed P-wave arrival (P_{transP}) and two converted S-wave arrivals. Troy Durant adapted the E3D output parameters to generate waveform images at even time intervals. Figure 3 presents two time frames best depicting the secondary arrivals. The resulting secondary arrivals depend not only upon the size and velocity of the magma chamber, but also upon its depth and distance from the seismic source. With the 2008 shot located 30 km from the expected magma chamber, the impending P-wave first arrival encounters the low-velocity magma chamber at an incidence angle of 80° from below. This geometry is not ideal for producing a P to S-wave conversion from the top of a magma sill and the P_{reflS} secondary arrival is relatively weak compared to the predicted P_{transP} secondary arrival. The P_{reflS} phase is produced when the P_{diffA} wavefront shears the solid-liquid interface and reflects shear energy back into the solid as P_{reflS} (Figure 3a). The predicted P_{transP} secondary arrival focuses into the low-velocity body and transmits strongly through the other side. As the P_{transP} wave exits the low-velocity, it produces P_{transS}, a transmitted P to S-wave conversion at the solid-liquid interface (Figure 3b). However, this second converted arrival is also weak compared to the P_{transP} arrival. As such it is not surprising that converted S-wave arrivals are not observed above the noise in the 2008 radial component data.

6.4.d. Synthetic Seismics

Troy Durant adapted the E3D output into seismic SEG-Y files and produced a synthetic record section. Figure 28 compares this synthetic record section to the actual record section of the 2008 profile. The vertical-component synthetic record section shows a secondary arrival starting 1.2 seconds behind the first arrival at 27 km range (Figure 27, bottom). This secondary arrival is identified as the PtransP arrival shown in the waveform images (Figure 3) by its high amplitude and distance behind the first arrival wavefront. This PtransP arrival closely matches the observed secondary arrival both in location and moveout. The correlation with the synthetic record section identifies the observed secondary arrival as a PtransP phase caused by a low-velocity body below 3 km depth. The finer details of the low-velocity body, such as whether it consists of a melt sill above a mush region, cannot be determined without further modeling

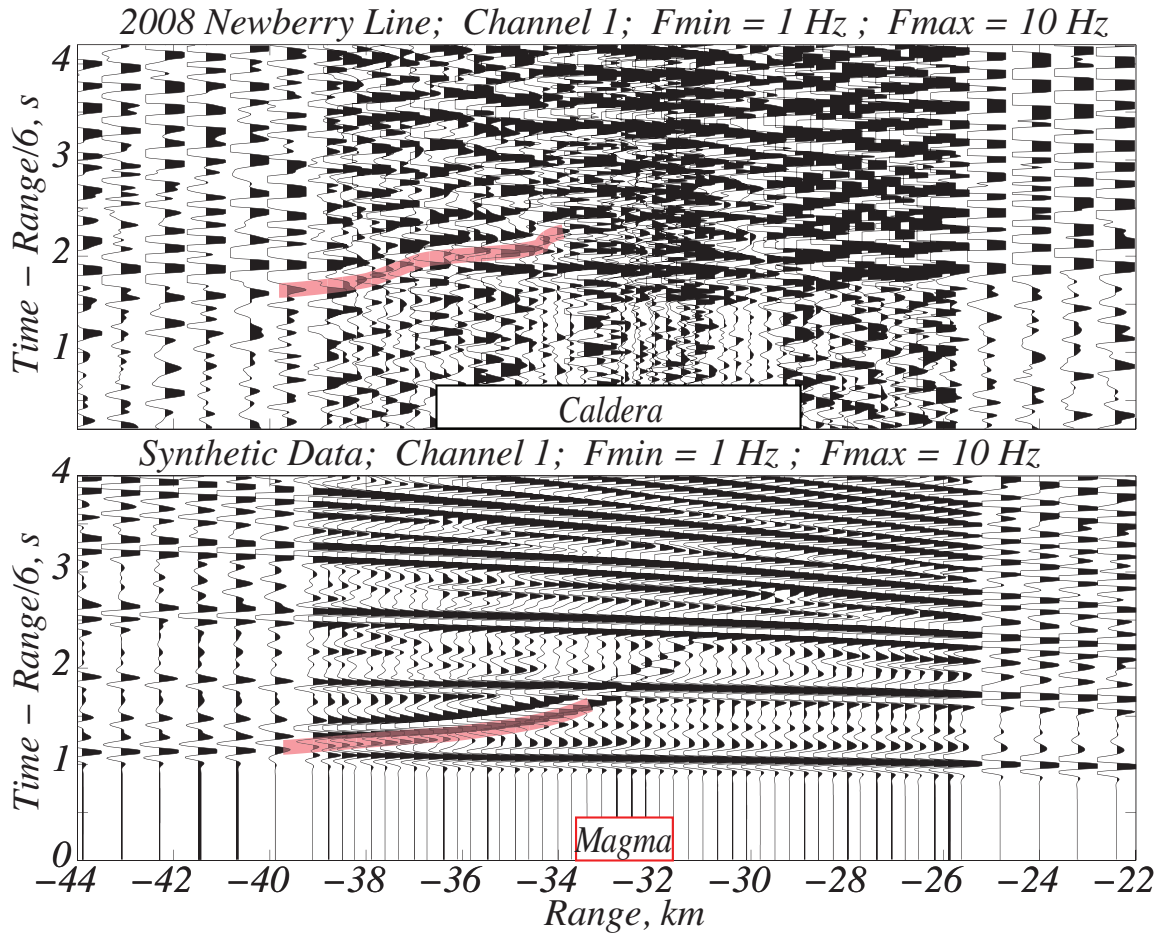


Figure 27. (Top) The central section of the 2008 vertical-component record section showing a P-wave secondary arrival (Red). The traces are Butterworth filtered from 1 to 8 Hz and range reduced at 6 km/s. The amplitude scaling is fixed and trace amplitudes are clipped at 0.8 km. (Bottom) In the central section of the synthetic seismic record section there is a P-wave secondary arrival (red) similar to the observed secondary arrival in terms of location and moveout. The same settings are applied as in the top record section. Multiples follow the first arrival at ~ 0.7 second intervals. Differences in time between the synthetic seismics and actual arrivals result from an overly fast velocity gradient in the synthetic model.

6.4.e. Future Modeling

Future work will improve upon the preliminary results presented here to identify the secondary arrival with more confidence. The preliminary waveform-modeling test produced a delayed P-wave secondary arrival from a low-velocity body that compared well with the observed secondary arrival. While the preliminary synthetic velocity model

used a simple 1D velocity gradient with a modified low-velocity body at 3-5 km depth beneath the caldera, future models could replace the 1D velocity gradient with the velocity structure from the P-wave tomography model. The velocity structure would be extracted from the 3D tomography model along the 2008 seismic profile. Having realistic structure in the finite-difference model would better reproduce waveforms observed in the 2008 record section. The synthetic first-arrival wavefront would better match the observed first-arrival wavefront, improving the comparison of the relative delay and moveout between the first-arrival and secondary-arrival. The range of the synthetic secondary arrival could also be compared to the observed secondary arrival in terms of the stations that record the arrival. Finally, an accurate background velocity model might change the nature of the synthetic secondary arrival and require a low-velocity body of different depth, size, or magnitude to produce the observed secondary arrival.

Future tests could investigate what range of structural features may cause the low-velocity body. A first test would consist of the background tomography model with no low-velocity body to confirm that a low-velocity body is necessary to cause the observed secondary arrival. Next, the model could be modified with a series of low-velocity bodies in the poorly resolved region at 3-6 km depth. The preliminary low-velocity body at 3-5 km depth would be retested in the new model with accurate background velocities. Variations of the low-velocity body would test different depths and volumes. Two particular tests would be the 35 km³, -40% low-velocity body from 3-6 km depth presented in one synthetic inversion, and a deeper low-velocity body at 4-6 km depth that would be more consistent with the observed low-velocity anomaly. In addition tests could vary the velocity reduction and density of the low-velocity body to simulate melt, mush,

or fractured rock. However, a full amplitude analysis of the observed and synthetic secondary arrivals would not be appropriate because a large range of solutions is allowed by the limited observations. Synthetic waveform analysis would give better limits on the depth, size, and magnitude of the low-velocity body than the synthetic inversion tests.

CHAPTER VII

CONCLUSIONS

This thesis investigates the upper-crustal structure of Newberry volcano. First, I present a new P-wave tomography study that images the P-wave velocity structure of the upper 6 km at Newberry and images an intrusive ring-complex, a deeper intrusive complex, and an inner-caldera fill zone. Second, the presence of a low-velocity body below 3 km depth, that is poorly resolved in the tomography study, is in agreement with several synthetic inversion tests. Third, I find that this low-velocity body is also consistent with an observed secondary arrival in the 2008 seismic profile. The conclusions depict the shallow magmatic plumbing system of Newberry volcano and suggest that a magma chamber or fractured pluton resides at 3-6 km depth.

The new P-wave tomography study obtains better resolution of the shallow volcanic structure of Newberry volcano than previous tomography studies by combining 1007 active-source travel-time data from three separate seismic experiments and inverting these with improved tomography methods, which include dense model parameterization and ray-tracing. The resulting P-wave velocity image constrains velocity structure within a region 15 km north-south, 15 km east-west, and to 4-6 km depth. The inversion images several structural features of interest. First, a ring-shaped high-velocity anomaly lies just beneath the inner set of caldera ring faults with dimensions 7 km east-west, 4 km north-south, and 1.5 km depth. I infer that the high-velocity ring is caused by either ring-dikes or cone-sheets emplaced along caldera

collapse faults. A synthetic test determines the ring-dikes or cone-sheets to be ~ 500 m thick, but cannot determine their dip. The high-velocity ring surrounds a low-velocity zone with dimensions 5.5 ± 1.5 km east-west and 4 ± 1 km north-south, where at least one collapse occurred. The boundary between caldera fill and the subsided region cannot be distinguished. A broad high-velocity zone below 2 km depth is thought to be caused by intrusive complexes and suggests that a higher concentration of intrusions were emplaced east and west of the caldera due to the presence of fault zones north and south of the caldera.

The tomography study detects a low-velocity body at 3-6 km depth below Newberry's caldera although it is poorly resolved. Potential travel times associated with this low-velocity body were not picked due to weak signal. I infer that the signal is lost to the spreading of deflected wave energy around the low-velocity body. I estimate that a low-velocity body up to 70 km^3 in volume is consistent with the tomography results by modeling a 40% low-velocity body in synthetic travel-time inversions. Synthetic inversions also determine that the low-velocity body at 3-6 km depth is not related to shallow low-velocities associated with caldera fill. I conclude that the low-velocity body could indicate a mush region containing up to $30 \pm 7\%$ partial melt with a maximum volume of 72 km^3 , or at the minimum a hot, fractured pluton.

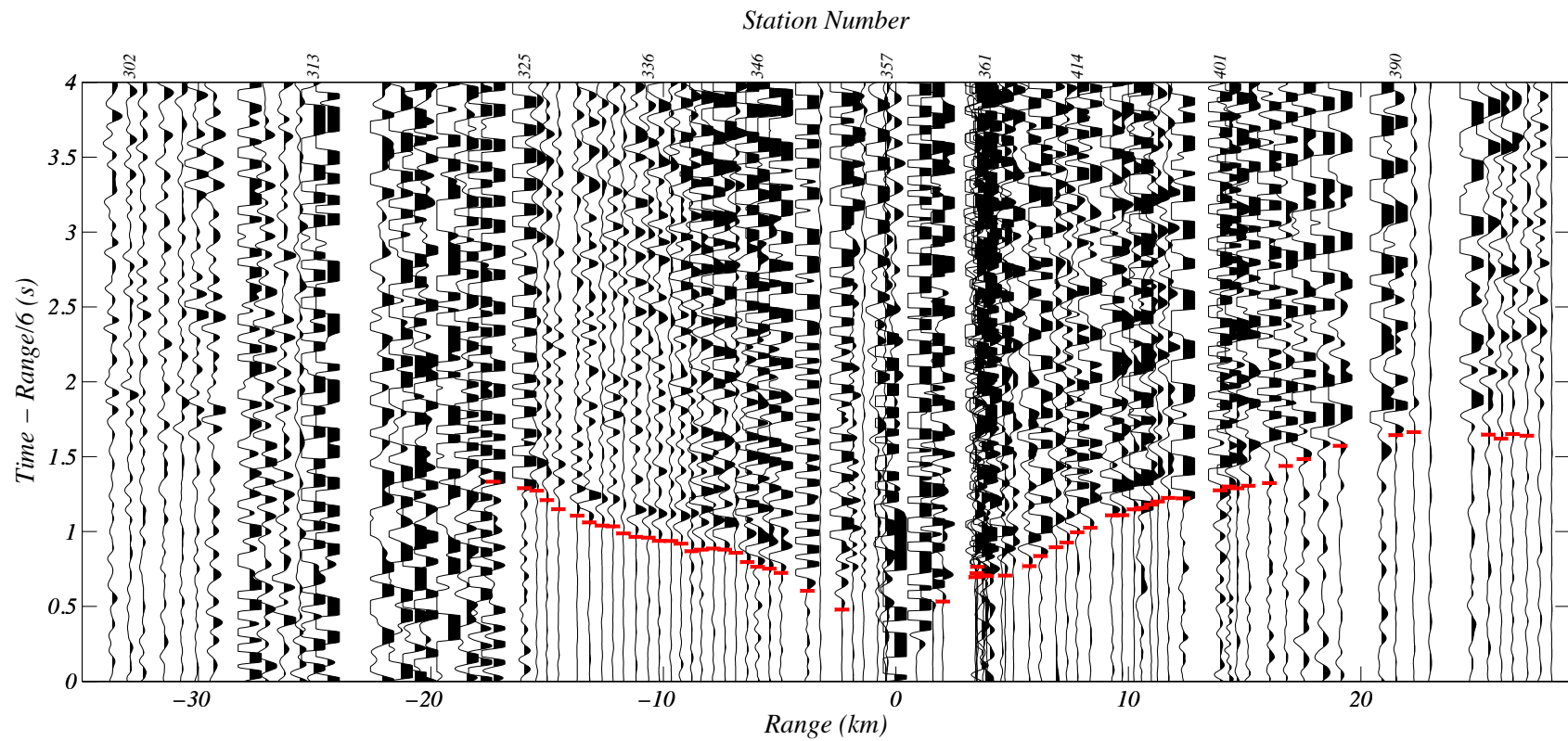
Further evidence for a low-velocity body is provided by a secondary arrival observed in the 2008 seismic profile. The 2008 seismic experiment allows identification of secondary arrivals because a coherent record section was produced by having dense, even, instrument spacing. Preliminary finite-difference modeling replicates this secondary arrival from a synthetic model containing a low-velocity body beneath the

caldera. Analysis of the finite-difference waveforms identifies the secondary arrival as a delayed P-wave arrival transmitted through the low-velocity body. These results are consistent with a magma chamber. I conclude that the secondary arrival arises from the same low-velocity body detected by the tomography study, and that the low velocity body is either a magma chamber or a hot, fractured pluton.

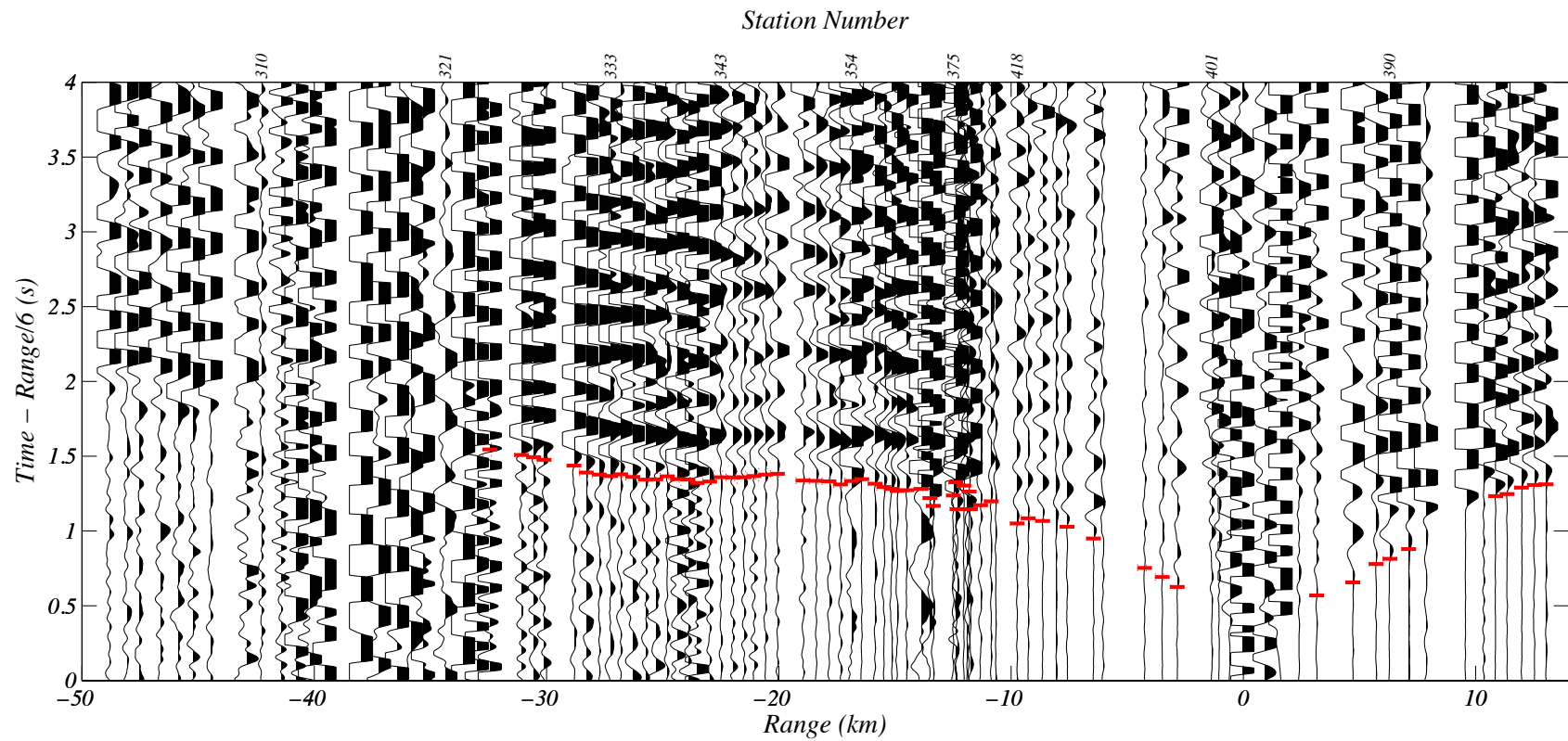
APPENDIX A

P-WAVE TRAVEL-TIME DATA

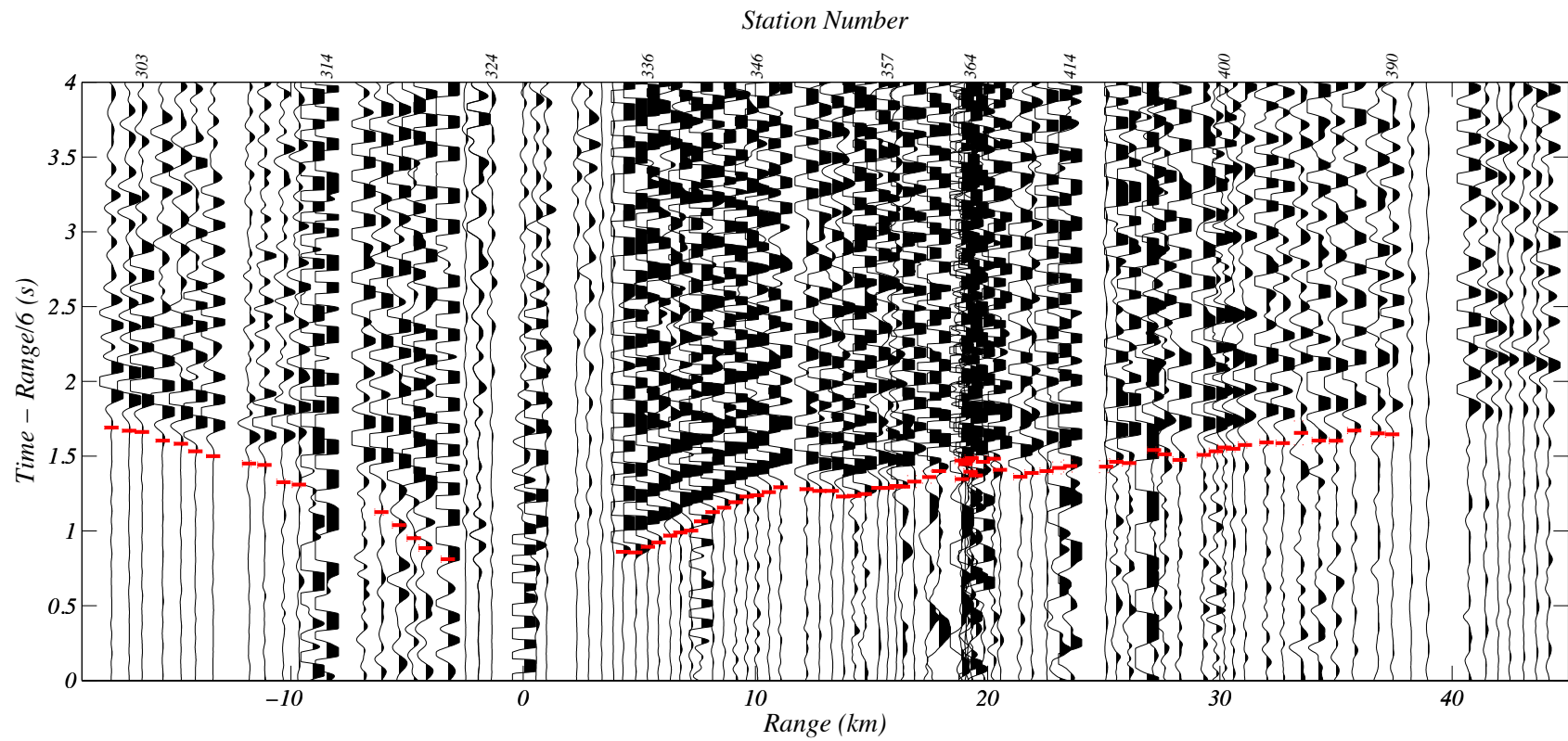
P-wave travel times are picked on seismic traces at the beginning of first-arriving seismic impulse (on the first phase). To identify the first arrivals the seismic traces are plotted in record sections with a trace for each station sorted by station number or range for a single event. Record sections for the refraction line studies (1983 and 2008) are sorted by range with negative ranges west of the event and positive ranges east of the event (the event is at zero range). Record sections for the 3D tomography array (1984) are plotted by station number because traces would overlap in a range plot. Record sections are range reduced by 6 km/s to align the first arrivals near horizontally across traces. Filters remove noise and sometimes appear to offset the first phase from the travel-time picks. 68% confidence intervals are estimated for the travel-time picks and are shown as dotted lines above and below the picks when large enough.



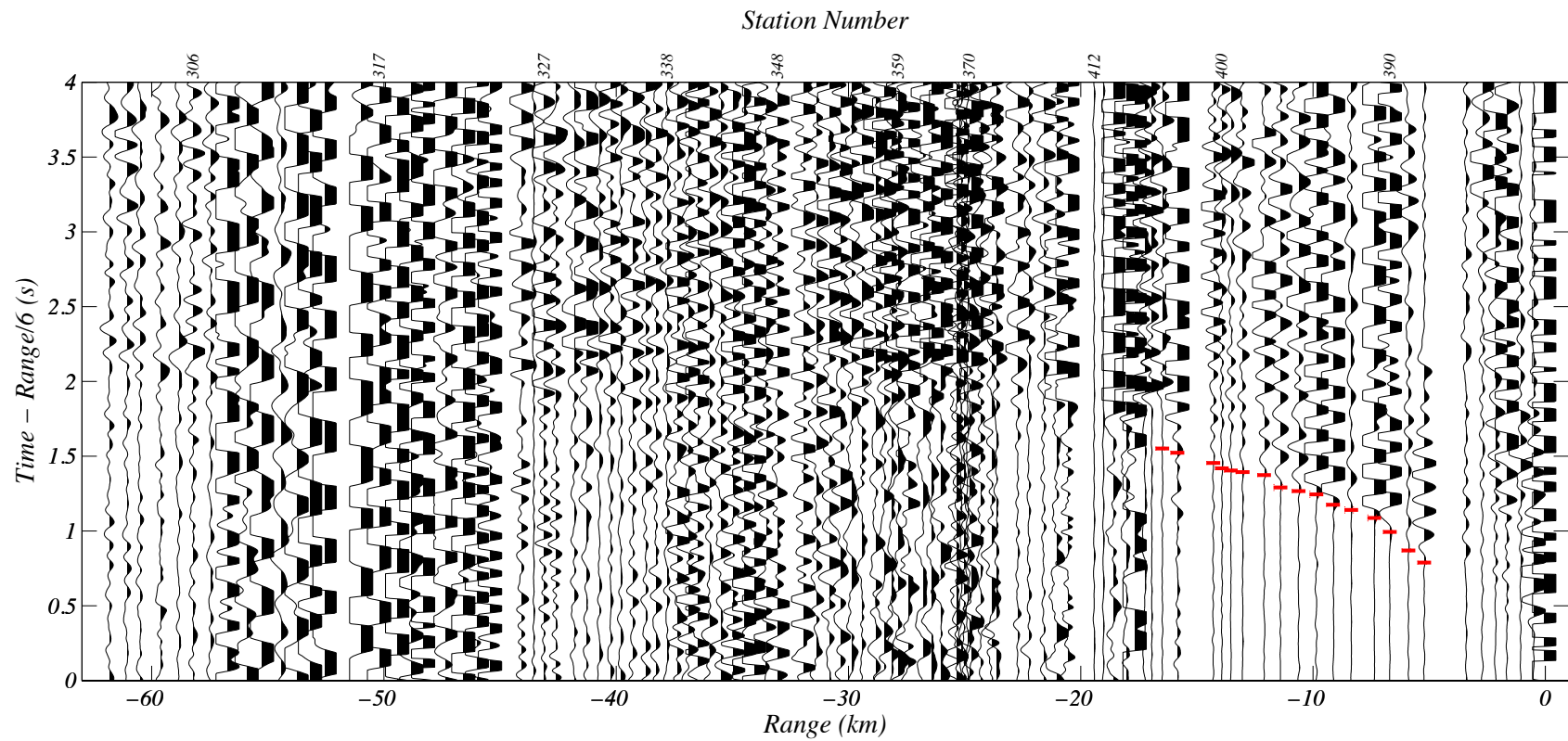
Shot 4, 1983. Traces are plotted by range and time aligned with a 6 km/s range reduction. A Butterworth filter is applied from 1 to 8 Hz. Amplitude scaling is fixed and clipped at 0.5 km. Red bars show first-arrival picks.



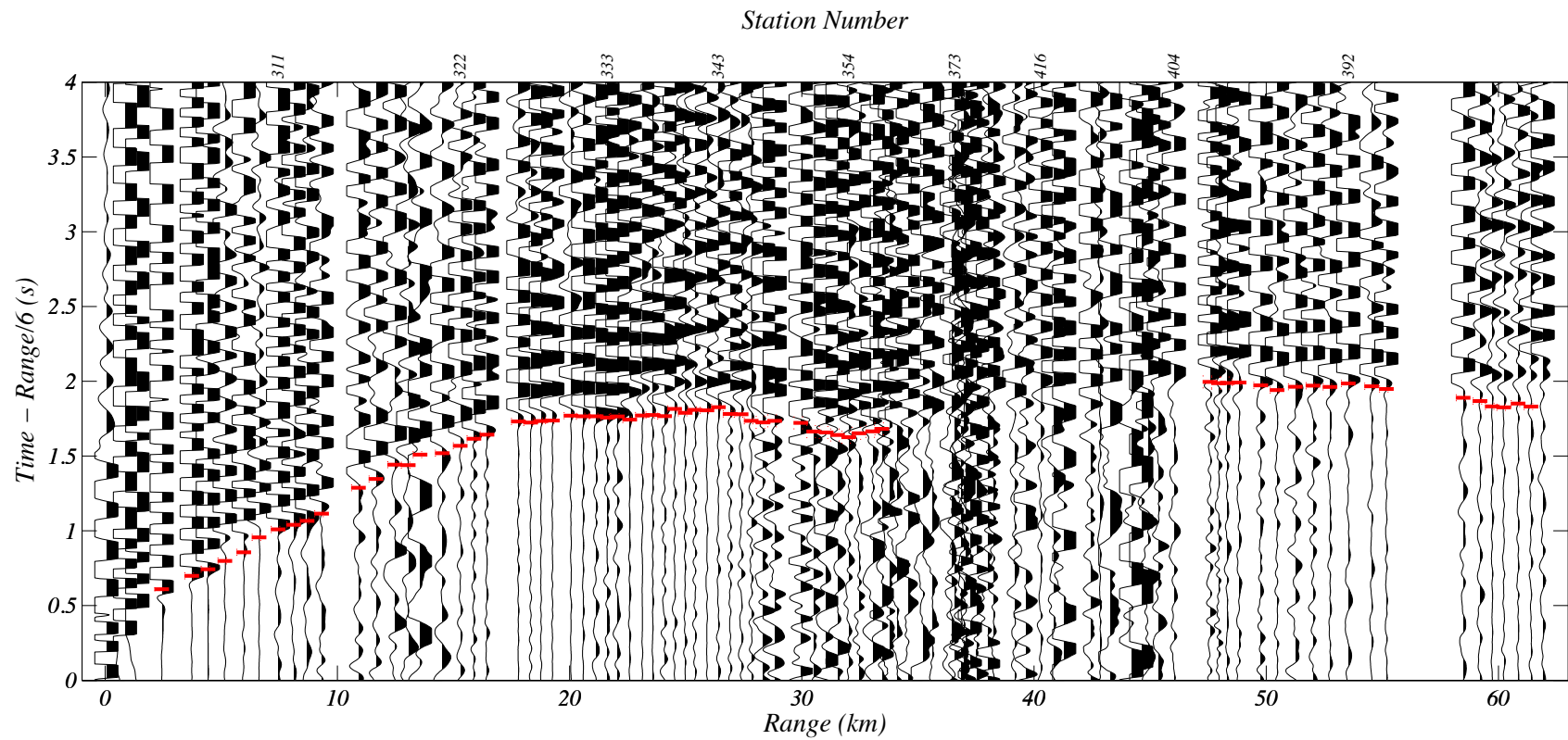
Shot 6, 1983. Traces are plotted by range and time aligned with a 6 km/s range reduction. A Butterworth filter is applied from 1 to 8 Hz. Amplitude scaling is fixed and clipped at 0.5 km. Red bars show first-arrival picks.



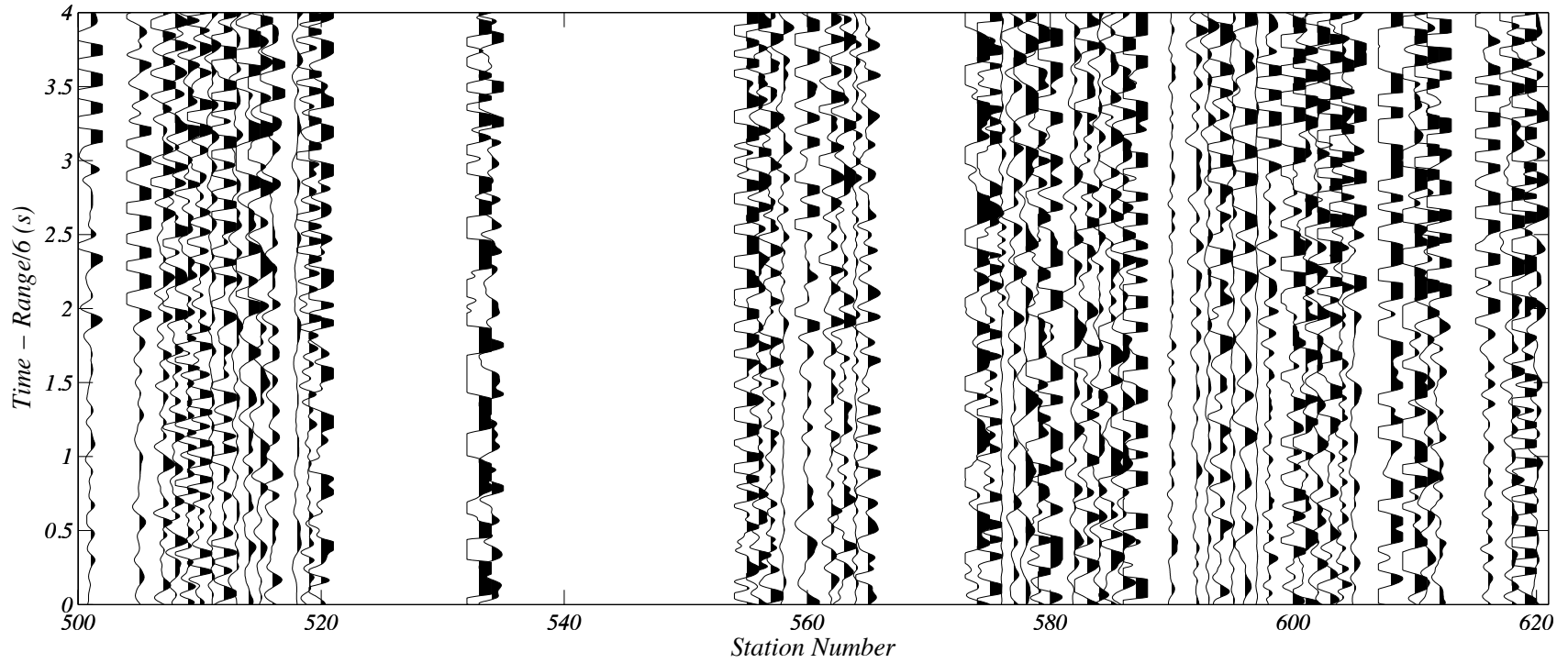
Shot 7, 1983. Traces are plotted by range and time aligned with a 6 km/s range reduction. A Butterworth filter is applied from 1 to 8 Hz. Amplitude scaling is fixed and clipped at 0.5 km. Red bars show first-arrival picks.



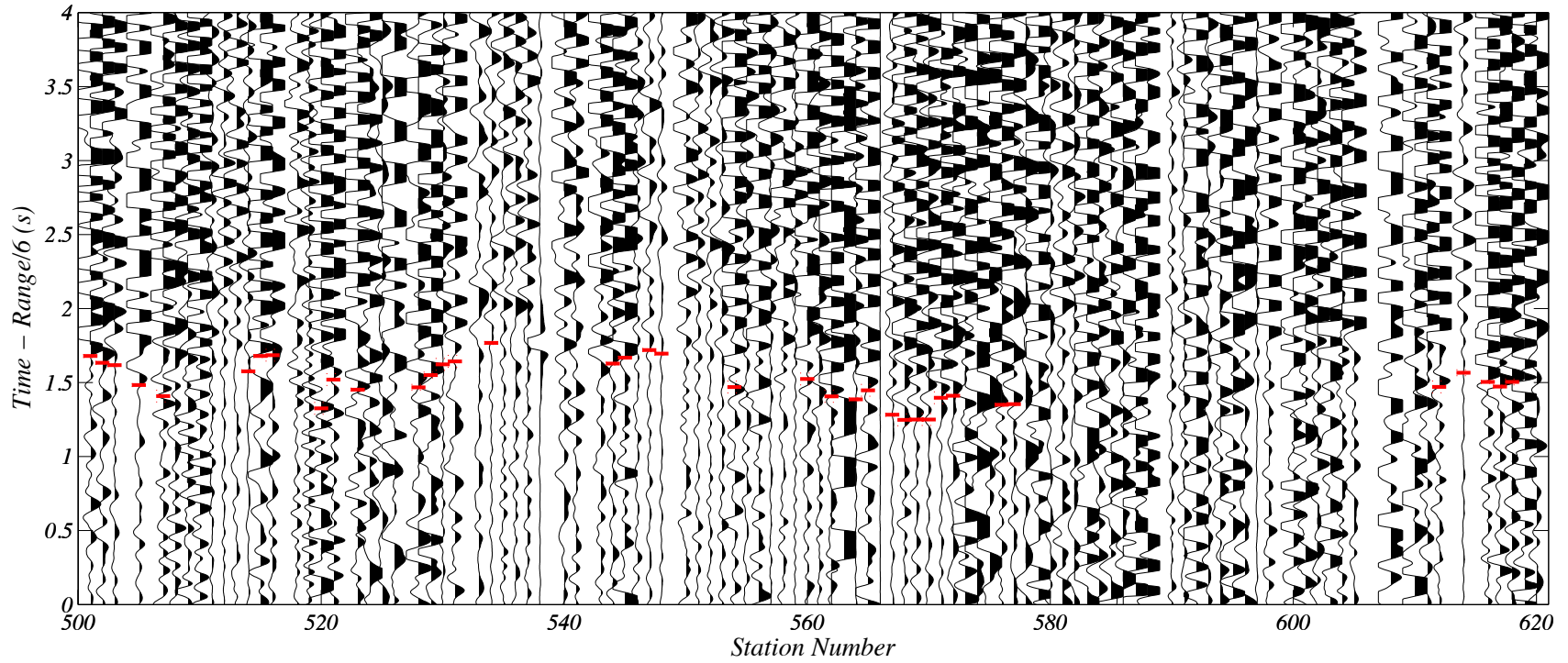
Shot 8, 1983. Traces are plotted by range and time aligned with a 6 km/s range reduction. A Butterworth filter is applied from 1 to 8 Hz. Amplitude scaling is fixed and clipped at 0.5 km. Red bars show first-arrival picks.



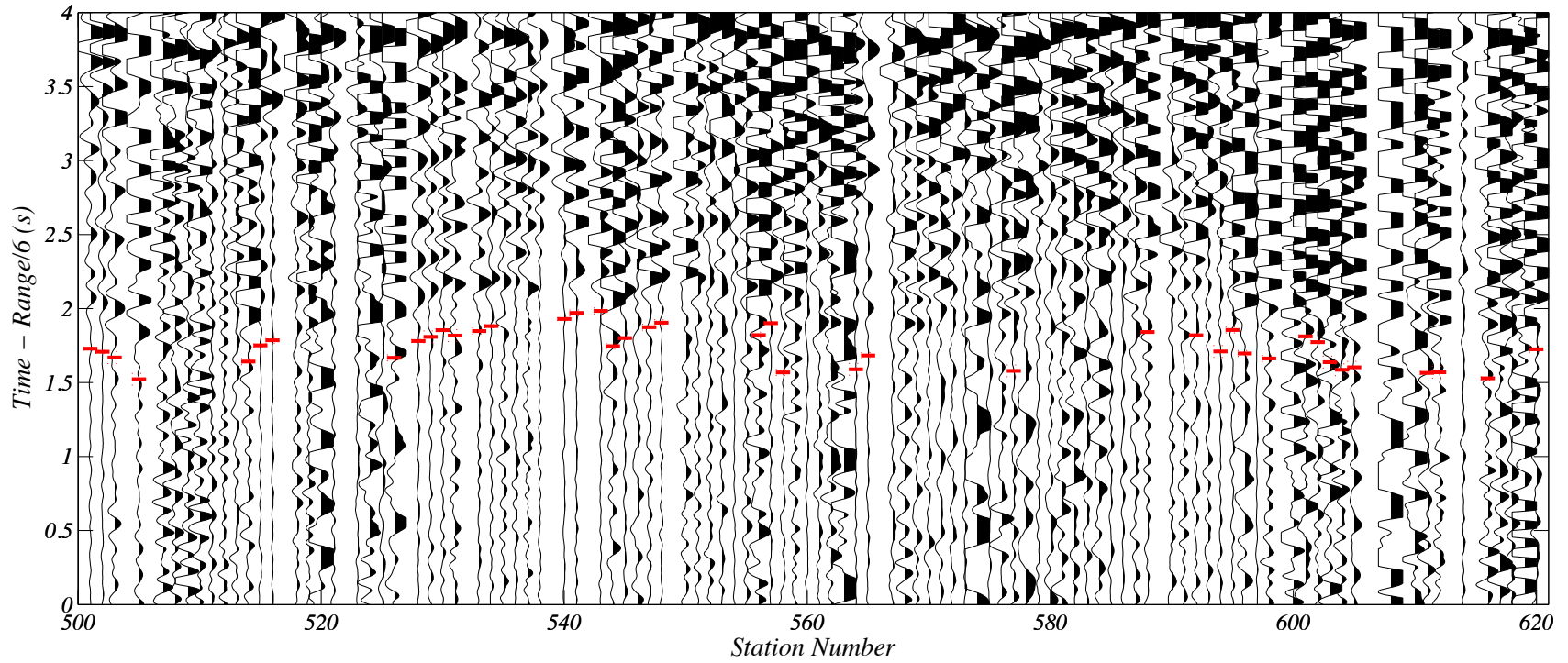
Shot 10, 1983. Traces are plotted by range and time aligned with a 6 km/s range reduction. A Butterworth filter is applied from 1 to 8 Hz. Amplitude scaling is fixed and clipped at 0.5 km. Red bars show first-arrival picks.



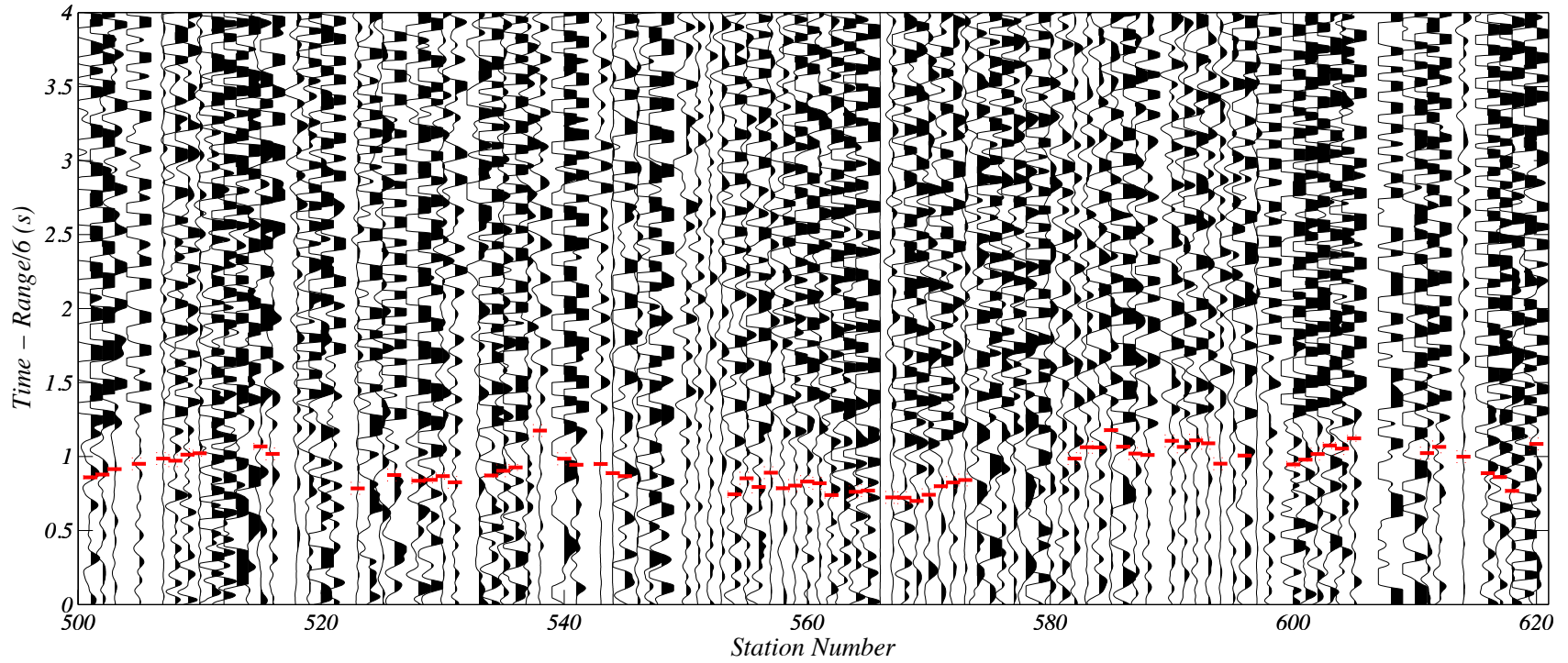
Shot 11, 1984. Traces are plotted by station number and time aligned with a 6 km/s range reduction. Traces that could not be identified to a station were removed. A Butterworth filter is applied from 1-5 Hz. No first-arrival picks were made.



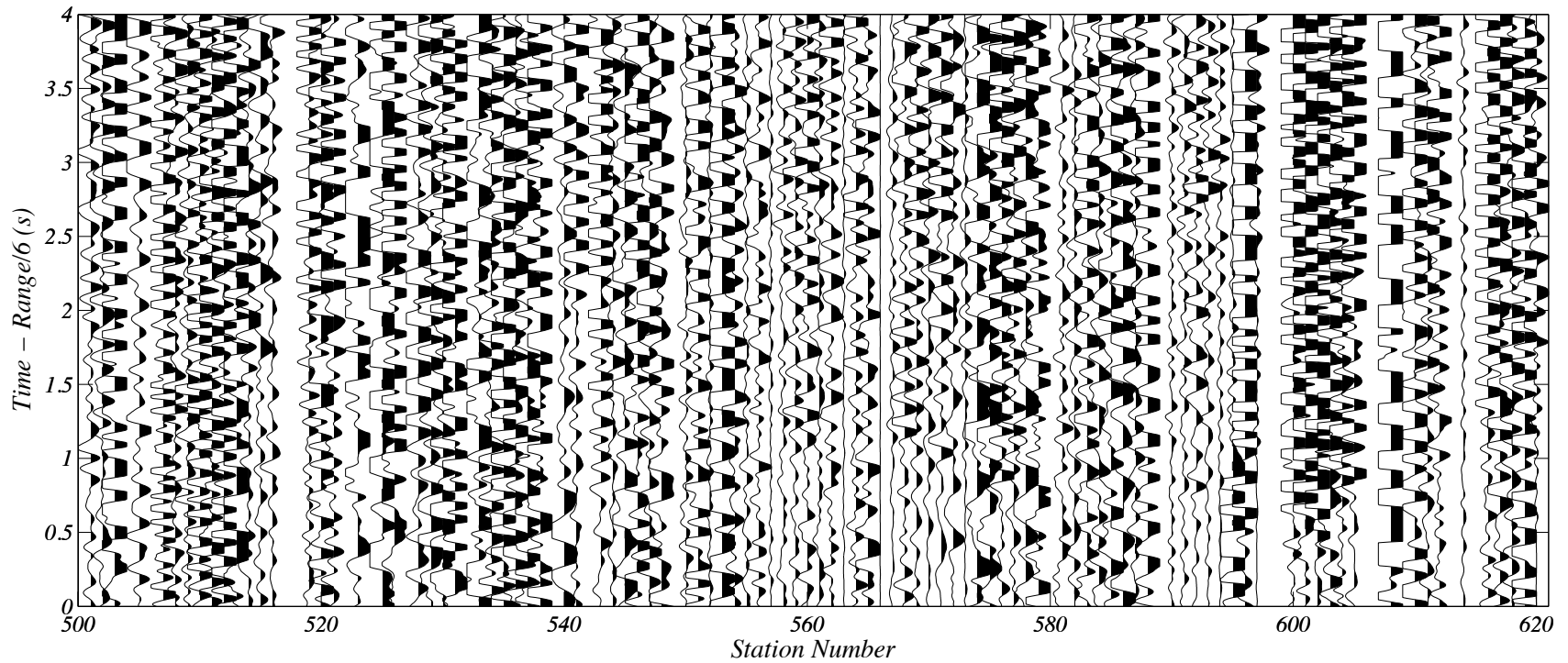
Shot 12, 1984. Traces are plotted by station number and time aligned with a 6 km/s range reduction. A Butterworth filter is applied from 1-5 Hz. Red bars show first-arrival picks.



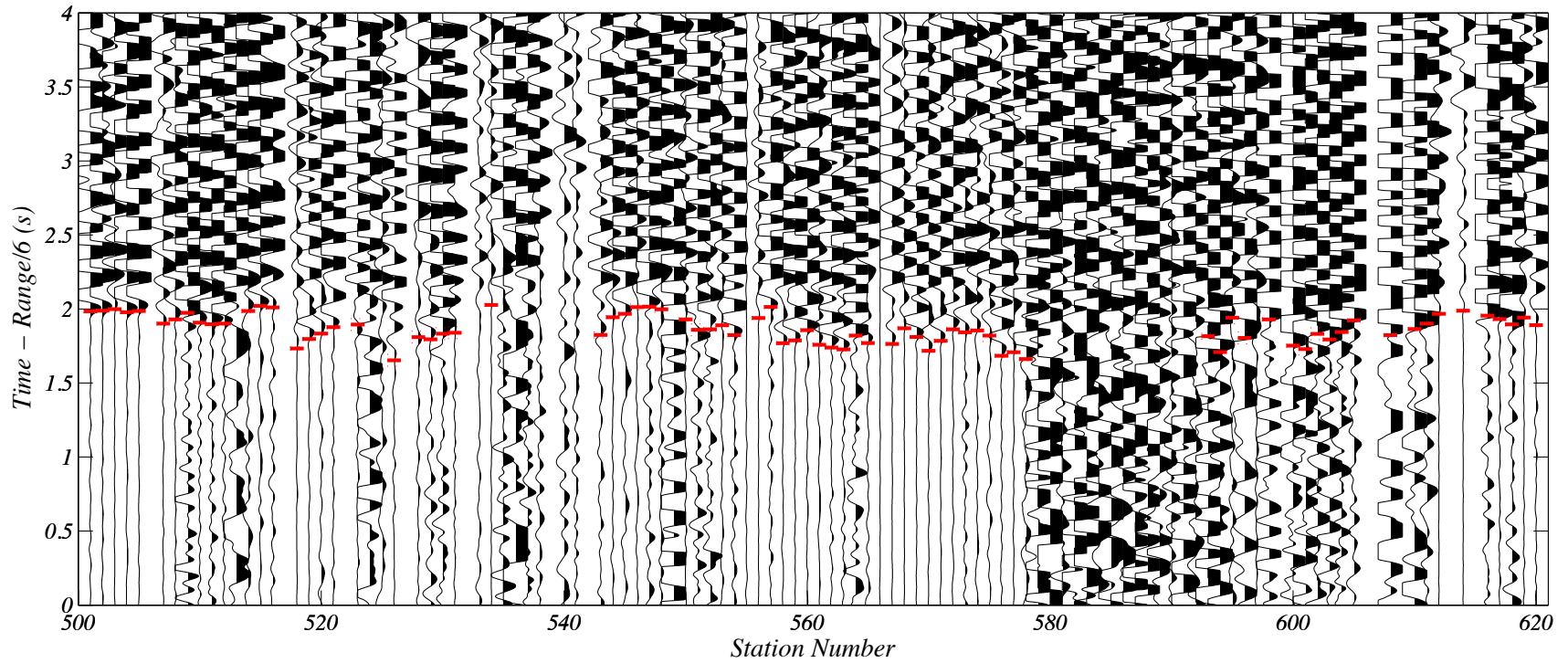
Shot 13, 1984. Traces are plotted by station number and time aligned with a 6 km/s range reduction. A Butterworth filter is applied from 1-5 Hz. Red bars show first-arrival picks.



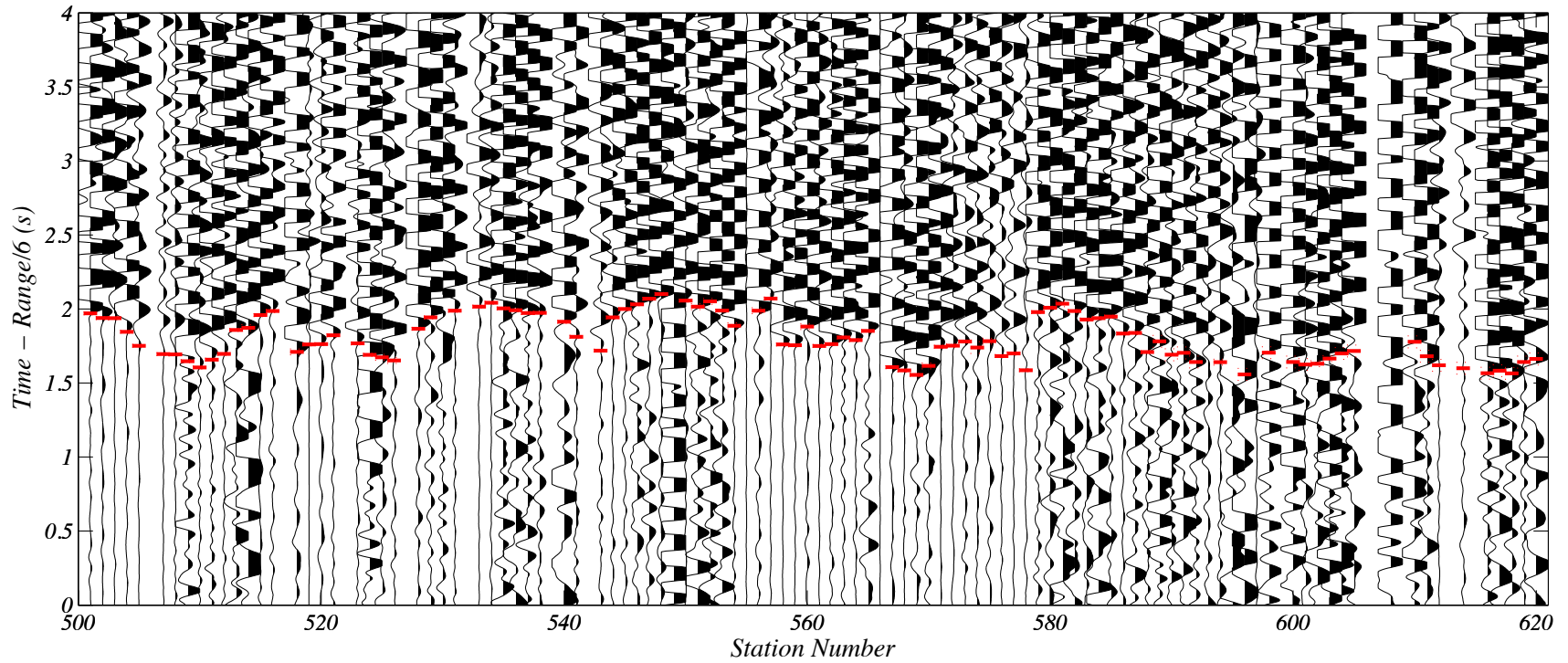
Shot 14, 1984. Traces are plotted by station number and time aligned with a 6 km/s range reduction. A Butterworth filter is applied from 1-5 Hz. Red bars show first-arrival picks.



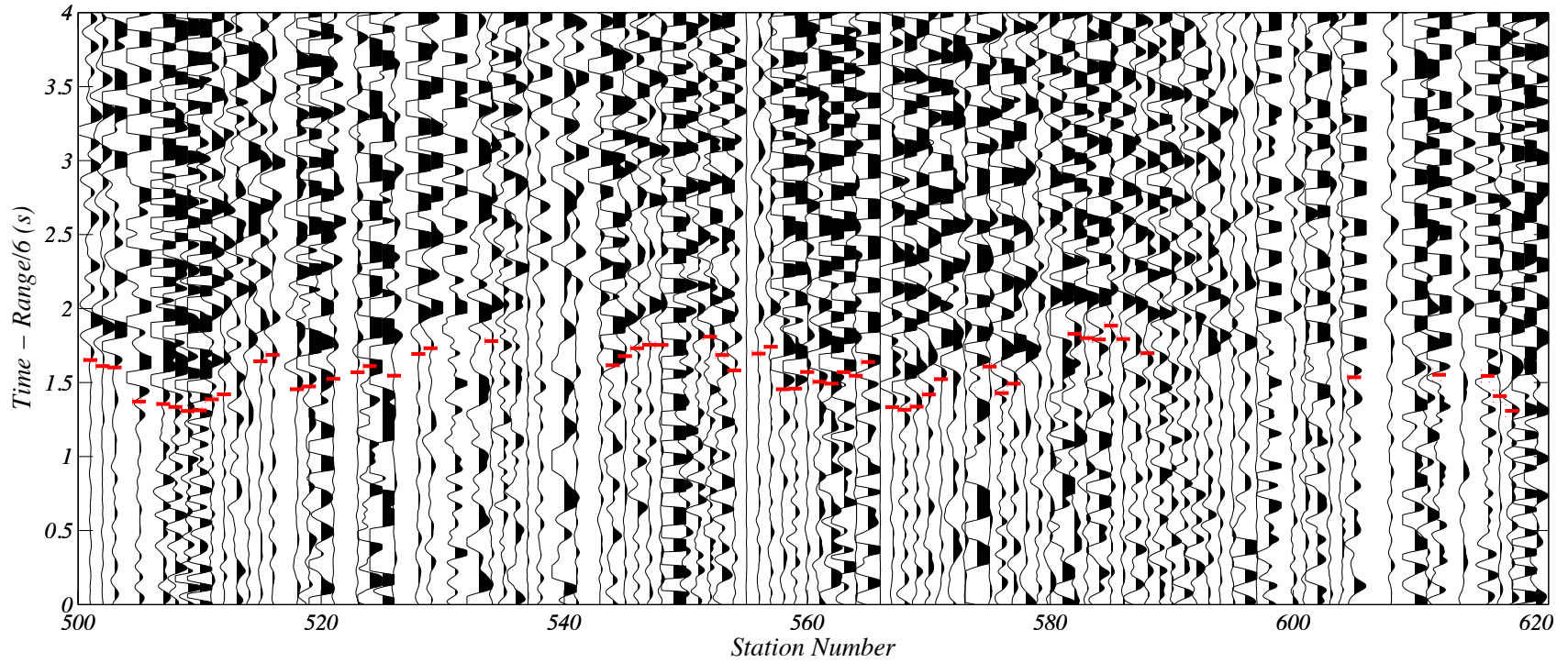
Shot 15, 1984. Traces are plotted by station number and time aligned with a 6 km/s range reduction. A Butterworth filter is applied from 1-5 Hz. No first-arrival picks were made.



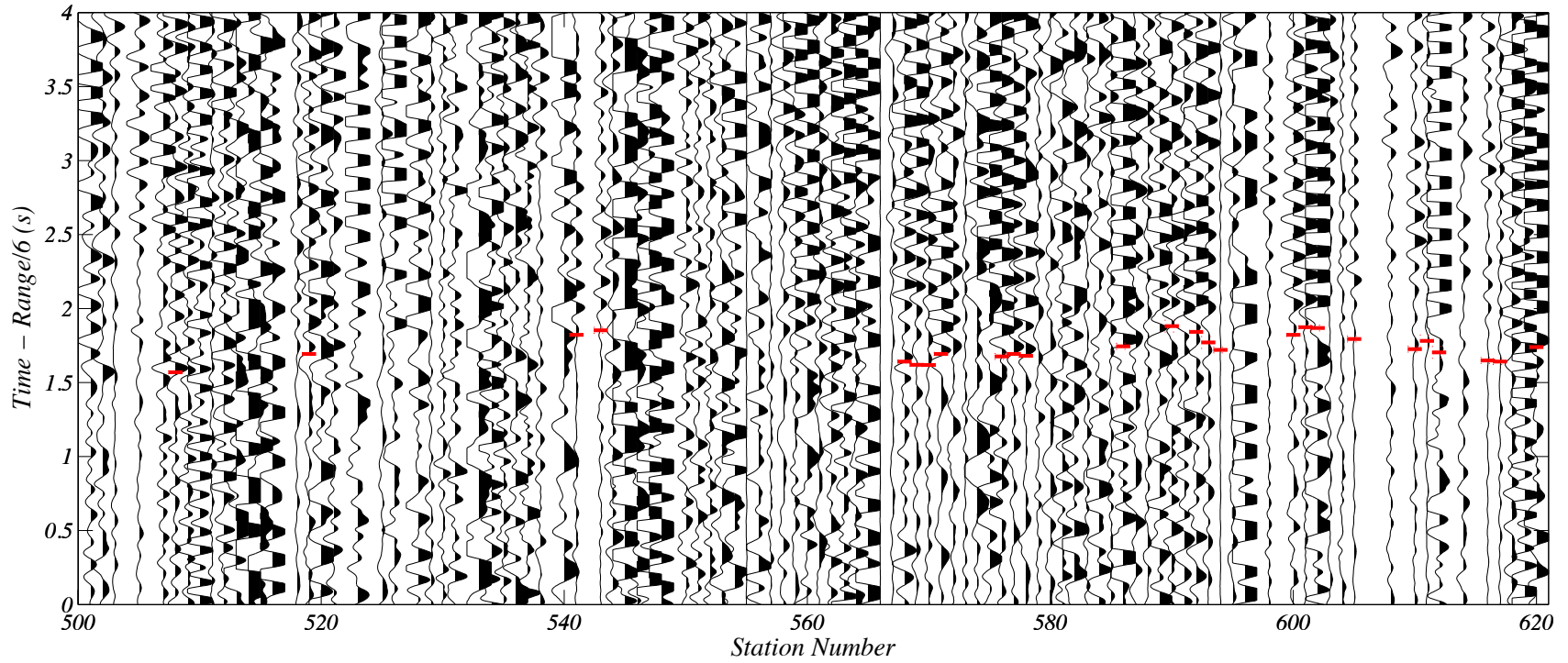
Shot 16, 1984. Traces are plotted by station number and time aligned with a 6 km/s range reduction. A Butterworth filter is applied from 1-5 Hz. Red bars show first-arrival picks.



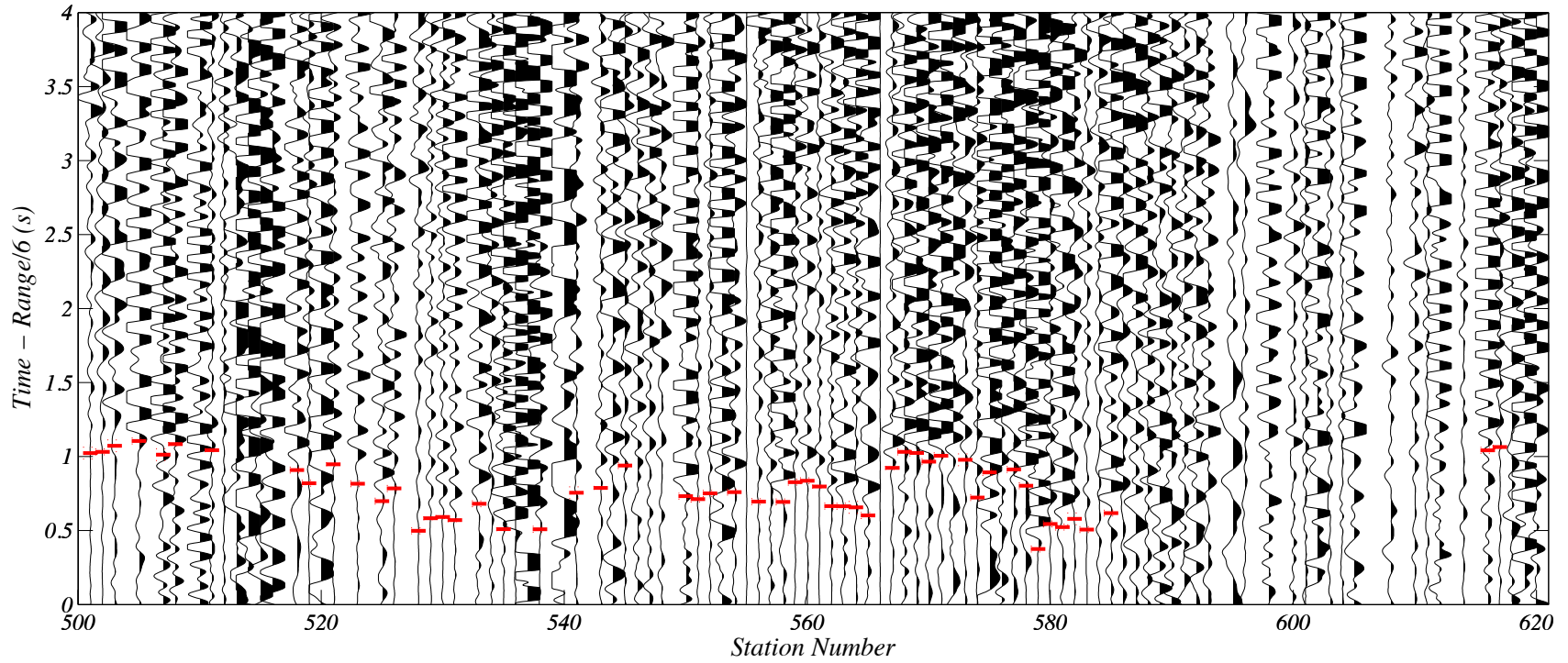
Shot 17, 1984. Traces are plotted by station number and time aligned with a 6 km/s range reduction. A Butterworth filter is applied from 1-5 Hz. Red bars show first-arrival picks.



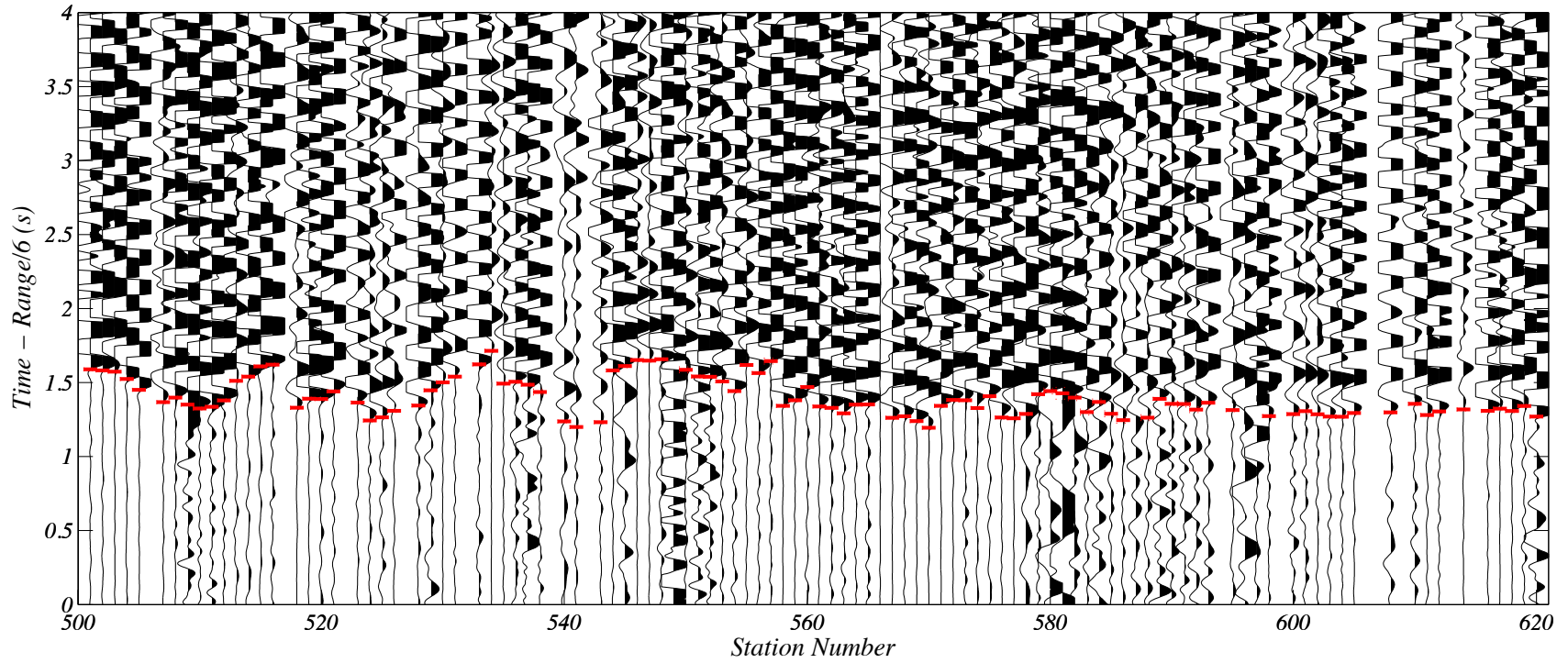
Shot 18, 1984. Traces are plotted by station number and time aligned with a 6 km/s range reduction. A Butterworth filter is applied from 1-5 Hz. Red bars show first-arrival picks.



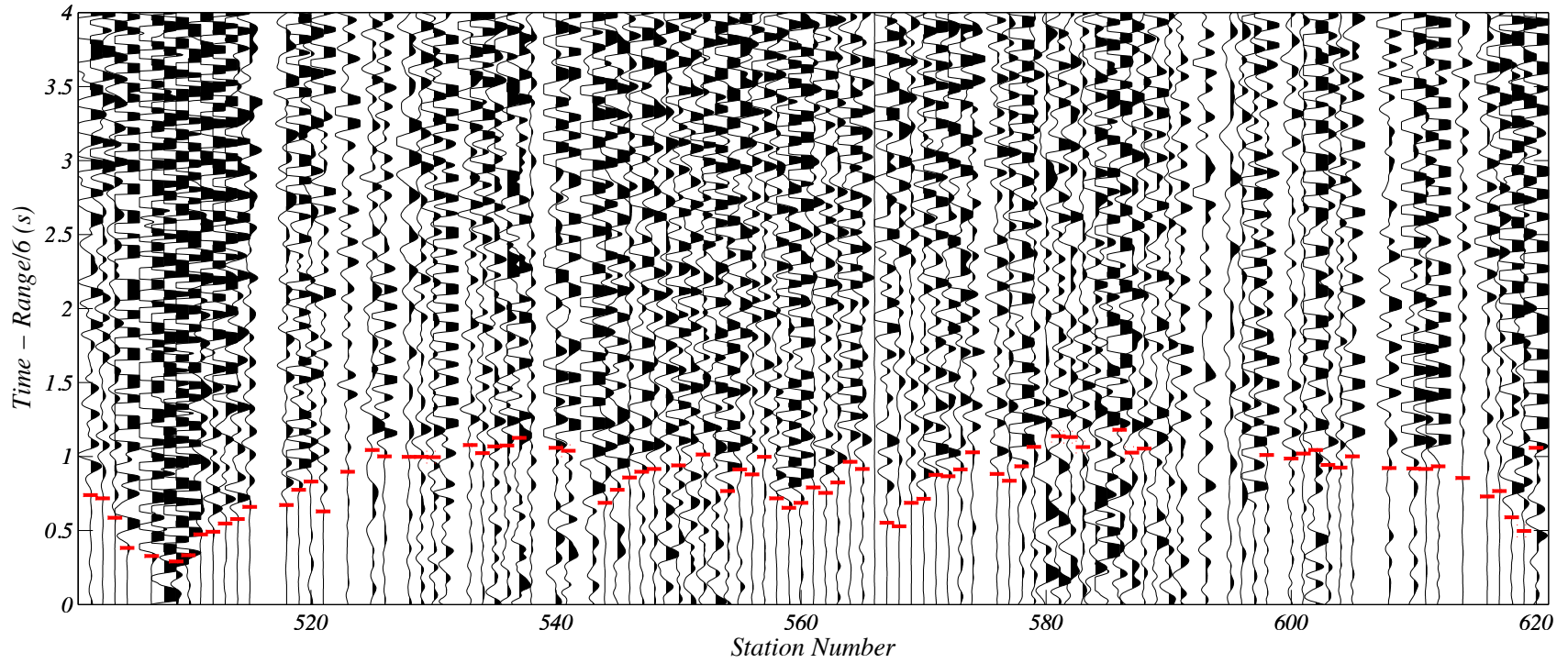
Shot 19, 1984. Traces are plotted by station number and time aligned with a 6 km/s range reduction. A Butterworth filter is applied from 1-5 Hz. Red bars show first-arrival picks.



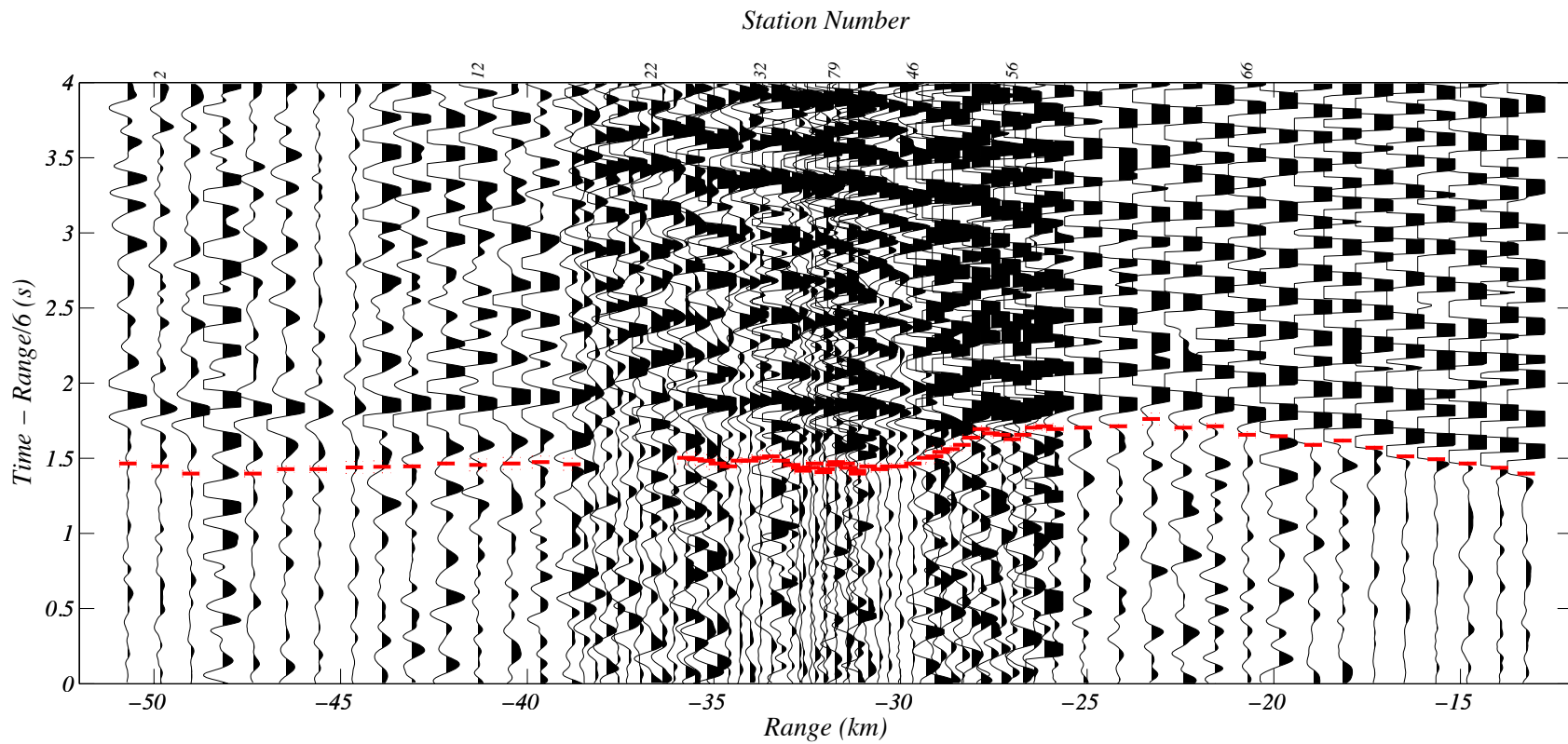
Shot 20, 1984. Traces are plotted by station number and time aligned with a 6 km/s range reduction. A Butterworth filter is applied from 1-5 Hz. Red bars show first-arrival picks.



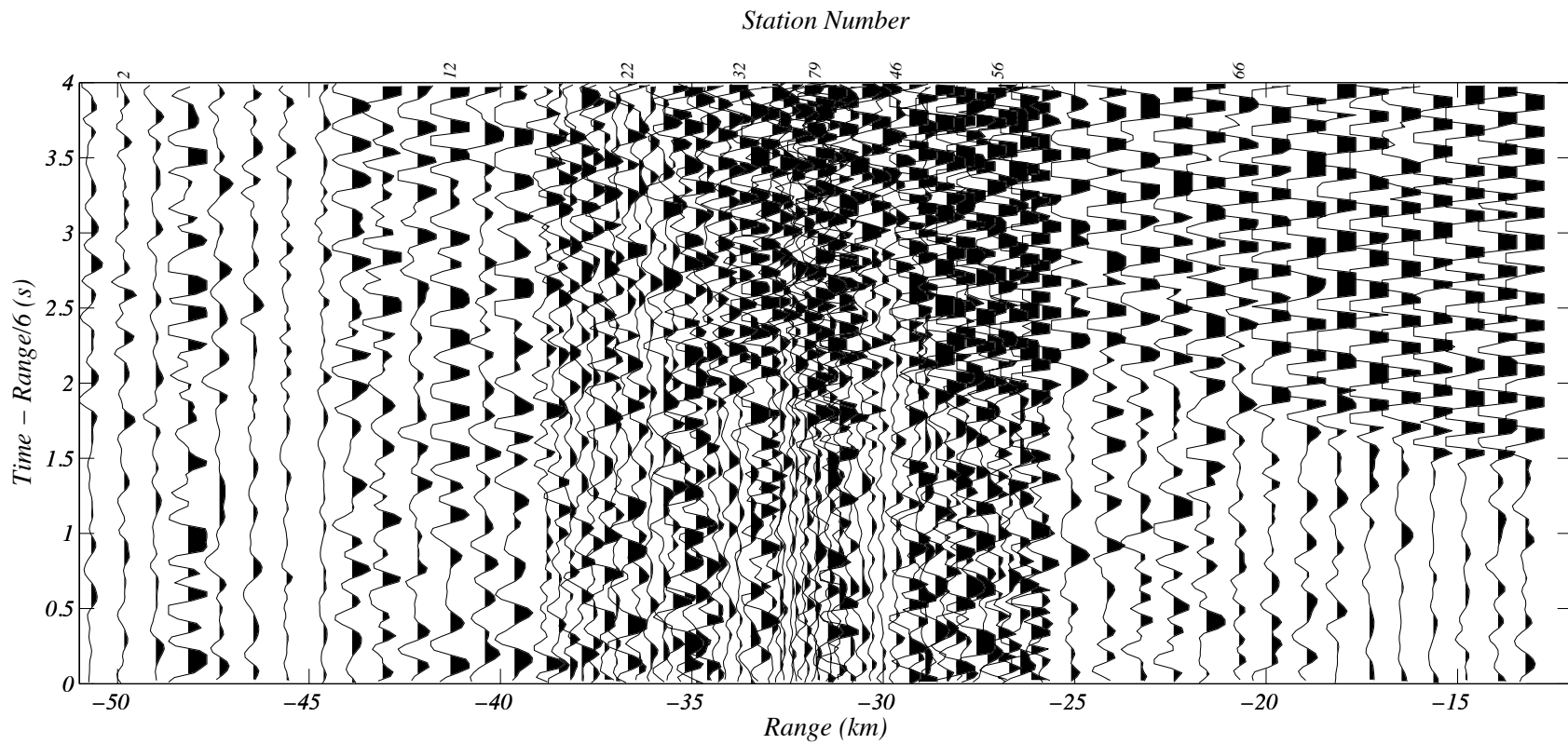
Shot 21, 1984. Traces are plotted by station number and time aligned with a 6 km/s range reduction. A Butterworth filter is applied from 1-5 Hz. Red bars show first-arrival picks.



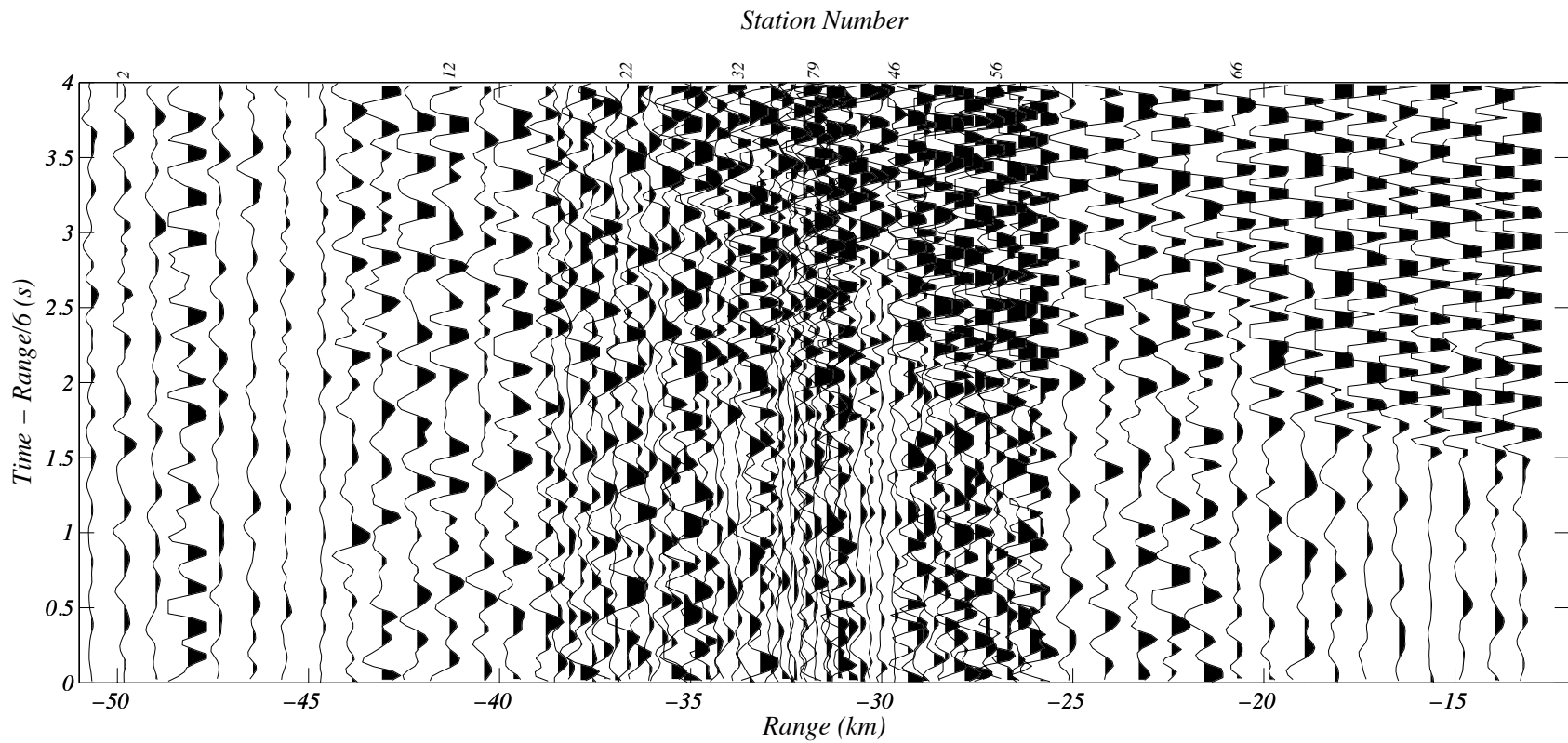
Shot 22, 1984. Traces are plotted by station number and time aligned with a 6 km/s range reduction. A Butterworth filter is applied from 1-5 Hz. Red bars show first-arrival picks.



Shot 9011, 2008, Vertical Component. Traces are plotted by range and time aligned with a 6 km/s range reduction. A Butterworth filter is applied from 1 to 5 Hz. Amplitude scaling is fixed and clipped at 0.5 km. Red bars show first-arrival picks.



Shot 9011, 2008, Radial Component. Traces are plotted by range and time aligned with a 6 km/s range reduction. A Butterworth filter is applied from 1 to 5 Hz. Amplitude scaling is fixed and clipped at 0.5 km. No first-arrival picks are made.

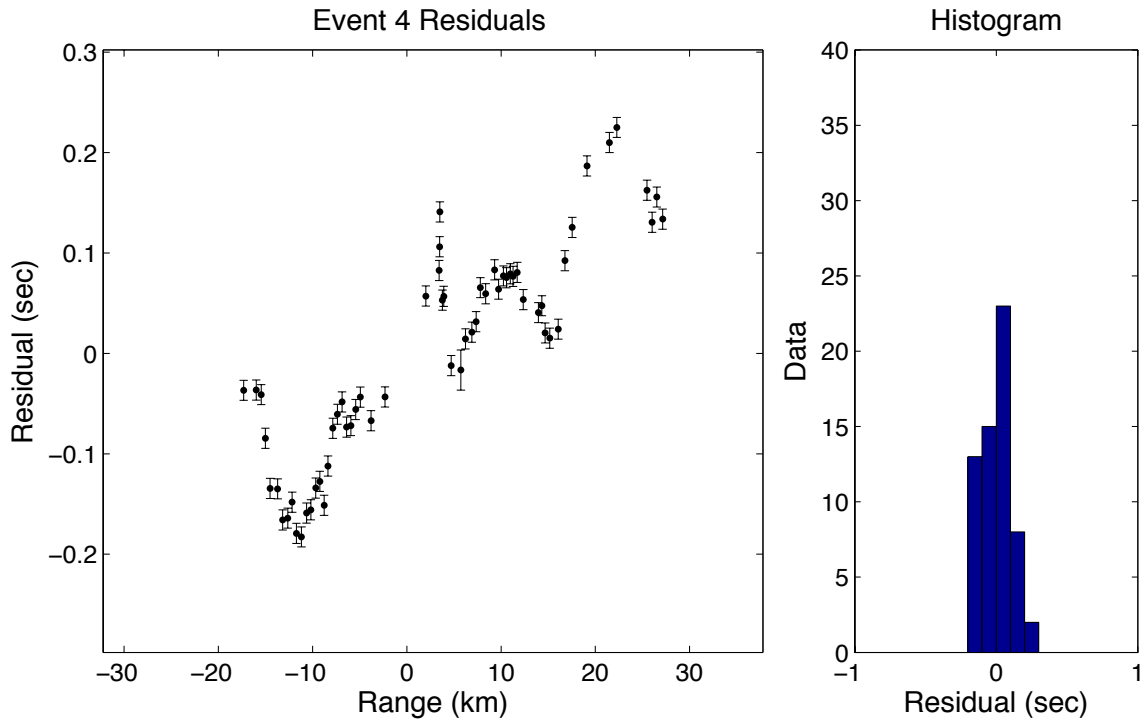


Shot 9011, 2008, Transverse Component. Traces are plotted by range and time aligned with a 6 km/s range reduction. A Butterworth filter is applied from 1 to 5 Hz. Amplitude scaling is fixed and clipped at 0.5 km. No first-arrival picks are made.

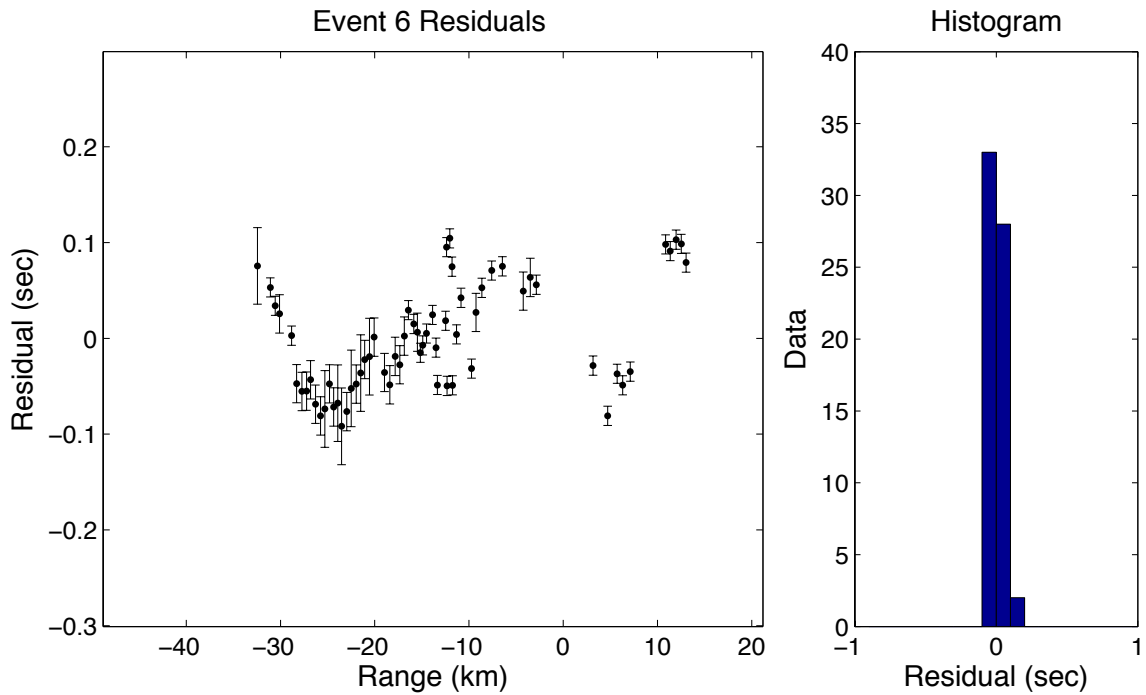
APPENDIX B

P-WAVE TRAVEL-TIME RESIDUALS

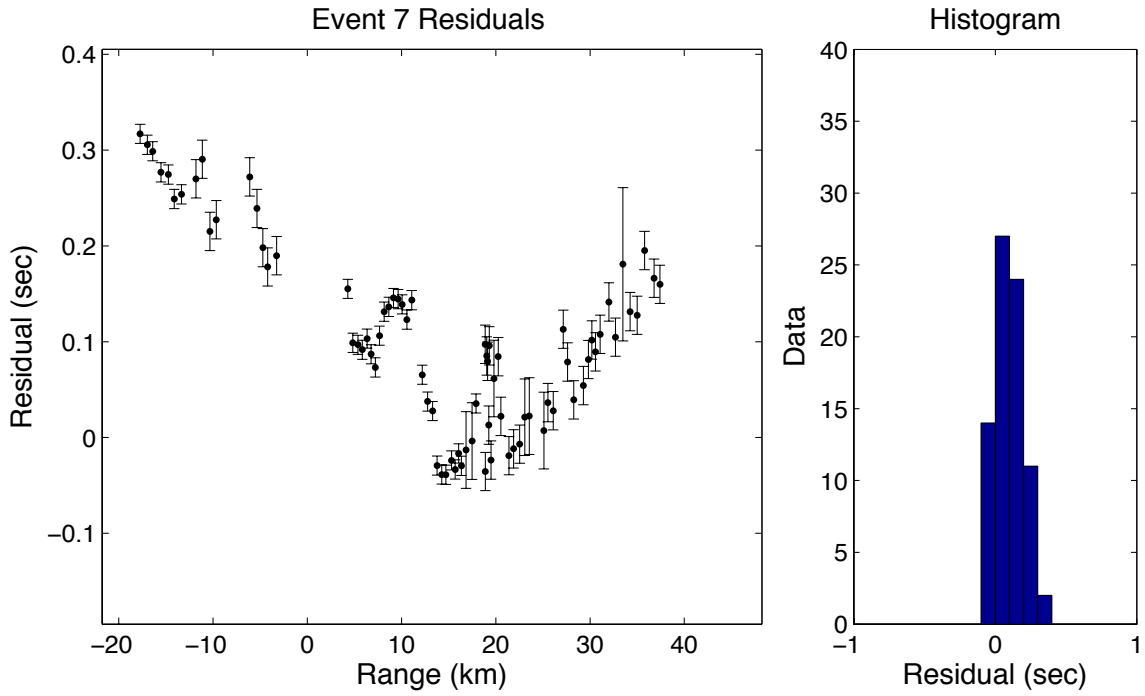
Travel-time residuals are the difference between the observed arrival time and the predicted arrival time calculated by ray tracing through a velocity model (residual = observed – predicted). A positive travel-time residual indicates that the predicted travel time is earlier than the observed travel time and that the velocity model is slower than the actual structure integrated along the region sampled by an associated ray-path. A negative travel-time residual indicates the opposite. In this appendix, travel-time residuals are plotted by station range or location for a single event. Residuals from the refraction line studies (1983 and 2008) are plotted as residual vs. range while those from the 3D tomography array (1984) are plotted in map-view and color scaled because they would overlap in a range plot. Residual histograms ideally show Gaussian distributions with no outliers. Some histograms show bimodal distributions but were accepted after confirming that the travel-time picks didn't follow two different phases.



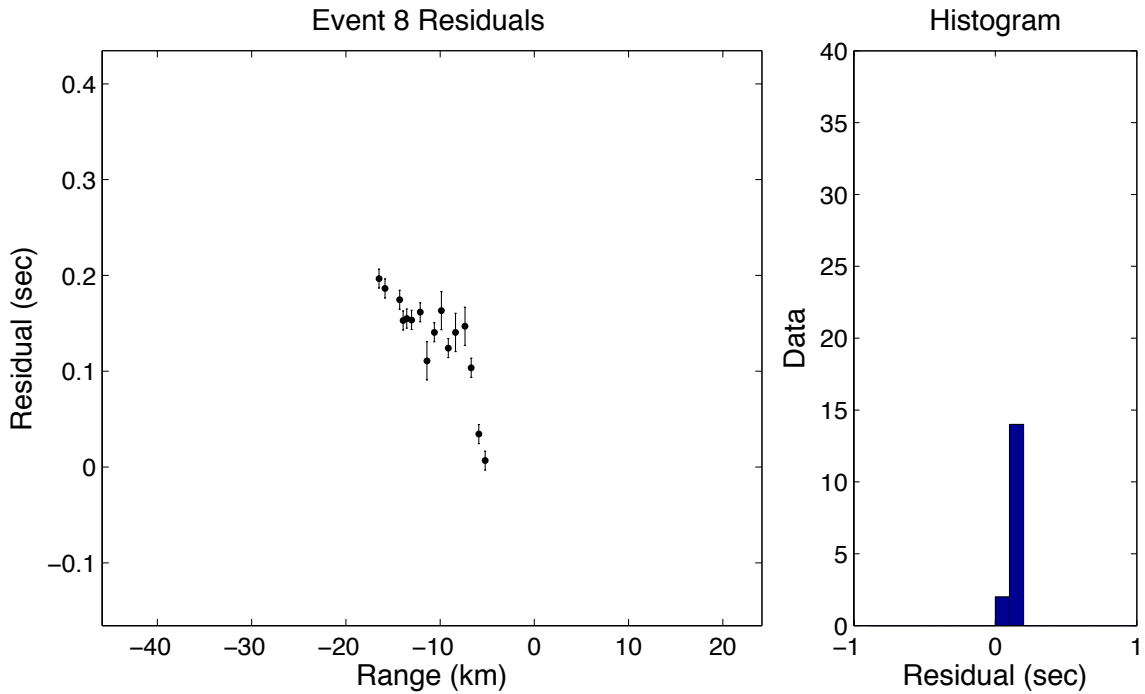
Event 4, 1983. Residuals are plotted by station range from the event. Error bars show 68% confidence intervals.



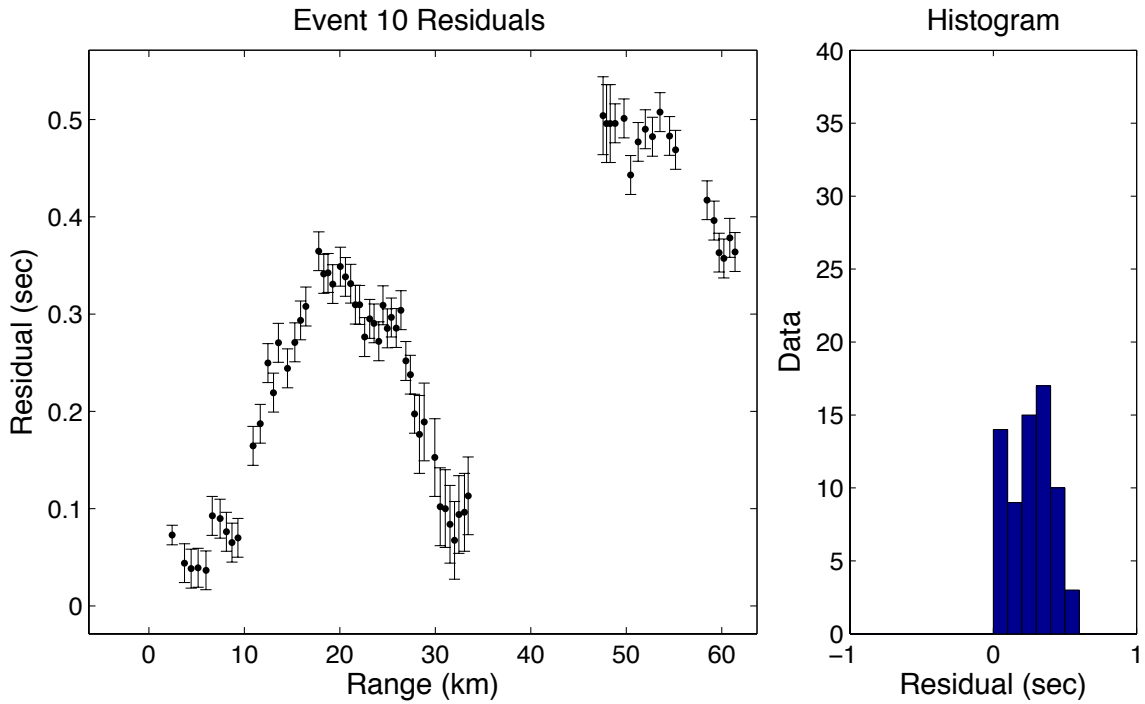
Event 6, 1983. Residuals are plotted by station range from the event. Error bars show 68% confidence intervals.



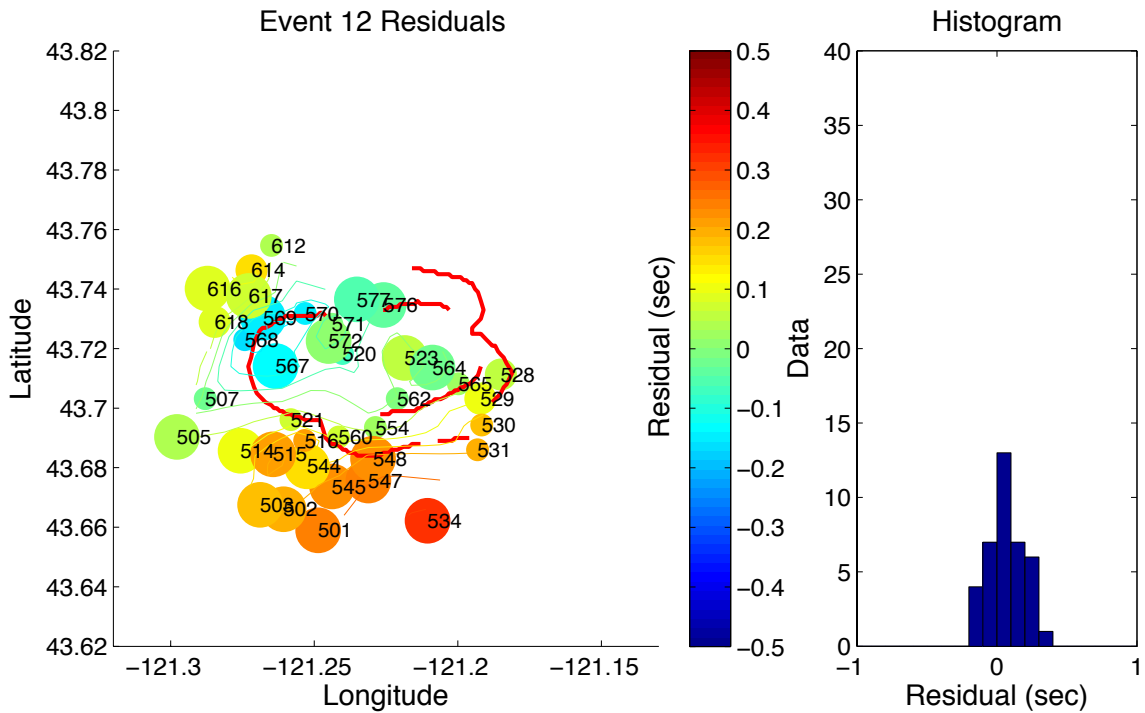
Event 7, 1983. Residuals are plotted by station range from the event. Error bars show 68% confidence intervals.



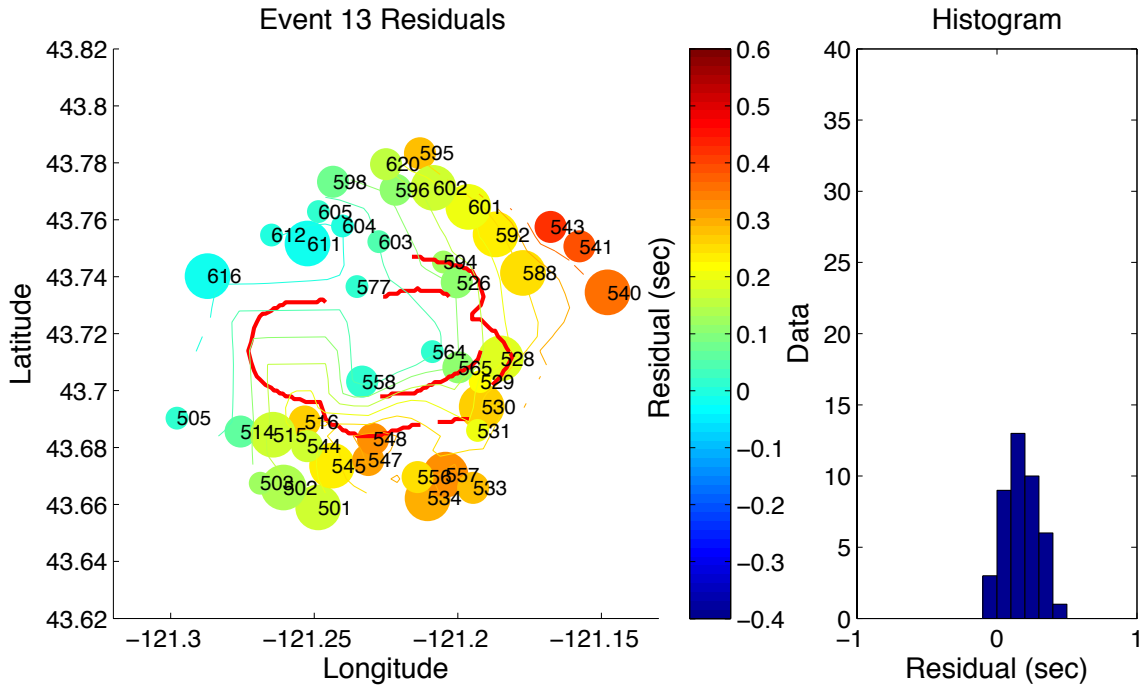
Event 8, 1983. Residuals are plotted by station range from the event. Error bars show 68% confidence intervals.



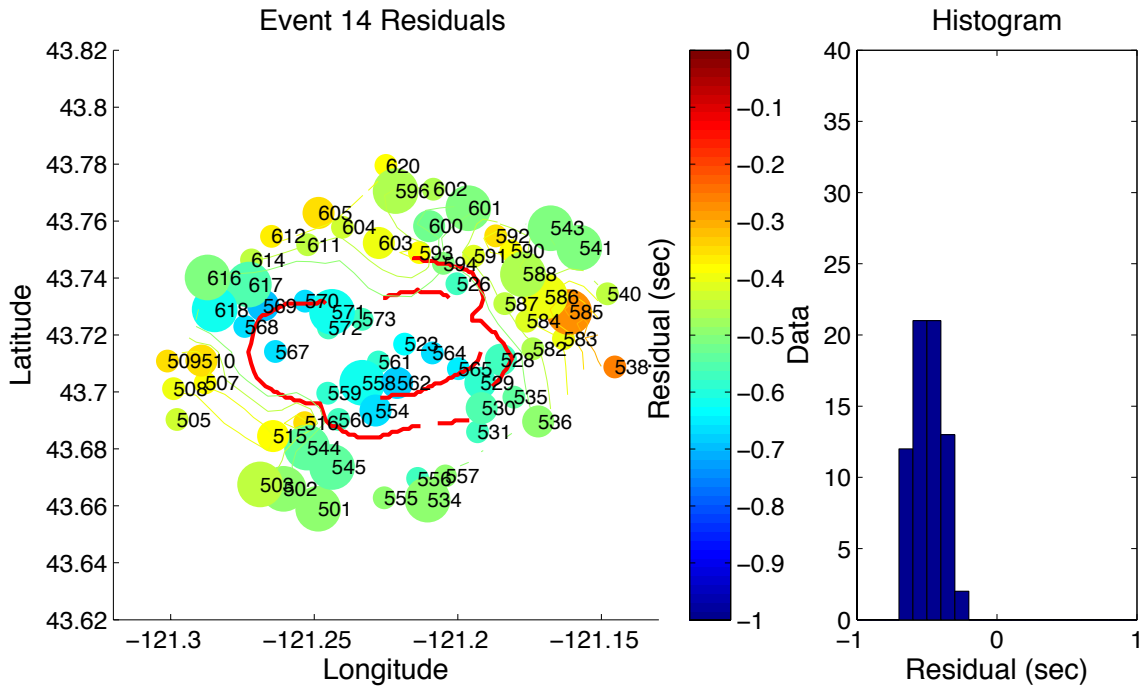
Event 10, 1983. Residuals are plotted by station range from the event. Error bars show 68% confidence intervals.



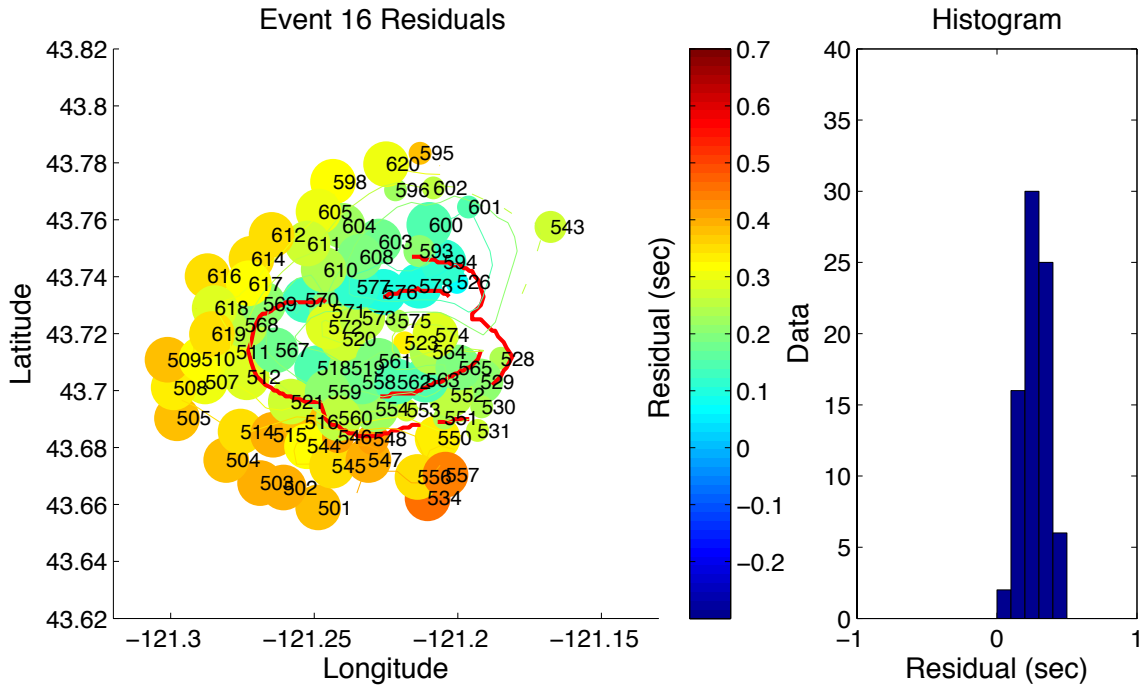
Event 12, 1984. Residuals are plotted in map view with color representing the magnitude of residual and size of circle inversely proportional to pick error. Red lines show caldera ring faults.



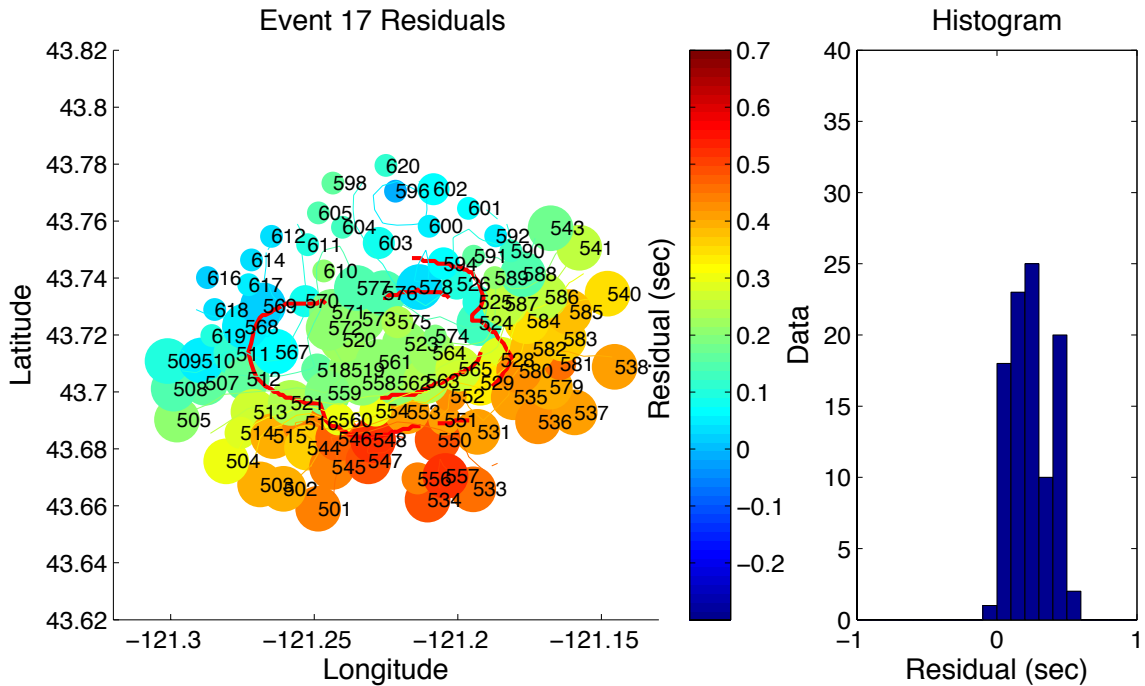
Event 13, 1984. Residuals are plotted in map view with color representing the magnitude of residual and size of circle inversely proportional to pick error. Red lines show caldera ring faults.



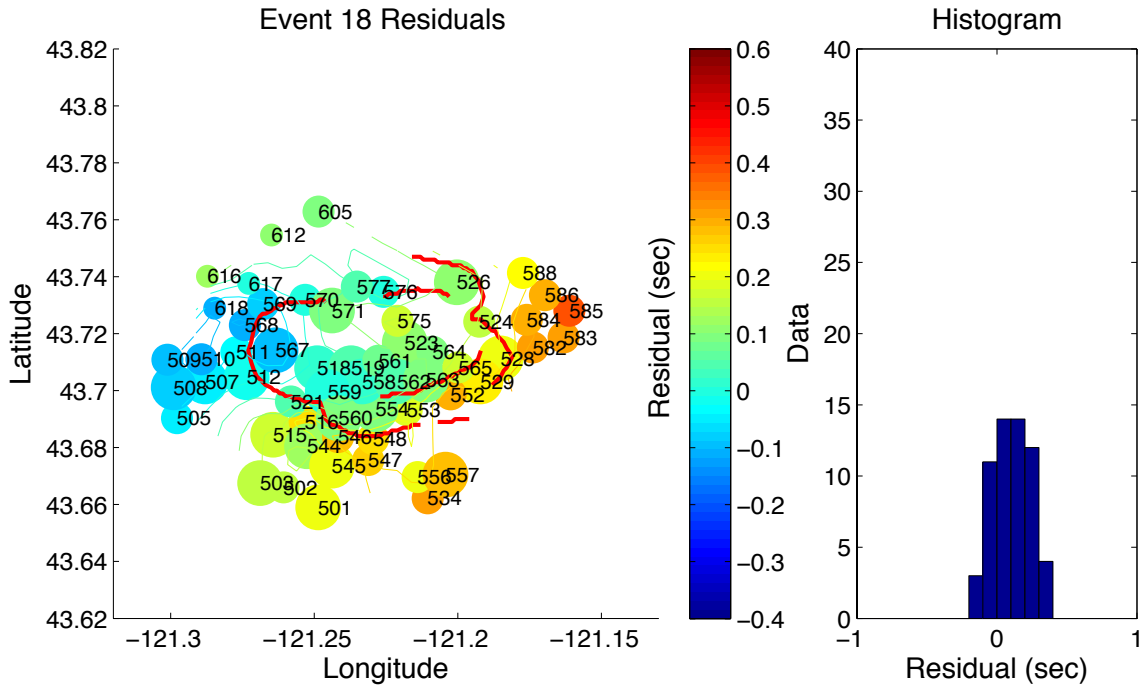
Event 14, 1984. Residuals are plotted in map view with color representing the magnitude of residual and size of circle inversely proportional to pick error. Red lines show caldera ring faults.



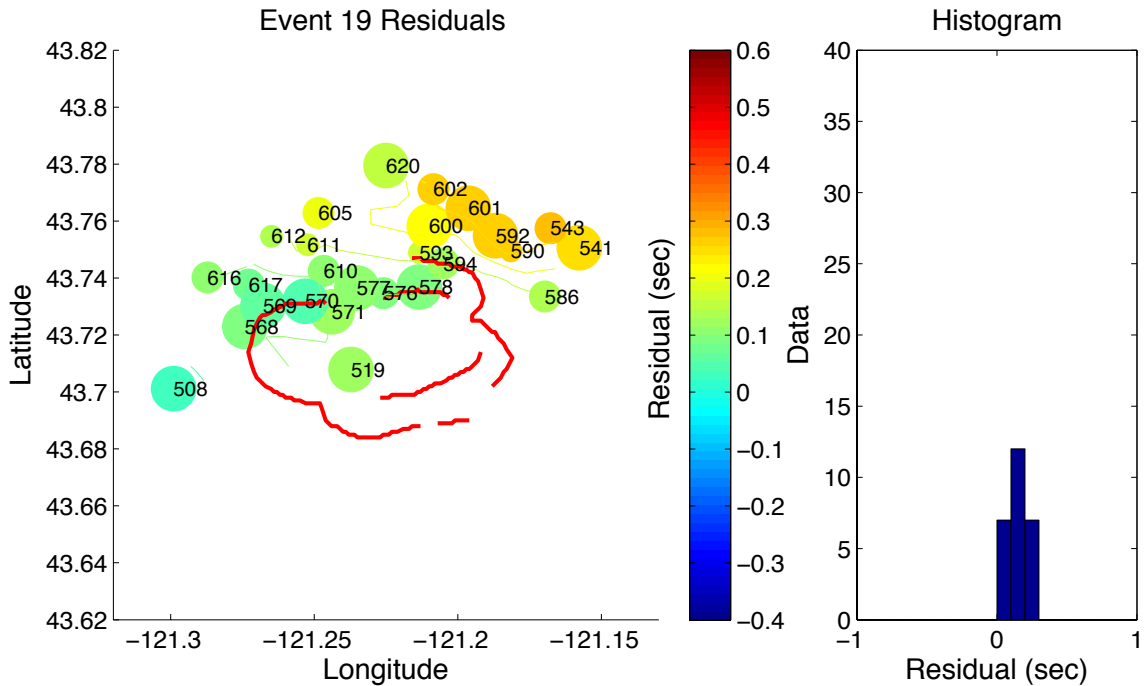
Event 16, 1984. Residuals are plotted in map view with color representing the magnitude of residual and size of circle inversely proportional to pick error. Red lines show caldera ring faults.



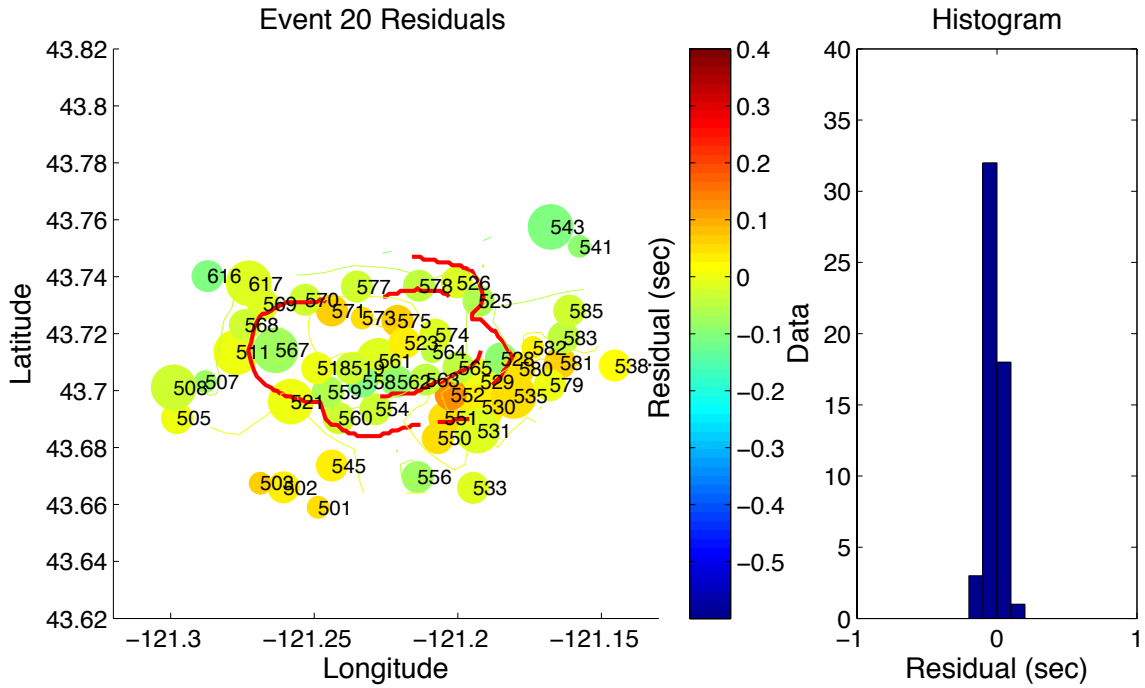
Event 17, 1984. Residuals are plotted in map view with color representing the magnitude of residual and size of circle inversely proportional to pick error. Red lines show caldera ring faults.



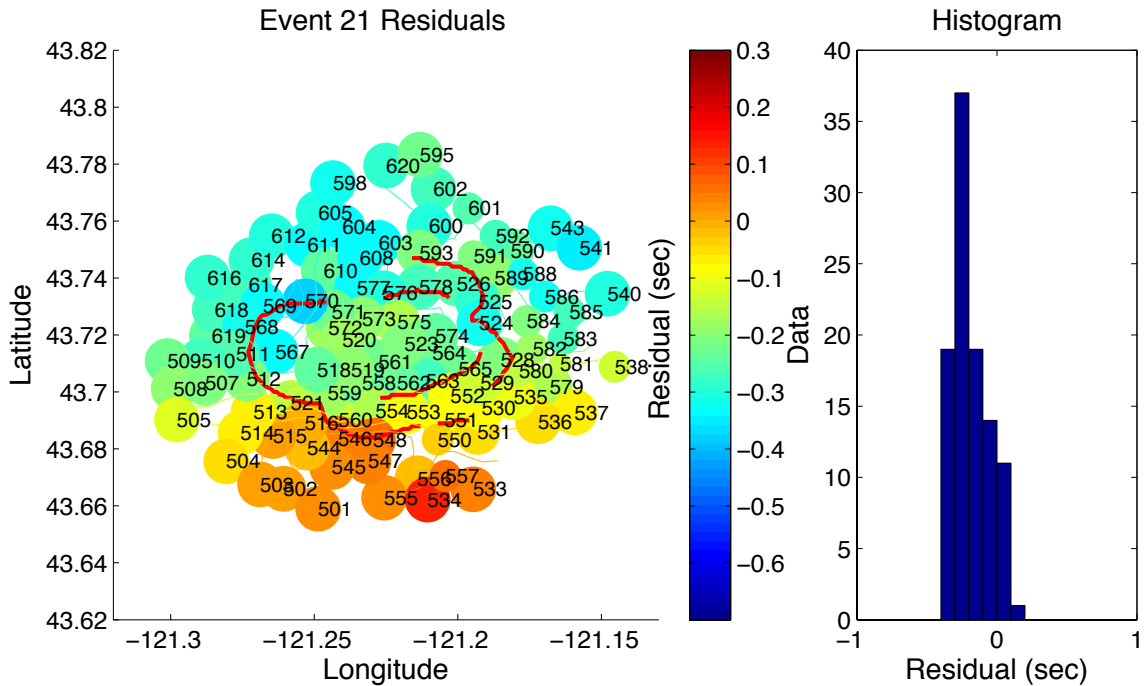
Event 18, 1984. Residuals are plotted in map view with color representing the magnitude of residual and size of circle inversely proportional to pick error. Red lines show caldera ring faults.



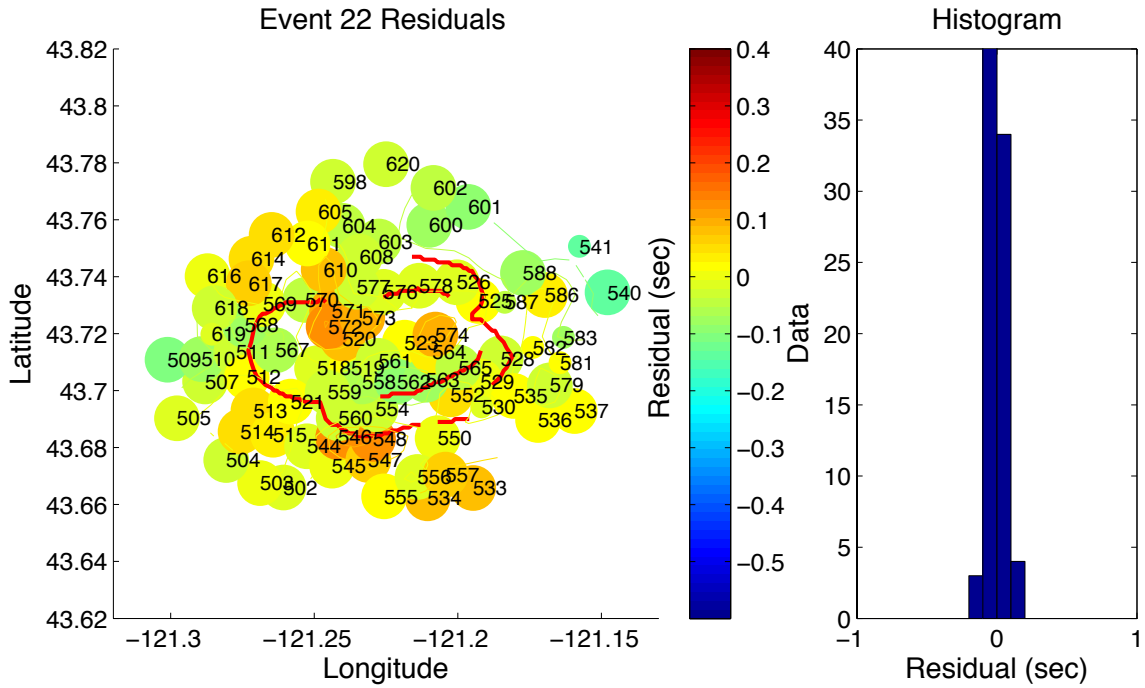
Event 19, 1984. Residuals are plotted in map view with color representing the magnitude of residual and size of circle inversely proportional to pick error. Red lines show caldera ring faults.



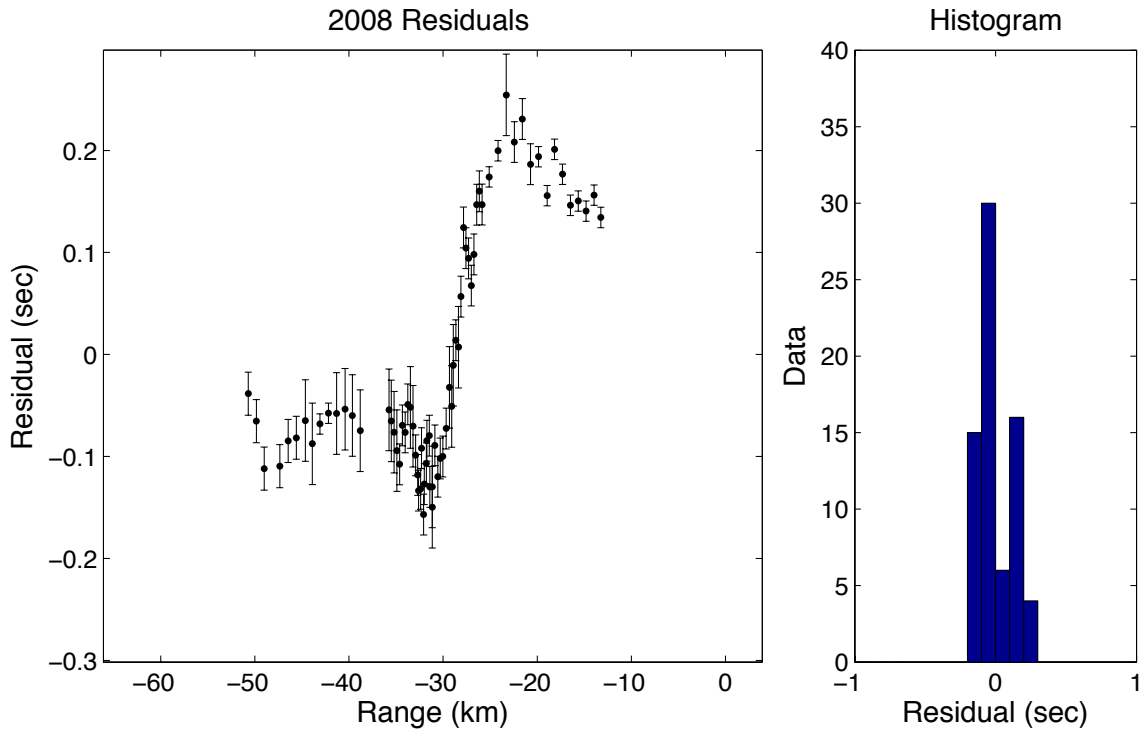
Event 20, 1984. Residuals are plotted in map view with color representing the magnitude of residual and size of circle inversely proportional to pick error. Red lines show caldera ring faults.



Event 21, 1984. Residuals are plotted in map view with color representing the magnitude of residual and size of circle inversely proportional to pick error. Red lines show caldera ring faults.



Event 22, 1984. Residuals are plotted in map view with color representing the magnitude of residual and size of circle inversely proportional to pick error. Red lines show caldera ring faults.



Event 9011, 2008. Residuals are plotted by station range from the event. Error bars show 68% confidence intervals.

REFERENCES CITED

- Achauer, U., Evans, J., & Stauber, D. (1988). High-resolution seismic tomography of compressional wave velocity structure at Newberry Volcano, Oregon Cascade Range. *Journal of Geophysical Research* , 93 (B9), 10,135-10,147.
- Acocella, V., Funicello, R., Marotta, E., & Orsi, G. (2004). The role of extensional structures on experimental calderas and resurgence. *Journal of Volcanology and Geothermal Research* , 129 (1-3), 199-217.
- Ancochea, E., Brändle, J., & Huertas, M. (2003). The felsic dikes of La Gomera (Canary Islands): identification of cone sheet and radial dike swarms. *Journal of Volcanology and Geothermal Research* , 120 (3-4), 197-206.
- Anderson, E. (1937). Cone-sheets and ring-dykes: the dynamical explanation. *Bulletin of Volcanology* , 1 (1), 35-40.
- Aster, R., & Meyer, R. (1989). Determination of shear- and compressional-wave velocity variations and hypocenter locations in a rapidly-inflating caldera: the Campi Flegrei, *Physics of the Earth and Planetary Interiors* , 55, 313-325.
- Auger, E., Gasparini, P., Virieux, J., & Zollo, A. (2001). Seismic evidence of an extended magmatic sill under Mt. Vesuvius. *Science* , 294, 1510-1512.
- Bauer, K., Trumbull, R., & Vietor, T. (2003). Geophysical images and a crustal model of intrusive structures beneath the Messum ring complex, Namibia. *Earth and Planetary Science Letters* , 216, 65-80.
- Ben-Zvi, T., Wilcock, W., Barclay, A., Zandomenighi, D., Ibáñez, J., & Almendros, J. (2009). The P-wave velocity structure of Deception Island, Antarctica, from two-dimensional seismic tomography. *Journal of Volcanology and Geothermal Research* , 180 (1), 67-80.
- Bons, P., & Dougherty-Page, J. (2001). Stepwise accumulation and ascent of magmas. *Journal of Metamorphic Geology* , 19, 627-633.
- Bosworth, W., Burke, K., & Strecker, M. (2000). Magma chamber elongation as an indicator of intraplate stress field orientation: 'borehole breakout mechanism' and examples from the Late Pleistocene to Recent Kenya Rift Valley. In: Jessel, M.W., Urai, J.L. (Eds.), *Stress, Strain and Structure, a Volume in Honour of W.D. Means. Journal of the Virtual Explorer* , 2.
- Brown, L., Chapin, C., Sanford, A., & Kaufman, S. (1980). Deep structure of the Rio Grande rift from seismic reflection profiling. *Journal of Geophysical Research* , 85 (B9), 4773-4800.

- Catchings, R., & Mooney, W. (1988). Crustal structure of east central Oregon: relation between Newberry Volcano and regional crustal structure. *Journal of Geophysical Research* , 93 (B9), 10,081-10,094.
- Christensen, N., & Mooney, W. (1995). Seismic velocity structure and composition of the continental crust: A global view. *Journal of Geophysical Research* , 100 (B7), 9761-9788.
- Chu, R., Helmberger, D., Sun, D., Jackson, J., & Zhu, L. (2010). Mushy magma beneath Yellowstone. *Geophysical Research Letters* , 37 (1), L01306.
- Cole, J., Nilner, D., & Spudis, K. (2005). Calderas and caldera structures; a review. *Earth Science Reviews* , 69, 1–26.
- Cotton, J., & Catchings, R. (1989). Eata report for the 1983 U.S. Geological Survey East-Central Oregon Seismic Refraction Experiment. *U.S. Geological Survey Open File Report* , 89-124.
- Dawson, P., & Stauber, D. (1986). Data report for a three-dimensional high-resolution P-velocity structural investigation of Newberry Volcano, Oregon, using seismic tomography. *U.S. Geological Survey Open File Report* , 86-352.
- Dunn, R., Toomey, D., & Solomon, S. (2000). Three-dimensional seismic structure and physical properties of the crust and shallow mantle beneath the East Pacific Rise at 9 30'N. *Journal of Geophysical Research* , 105 (B10), 23,537–23,555.
- Durant, D., & Toomey, D. (2009). Evidence and implications of crustal magmatism on the flanks of the East Pacific Rise. *Earth and Planetary Science Letters* , 287 (1-2), 130-136.
- Fitterman, D. (1988). Overview of the structure and geothermal potential of Newberry Volcano, Oregon. *Journal of Geophysical Research* , 93 (B9), 10,059-10,066.
- Fitterman, D., Stanley, W., & Bisdorf, R. (1988). Electrical structure of Newberry volcano, Oregon. *Journal of Geophysical Research* , 93 (B9), 10,119-10,134.
- Flecha, I., Martí, D., Carbonell, R., & Escuder-Viruete, J. (2004). Imaging low-velocity anomalies with the aid of seismic tomography. *Tectonophysics* , 388, 225–238.
- Gettings, M., & Griscom, A. (1988). Gravity model studies of Newberry Volcano, Oregon. *Journal of Geophysical Research* , 93 (B9), 10,109-10,118.
- Gudmundsson, M., & Högnadóttir, T. (2007). Volcanic systems and calderas in the Vatnajökull region, central Iceland: Constraints on crustal structure from gravity data. *Journal of Geodynamics* (43), 153–169.
- Holtz, F., Johannes, W., Tamic, N., & Behrens, H. (2001). Maximum and minimum water contents of granitic melts generated in the crust: a reevaluation and implications. *Lithos* , 56, 1-14.

- Hooft, E., & Detrick, R. (1993). The role of density in the accumulation of basaltic melts at mid-ocean ridges. *Geophysical Research Letters* , 20 (6), 423-426.
- Jensen, R., Donnelly-Nolan, J., & McKay, D. (2009). A field guide to Newberry Volcano, Oregon. *Volcanoes to Vineyards: Geologic Field Trips Through the Dynamic Landscape of the Pacific Northwest* , 53-79.
- Keith, T., & Bargar, K. (1988). Petrology and hydrothermal mineralogy of US Geological Survey Newberry 2 drill core from Newberry Caldera, Oregon. *Journal of Geophysical Research* , 93 (B9), 10,174–10,190.
- Klausen, M. (2004). Geometry and mode of emplacement of the Thverartindur cone sheet swarm, SE Iceland. *Journal of Volcanology and Geothermal Research* , 138, 185-204.
- Koenders, M., & Petford, N. (2003). Thermally induced primary fracture development in tabular granitic plutons: a preliminary analysis. *Geological Society London Special Publications* , 214 (1), 143-150.
- Lees, J., & Wu, H. (2000). Poisson's ratio and porosity at Coso geothermal area, California. *Journal of Volcanology and Geothermal Research* , 95, 157-173.
- Legros, F., Kelfoun, K., & Marti, J. (2000). The influence of conduit geometry on the dynamics of caldera-forming eruptions. *Earth and Planetary Science Letters* , 179 (1), 53-61.
- Linneman, S., & Myers, J. (1990). Magmatic inclusions in the Holocene rhyolites of Newberry volcano, central Oregon. *Journal of Geophysical Research* , 95 (B11), 17,677-17,691.
- Lipman, P. (1997). Subsidence of ash-flow calderas: relation to caldera size and magma-chamber geometry. *Bulletin of Volcanology* , 59, 198-218.
- MacLeod, N., & Sherrod, D. (1988). Geologic evidence for a magma chamber beneath Newberry Volcano, Oregon. *Journal of Geophysical Research* , 93 (B9), 10,067-10,079.
- MacLeod, N., Sherrod, D., Chitwood, L., & Jensen, R. (1995). Geologic map of Newberry volcano, Deschutes, Klamath, and Lake Counties, Oregon. *U.S. Geological Survey Miscellaneous Investigations* , Map I-2455, scales 1:62,500 and 1:24,000.
- Marsh, B. (1989). Magma chambers. *Annual Review of Earth and Planetary Sciences* , 17 (1), 439-472.
- Marti, J., Ablay, G., & Redshaw, L. (1994). Experimental studies of collapse calderas. *Journal of the Geological Society* , 151, 919-929.

- Mckay, D., Donnelly-Nolan, J., Jensen, R., & Champion, D. (2009). The post-Mazama northwest rift zone eruption at Newberry Volcano, Oregon. *Volcanoes to Vineyards: Geologic Field Trips Through the Dynamic Landscape of the Pacific Northwest* , 1-20.
- Morgan, J., & Chen, Y. (1993). The genesis of oceanic crust: Magma injection, hydrothermal circulation, and crustal flow. *Journal of Geophysical Research* , 98 (B4), 6283-6297.
- Nercessian, A., Hirn, A., & Tarantola, A. (1984). Three-dimensional seismic transmission prospecting of the Mont Dore volcano, France. *Geophysical Journal of the Royal Astronomical Society* , 76, 307-315.
- Petford, N. (2003). Rheology of granitic magmas during ascent and emplacement. *Annual Review of Earth and Planetary Sciences* , 31, 399–427.
- Ryan, M. (1988). The mechanics and three-dimensional internal structure of active magmatic systems: Kilauea volcano, Hawaii. *Journal of Geophysical Research* , 93, 4213-4248.
- Sammel, E., Ingebritsen, S., & Mariner, R. (1988). The hydrothermal system at Newberry Volcano, Oregon. *Journal of Geophysical Research* , 93 (B9), 10,149-10,162.
- Sanford, A., Alptekin, O., & Topozada, T. (1973). Use of reflection phases on microearthquake seismograms to map an unusual discontinuity beneath the Rio Grande rift. *Bulletin of the Seismological Society of America* , 63 (6), 2021-2034.
- Saunders, S. (2004). The possible contribution of circumferential fault intrusion to caldera resurgence. *Bulletin of Volcanology* , 67, 57-71.
- Schirnack, C., Van Den Bogaard, P., & Schmincke, H. (1999). Cone sheet formation and intrusive growth of an oceanic island—The Miocene Tejada complex on Gran Canaria (Canary Islands). *Geology* , 27, 207-210.
- Sheetz, K., & Schlue, J. (1992). Inferences for the Socorro magma body from teleseismic receiver functions. *Geophysical Research Letters* , 19 (18), 1867-1870.
- Shuey, R. (1985). A simplification of the Zoeppritz equations. *Geophysics* , 50 (4), 609-614.
- Stauber, D., Green, S., & Iyer, H. (1988). Three-dimensional P velocity structure of the crust below Newberry Volcano, Oregon. *Journal of Geophysical Research* , 93 (B9), 10,095-10,107.
- Steck, L., Thurber, C., Fehler, M., Lutter, W., Roberts, P., Baldrige, W., et al. (1998). Crust and upper mantle P wave velocity structure beneath Valles caldera, New Mexico: Results from the Jemez teleseismic tomography experiment. *Journal of Geophysical Research* , 103 (B10), 24,301-24,320.

- Toomey, D., Solomon, S., & Purdy, G. (1994). Tomographic imaging of the shallow crustal structure of the East Pacific Rise at 9 deg 30 min N. *Journal of Geophysical Research* , 99 (B12), 24,135-24,157.
- Vera, E., Mutter, J., Buhl, P., Orcutt, J., Harding, A., Kappus, M., Detrick, R., Brocher, T. (1990). The structure of 0-to 0.2-my-old oceanic crust at 9 N on the East Pacific Rise from expanded spread profiles. *Journal of Geophysical Research* , 95 (B10), 15,529-15,556.
- Vigneresse, J., Barbey, P., & Cuney, M. (1996). Rheological transitions during partial melting and crystallization with application to felsic magma segregation and transfer. *Journal of Petrology* , 57 (6), 1579-1600.
- West, M., Menke, W., Tolstoy, M., Webb, S., & Sohn, R. (2001). Magma storage beneath Axial volcano on the Juan de Fuca mid-ocean ridge. *Nature* , 413 (6858), 833-836.
- Wilcock, W., Dougherty, M., Solomon, S., Purdy, G., & Toomey, D. (1993). Seismic propagation across the East Pacific Rise: finite difference experiments and implications for seismic tomography. *Journal of Geophysical Research* , 98 (19), 19,913-19,932.
- Zollo, A., Maercklin, N., Vassallo, M., & Iacono, D. (2008). Seismic reflections reveal a massive melt layer feeding Campi Flegrei caldera. *Geophysical Research Letters* , 35, L12306.
- Zucca, J., & Evans, J. (1992). Active high-resolution compressional wave attenuation tomography at Newberry Volcano, Central Cascade Range. *Journal of Geophysical Research* , 97 (B7), 11,047-11,055.